Modeling Neural Activity in the Cardiovascular Control System: The Effects of Neural Circuit Structure and Intrinsic Cellular Properties

By

ADAM ROSE
DISSERTATION

Submitted in partial satisfaction of the requirements for the degree of

DOCTOR OF PHILOSOPHY

in

APPLIED MATHEMATICS

in the

OFFICE OF GRADUATE STUDIES

of the

UNIVERSITY OF CALIFORNIA

DAVIS

Approved:

———————————————
Timothy Lewis, Chair

———————————————
Colleen Clancy

———————————————
Rishidev Chaudhuri

Committee in Charge

2024

i

To Mom, Dad, and Ana.
I would not have completed this dissertation without your support and love.

Contents

Abstract

The autonomic nervous system (ANS) plays a critical role in neurocardiovascular control. The structure of the neural circuitry and intrinsic properties of autonomic neurons are likely to play important roles in shaping the ANS control response to changes in blood demand. In this dissertation, we explore how the M-current, cardiac feedback, and recurrent neural connections shape the firing dynamics of autonomic cardiac ganglia. In chapter 2, a data-informed, idealized cell-based mathematical model of the neural circuitry in the intrinsic cardiac nervous system (ICNS) is developed that captures the firing properties of ICNS neurons. The model indicates that the M-current and cardiac-cycle dependent feedback shape the firing dynamics of ICNS neurons. In chapter 3, we explain how the M-current bestows ICNS neurons with band-pass filter and resonance properties. In chapter 4, we reduce the cell-based ICNS network model to a firing rate model, which enables extensive mathematical analysis. Analysis of the firing rate model is used to gain insight into how bistability can arise in the cell-based ICNS network model through M-current dynamics and recurrent excitation in the network. Predictions from the firing rate model are confirmed in the cell-based model. Finally, in chapter 5, we extend our ICNS network models to include the neural circuity of the sympathetic and parasympathetic autonomic tracts, the sino-atrial node, the cardiovascular system, and the baroreflex to describe the full autonomic neurocardiovascular control system. Our preliminary results suggest that the detailed structure of the autonomic neural circuitry (beyond just the baroreflex) could upregulate the magnitude and speed of the hearts response to a sudden increase in blood demand.

Acknowledgments

To my advisor Timothy Lewis: I can not emphasize enough how important your support was throughout this experience. I may not have been the easiest student to work with, but I am forever grateful that you were there to lend me your guidance and help me grow as a mathematician, and as a person. Thank you, Tim.

To my Qualifying Exam and Dissertation committee members at UC Davis, Colleen Clancy, Bob Guy, Becca Thomases, Rishi Chaudhuri, and Sam Walcott: Thank you for challenging me and reminding me that I need to think about my work in a clear manner and be concise and informative in my communication. Your feedback provided me with insight that made this dissertation possible.

To the staff of Math Department (past and present) including Sarah Driver and Tina Denena: Your kindness and compassion in dealing with the struggles of graduate students is unmatched. I will forever appreciate your support, and know that this department runs because of you.

To all of my past instructors from UC Davis and UC Santa Barbara, including Thomas Sideris and Lee Kennard: Thank you for providing me with the tools I needed to grow my mathematical abilities and the considerable amount of energy you expended advising me about my future in graduate school.

To my friends in Davis and Los Angeles: Thank you for the never-ending love and support. I would have been bored out of my mind without the numerous trivia nights, brewery tours, game nights and cooking adventures we had.

Finally, to Mom, Dad, Ana, and our dog Tonttu: You supported me through the times when I struggled to believe in myself. You provided love, compassion, and perspective that was (sometimes) completely foreign to me. I love you.

CHAPTER 1

Introduction

On a daily basis, the human body encounters a myriad of situations that require adaptation. For example, during exercise, there is increased oxygen demand by muscle tissue, and therefore heart rate and myocardial contractility are increased, blood flow is redistributed to the muscles and away from visceral organs, and resistance of the peripheral vasculature is increased [**36**, **64**]. All of these adaptations must be highly coordinated. These complex cardiovascular phenomena necessitate a control system that can adapt to the changes in conditions or demand. The Autonomic Nervous System (ANS) provides the infrastructure for the necessary adaptations in the form of neurocardiovascular control.

1.1. Structure of Autonomic Neural Control of Cardiovascular System

The ANS, also known as the involuntary nervous system, is a portion of the nervous system that acts as a control system for the human internal environment. There are two branches within the ANS: the sympathetic and the parasympathetic nervous systems. Activity in the sympathetic branch typically increases during times of stress, anxiety, and physical activity, and said to be linked to fight-or-flight behavior. The parasympathetic branch typically has increased activity during sedentary activities, which are often referred to as rest-and-digest behaviors [**10**]. The neural outputs of the sympathetic and parasympathetic nervous systems target the visceral organs and regulate function. One subsystem of the ANS is the neurocardiovascular control system [**10**, **79**]. The sympathetic and parasympathetic nervous systems work in coordination with each other, both exerting influence on the cardiovascular system in a manner that keeps the body in homeostasis.

Figure 1.1 shows the structure of the Autonomic Neurocardiovascular Control System. The sympathetic tract of the cardiovascular ANS (shown as blue in figure 1.1) originates in the brainstem, with neuronal axons projecting from the medulla and synapsing onto neurons in spinal cord [10, 79]. These neurons located in the spinal cord then project into the intrathoracic cavity and synapse onto intrathoracic extra-cardiac ganglia, i.e., the Intrathoracic Nervous System (ITNS). The ITNS contains the somata of efferent sympathetic neurons, afferent feedback axons, local circuit neurons, and interneurons, forming an interconnected neural network [4, 6, 10]. Efferent neurons in the ITNS innervate neurons in ganglia located on the surface of the heart, as well as blood vessels [4, 6, 10]. The collection of cardiac ganglia on the heart are referred to as the Intrinsic Cardiac Nervous System (ICNS). The ICNS contains afferent feedback neurons, efferent neurons, local circuit neurons, and interneurons similar to the ITNS, and form a complex neural circuit [4, 6, 9, 24].

The parasympathetic tract of the cardiovascular ANS (shown as green in figure 1.1) originates from the brainstem. The pre-ganglionic CNS neurons project to and synapse onto neurons in ICNS ganglia [10]. Note that the ICNS contains both symapthetic and parasympathetic gangia, with afferent sympathetic axons innervating ITNS neurons [4, 6, 9, 24]. The sympathetic and parasympathetic ICNS innervate the heart and exert influence over cardiac activity [4, 6].

Multiple sources of neural feedback to the ANS provide information about the states of the heart and vasculature. Baro- and chemo-receptors transduce arterial blood pressure and partial pressures of oxygen and carbon dioxide into neural signals that are sent through afferent neural pathways to the brainstem via nodose and dorsal root ganglia. These neural signals are processed in the brainstem, and a control signal is communicated via the efferent neural circuitry of the ANS to the heart and vasculature. Also, cardiac sensory neurites located in the in the heart transduce mechanical and chemical inputs from the heart (e.g., ventricular deformation) and send this information to the ICNS, ITNS, and CNS [4, 6, 9, 10, 69, 79]. Thus, the combined structure of the descending sympathetic and parasympathetic

pathways and the multiple feedback loops results in a set of nested feedback loops in the neurocardiovascular control system (shown in figure 1.1) that modulate blood pressure, heart rate, and heart contractility [3, 10, 41].
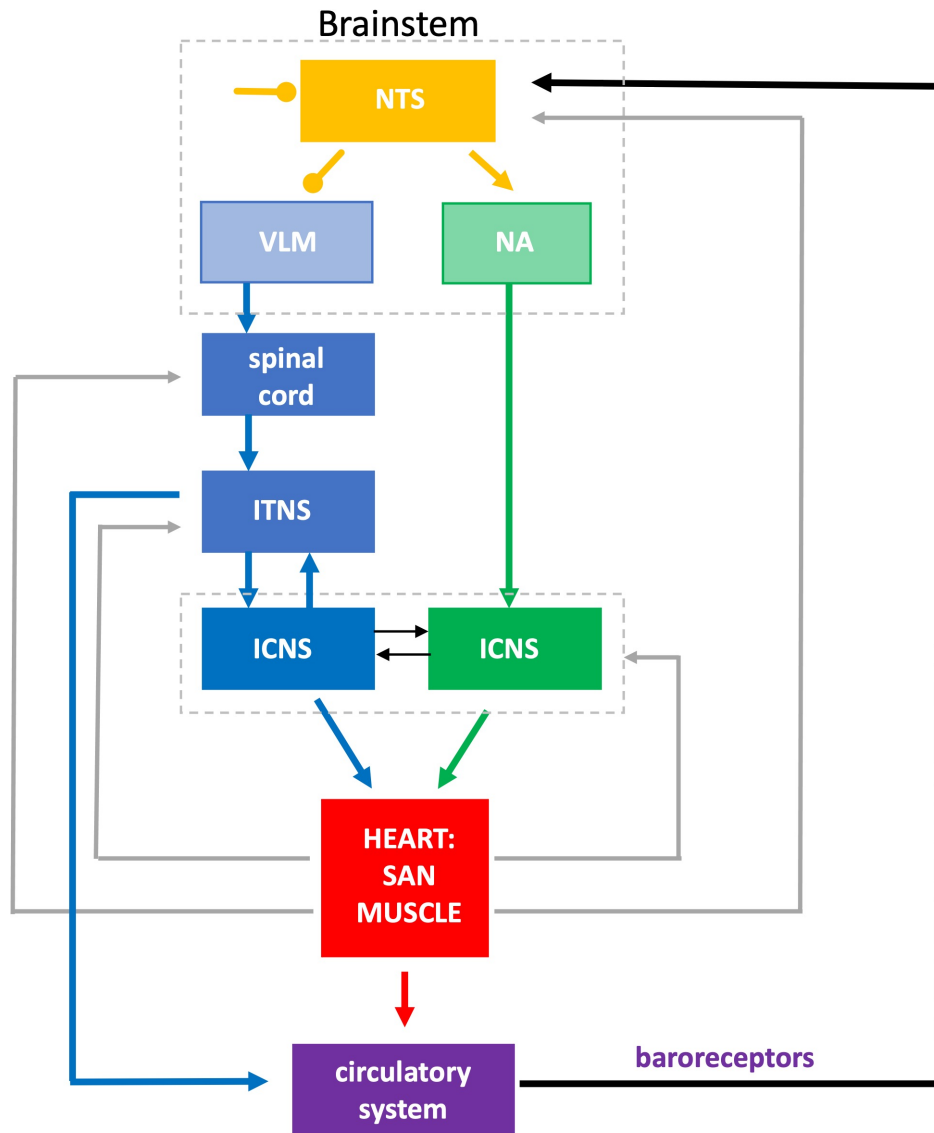
FIGURE 1.1. Structure of Autonomic Control of the Cardiovascular system. Symapthetic nervous system in blue, Parasympathetic nervous system in green, local feedback from sensory neurites in gray. The Nucleus Tractus Solitarius (NTS) receives central drive information and afferent inputs from baro-/chemo-receptors and cardiac sensory neurons, and relays commands for sympathetic and parasympathetic activation to the ventrolateral medulla (VLM) and the nucleus ambiguus (NA), respectively [10, 27].

1.2. Classical versus Hierarchical View of Neural Control of Cardiovasculature

Classically, the neural circuitry of the ITNS and ICNS between the heart and the brainstem was considered to simply relay the central control signal from the brainstem to reach the target organs and vasculature with the only feedback coming from arterial baro- and chemoreceptors. This ignored the information processing of the signal along the efferent fibers, and the feedback from the heart directly to the ICNS and ITNS [4, 6, 9, 24, 37, 63, 69, 79]. In fact, to my knowledge, the ICNS is typically not mentioned by name in textbooks on medical physiology (e.g., [10, 18, 27]). These complex peripheral subsystems (i.e., ITNS & ICNS) process information and therefore must provide additional qualities to the neurocardiovascular control system. However, the details of what these neural processing centers are contributing to the model of neural control are unclear. This dissertation employs an exploratory modeling approach to begin to address potential contributions that the hierarchical structure of the ANS has on the autonomic control of the cardiovascular system.

1.3. Exploring Roles of Afferent Cardiac Feedback Coupled with Intrinsic Properties of ANS Neurons

Recently, it has been suggested that the local circuitry and cardiovascular feedback pathways in the ICNS and ITNS play an important role in autonomic neurocardiovascular control [5, 6, 9, 63, 69, 79]. Local circuit neurons project axons between ICNS ganglia, interneurons synapse onto post-synaptic neurons in the same ganglia, efferent somata project to neurons in the ITNS, and afferent cell bodies synapse onto the heart [4, 9, 24, 63, 69, 79]. Post-synaptic ICNS neurons receive beat-to-beat information from pre-synaptic atrial pressure receptors [4, 69, 78]. The transduced pressure indices are integrated with, and modulate, the efferent central command signal, and they also allow the ICNS to function independently of central command [5, 6, 7, 69, 78, 79]. Becuase cardiac feedback though the local circuit is prevalent in ICNS neurons, we seek to understand how the afferent local cardiac feedback

can lead to specific information processing in the network (e.g., how does cardiac feedback regulate the firing behavior of the ICNS network?)

The M-current is a non-inactivating voltage-gated K^+ current that is prevalent in autonomic cardiac ganglia, including the lumbar and superior cervical ganglia, the stellate ganglia, and the ICNS. [14, 17, 21, 22, 51]. It is slow activating (∼100-200 msec) and it activates below the threshold for firing an action potential [14, 17]. Thus the M-current is thought to control the excitability of the neurons [14, 17, 22, 30, 45, 54, 84]. Specifically, the M-current can increase the rheobase, i.e., the minimum stimulus required to reach action potential threshold [22] and endow with spike frequency adaptation (i.e., as the cell fires repeatedly, the M-current builds up and begins to inhibit the cell's firing). Intrinsic properties of neurons can determine the behavior of the ICNS network. Because the M-current is prevalent in ANS cardiac neurons and is known to have powerful impact on the firing of neurons, we focus on this particular intrinsic property of ICNS neurons and seek to understand how the slow activation (i.e., adaptation) leads to specific information processing properties of the network.

The research that I present in this dissertation uses mathematical models and analysis to explore the dynamics of the ICNS neural network and to gain insight into possible roles of the ICNS. The initial focus is on the ICNS, and then the model will be incorporated into a hierarchical model of the ANS. Specifically, I utilize high dimensional cell-based and low-dimensional firing rate models and focus on key components such as network connectivity, afferent cardiovascular feedback, and intrinsic properties of individual neurons, especially the role of the M-current.

1.4. Chapter Summaries

In Chapter 2, I develop a mathematical model of the ICNS with afferent cardiac feedback. Note, however, that the structure of the model can be applied to the ITNS. The model consists of a network of generalized integrate-and-fire (GIF) model neurons with multiple intrinsic ionic conductances, and excitatory & inhibitory synaptic inputs due to central

drive, local pressure feedback, and intra-network connections. This extends previous modeling approaches that employed intra-network connections, central drive, and cardiovascular feedback but did not include conductance based neuron and synapses. I show that the neuronal network model suggests mechanisms that endow model neurons with firing statistics observed in ICNS neurons experimentally [9], and theorize that the M-current and leakage current counteract the slowly varying afferent cardiac feedback but allowing the neuron to respond primarily to faster input frequencies.

In Chapter 3, I focus on the subthreshold behavior of GIF model neurons taken from the cell-based network model of the ICNS to assess how the M-current endows the GIF neuron with the ability to filter out low-frequency variations in input. First, I show that incorporation of the M-current changes the GIF model behavior from that of a low-pass filter to that of a band-pass filter. I show that this band-pass filter and the resulting resonance frequency depend on the strength of the M-current in the model. Next, I show that the band-pass filter behavior and resonance frequencies depend on the subthreshold activation of the steady-state activation curve of the M-current and conclude that the subthresold activation of the M-current is responsible for the ability of the M-current to endow the model neuron to act like a band-pass filter with a resonant frequency.

In Chapter 4, I use dimensionality reduction techniques to reduce the system of $7N$ equations (where the network contains N neurons) of the cell-based network model of the ICNS to a 2-dimensional firing rate model. This reduction provides two main advantages - a drastic reduction in the time to simulate solutions of the model and allows for analytical tools such as phase-plane analysis to provide insight into the behavior of the model. I show through parameter exploration that the firing rate model indicates the M-current promotes bistability in the cell-based network model. Next, I build a bistable cell-based network model using the insights from the parameter exploration of the firing rate model and show that changing the model of the M-current can eliminate the bistability. I conclude that the M-current promotes bistability in the cell-based ICNS network model.

In Chapter 5, I develop two models of the autonomic neurocardiovascular control system. I implement a hierarchical model of the ANS with multiple nested feedback loops, a phase-model of the sinoatrial node, a mechanical cardiovascular model [**60**, **77**], and a model of the afferent dynamics of the baroreflex [**49**]. The hierarchical ANS model was implemented in two different ways: each subnetwork composed of the cell-based network model developed in Chapter 2, and each subnetwork composed of the firing rate model developed in Chapter 4. Next I showed that the ITNS and ICNS contribute to an increased (rate and magnitude of) response in heart rate due to blood loss.

CHAPTER 2

M-Current and Magnitude of Cardiovascular Feedback Regulate Neuronal Firing Behavior in the Intrinsic Cardiac Nervous System

The Intrinsic Cardiac Nervous System (ICNS) is an interconnected set of neuronal ganglia located on the surface of the heart. The network of nerve clusters receives efferent central command signals, afferent local feedback from the heart, and contain local circuit neurons & inter-neurons that are purported to process and propogate information throughout the ICNS. [**6**, **7**, **9**, **69**]. To gain insight into the role of the ICNS in the context of neural control of the cardiovascular system, we develop an idealized mathematical model that is based on several key biophysical details of the ICNS. The firing properties of ICNS neurons observed experimentally [**9**, **63**] arise naturally from this model, and thus imply possible mechanisms for the firing behavior.

In Beaumont et al 2013 [**9**], the firing times of ICNS neurons located in the right atrial ganglionated plexus of anaesthetized canines were recorded concurrently with the left ventricular pressure (LVP) over one minute time intervals. The neuronal spike times for each neuron were sorted into 10 bins based on the phase of the LVP at the time of the spike. These bins were used to create probability mass functions (firing histograms) that indicate the probability of a neuron firing an action potential at a particular phase of the cardiac cycle. Figure 2.1 shows histograms for 49 ICNS neurons (reproduced from [**9**]).
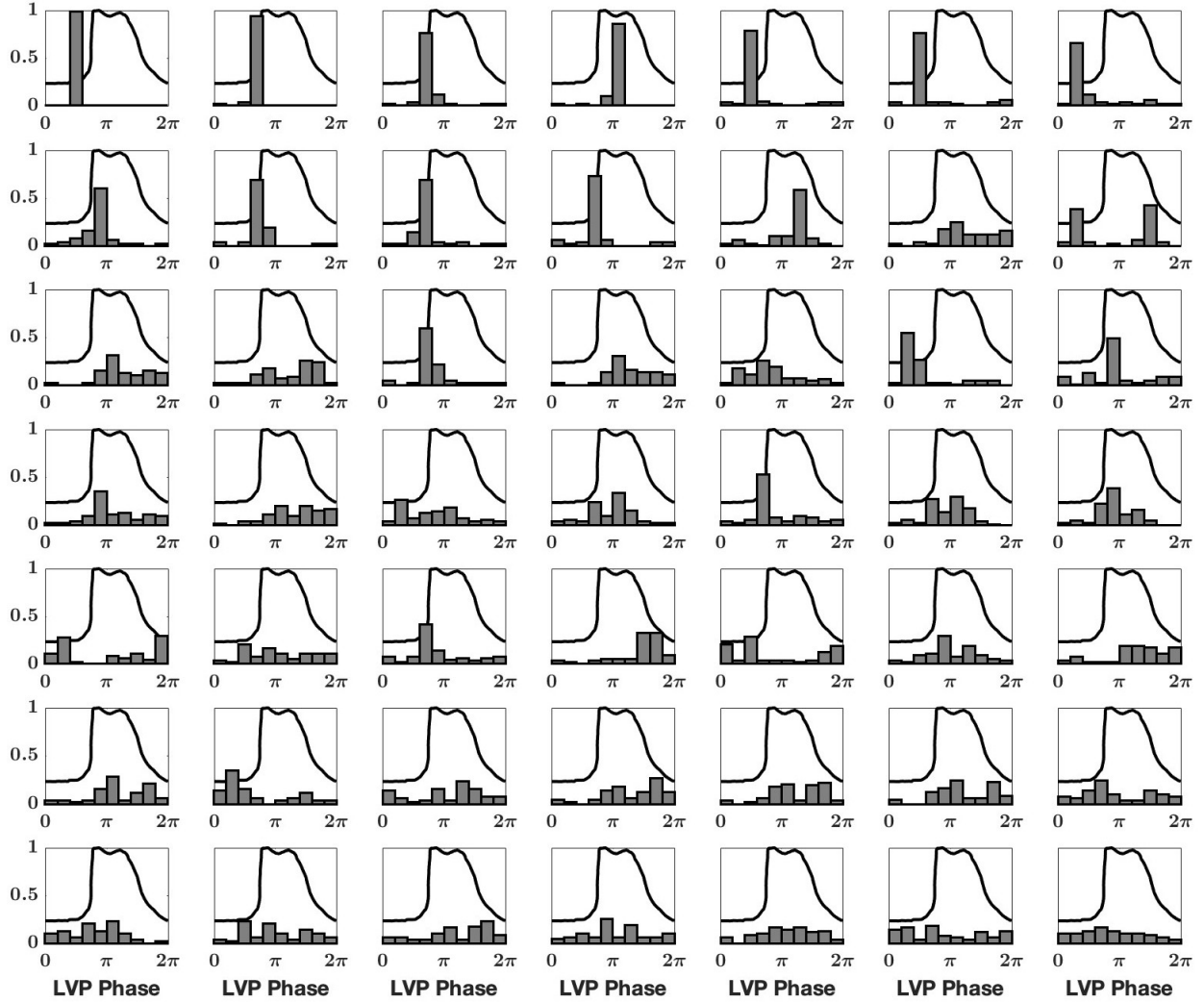
FIGURE 2.1. (A) Neuronal firing histograms with mean left ventricular pressure profile reproduced from Beaumont et al. 2013 [9]. Neurons fired at least 10 spikes per minute over 10 minutes of recording.

It was reported that 88% of ICNS neurons displayed firing with activity clustered around specific phases of cardiac cycle, i.e., LVP [9]. Many of the neurons that fired preferentially during certain phases of the cardiac cycle can be grouped into two distinct types of neuronal firing, which we will refer to as follower and phasic firing. Firing patterns that are not clustered around any specific phase of the cardiac cycle will be referred to as tonic firing. A canonical example of each of these three firing types is shown in figure 2.2. Follower neurons (figure 2.2, left) tend to fire more during systole (i.e. elevated LVP). Phasic neurons

9

fire predominantly during a specific phase of the cardiac cycle (e.g., during isovolumetric contraction, as shown in the middle histogram in figure 2.2). Tonic neurons (figure 2.2, right) fire at times that seem to have no correlation with the cardiac phase.
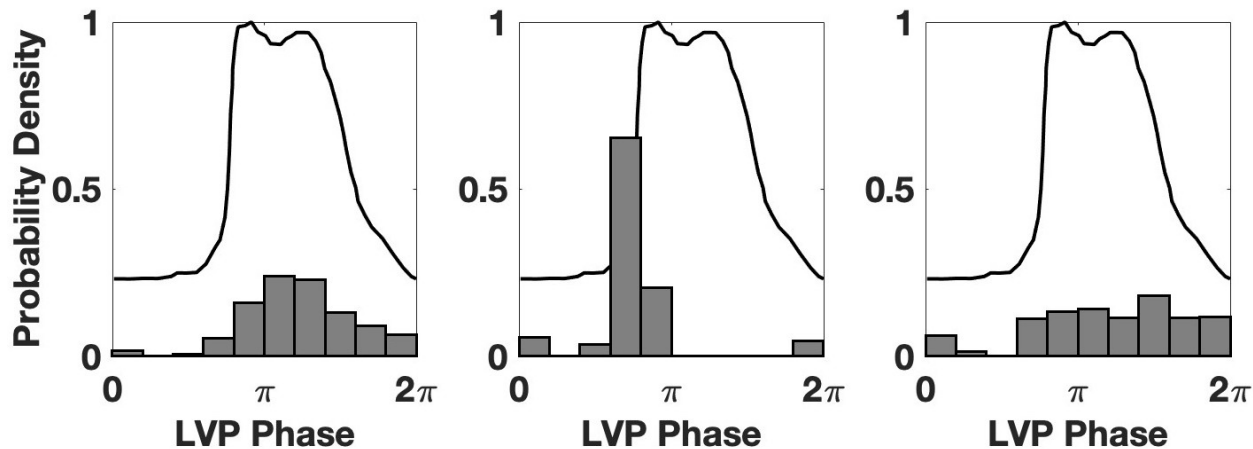
FIGURE 2.2. Three examples of the probability density of 3 example neuronal firing times as a function of the phase of the average left ventricular pressure. From left to right: follower, phasic, and tonic firing. Data reproduced from Beaumont et al. 2013 [9], figure 4.

While figure 2.2 shows the three canonical firing types, note that there are many neurons from figure 2.1 whose firing histograms do not fit cleanly into any of the three definitions. Figure 2.3 plots examples of firing histograms from [9] that do not fit the profile of any one of the three canonical firing types, but these three examples all share some aspects with at least one canonical firing type. The first neuron fires in a biphasic pattern, one peak of activity in diastole and the other in systole, rather than a singular phasic peak. The second neuron appears to share the traits of a tonic neuron and a phasic neuron, firing relatively throughout the cardiac cycle but also firing more often near peak systole. The third neuron appears to be a follower but it fires during diastole rather than systole. Indeed, clustering analysis shows that the ICNS neurons display a continuum of firing types rather than neurons fitting in distinct canonical firing types. (Appendix 2.5.2).
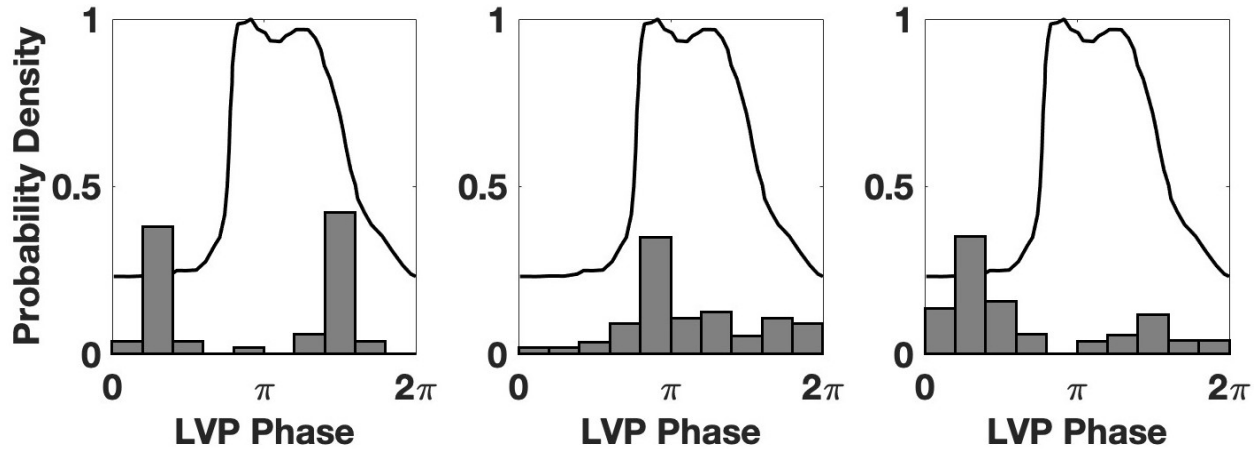
FIGURE 2.3. Firing histograms reproduced from Beaumont et al. 2013. which do not fit clearly into the definition of follower, phasic, or tonic firing. These neurons are inbetween the canonical firing types, sharing traits with multiple types at once.

It is not immediately clear what mechanisms are shaping the firing dynamics of the ICNS neurons, whether they behave like the canonical types or between. In this chapter, an idealized mathematical model of the ICNS neuronal network is developed as an exploratory tool to gain insight into the mechanisms underlying the canonical firing types of the ICNS neurons, and also the firing behaviors of the neurons that do not fit cleanly into the canonical types. (Note that while the idealized model is referred to as the ICNS network model, it can also be used to model ITNS activity.) I describe how the M-current, neural circuitry, and afferent cardiovascular feedback can induce the canonical firing types, and show that these mechanisms can indeed elicit the canonical firing types in single-cell models. I then present evidence of the mechanisms at work in the full ICNS network model. The combination of these mechanisms is also shown to elicit the firing behaviors that do not fit cleanly into a canonical firing type. I also observe that the M-current and the leakage current play a role in counteracting the slow (~ 1 Hz) afferent cardiovascular feedback (on average), while allowing higher frequency input to drive spikes.

2.1. Model Description

2.1.1. ICNS Neuronal Dynamics. The ICNS network model contain 100 model neurons. Individual neurons in the ICNS are described by a single-compartment conductance-based generalized integrate-and-fire (GIF) model [35]. The subthreshold dynamics of the neurons include a leakage current, a delayed-rectifier potassium current [79], an M-current [45], an intra-network synaptic current, and an afferent cardiovascular feedback current. The equations governing the subthreshold dynamics of the j-th neuron are

$$(2.1) \qquad C_m \frac{dv_j}{dt} = -g_L(v_j - E_L) - g_K n_j^2(v_j - E_K) - g_M w_j(v_j - E_M) - I_{syn,j} - I_{cv,j}$$

$$(2.2) \qquad \tau_x \frac{dx_j}{dt} = x_\infty(v_j) - x_j$$

where t is time (in msec), v_j is the transmembrane potential (in mV); $x_j = n_j, w_j$ are the activation variables of the delayed-rectifier potassium current and the M-current, respectively (delayed-rectifier and M-current are expressed by many autonomic cardiac neurons, and the M-current is suspected to play a key role in shaping autonomic cardiac neurons firing dynamics [1, 30, 54, 84]); $I_{syn,j}$ is the intra-network synaptic current into the j-th neuron induced by pre-synaptic neurons; $I_{cv,j}$ is the synaptic afferent cardiovascular feedback current; C_m is the membrane capacitance, and g_L, g_K, g_M are the maximal conductances of the leakage, delayed-rectifier potassium and M-currents, respectively; E_L, E_K, E_M are the reversal potentials of the leakage and delayed-rectifier potassium and M-currents; $\tau_x = \tau_n, \tau_w$ are the time-constants for the activation variables, and the function $x_\infty(v)$ is the subthreshold steady-state activation of the activation variable x_j, given by the equation

$$w_\infty(v) = 1 / \left(1 + \exp \left(-\frac{v + 45}{2.4} \right) \right), \text{ and } n_\infty = 0.$$

When the transmembrane potential of a model neuron reaches a threshold potential (v_T), the neuron fires an action potential and the transmembrane potential is reset. Note that in the GIF model action potentials are not explicitly modeled. Each action potential can be thought

12

of as an instantaneous spike in membrane potential followed by a brief absolute refractory period (t_{ref}). Following the absolute refractory period, the transmembrane potential is set to a reset potential (v_{reset}), and the subthreshold dynamics (as described above) are resumed. To capture the effect of the action potential on the gating variables, n and w are updated to include the increase that would occur during a stereotypical spike. Specifically, when $v_j(t) = v_T$, the membrane potential and gating variables are updated to

$$v_j(t + t_{\mathrm{ref}}) = v_{\mathrm{reset}},$$

$$n_j(t + t_{\mathrm{ref}}) = n_j(t) + \Delta n$$

$$w_j(t + t_{\mathrm{ref}}) = w_j(t) + \Delta w.$$

To model the saturation of the gating variables (i.e. n and w must be between 0 and 1), the update values for the gating variables, Δn and Δw are scaled by $(1 - x_j(t))$:

$$\Delta x = (1 - x_j(t))(1 - \exp(-t_{\mathrm{ref}}/\tau_x)), \quad x = n, w,$$

2.1.2. Synaptic Dynamics. The synaptic dynamics throughout the neural circuit are modeled as alpha function synapses [**26**, **46**]. It is assumed that each time a presynaptic neuron fires there is a stereotypical increase and decrease in the synaptic conductance of the post-synaptic neuron of the form

$$\bar{g}_{\mathrm{syn}}\tilde{s}(t) = \frac{\bar{g}_{\mathrm{syn}}}{\tau_r + \tau_d}\left(e^{-t/\tau_d} - e^{-t/\tau_r}\right),$$

where $\bar{g}_{\mathrm{syn}}$ sets the maximal conductance; τ_r is the rise time constant ,and τ_d is the decay time constant. When the presynaptic neuron fires multiple times, the stereotypical increases and deceases in the post-synaptic conductance add linearly. Note that $\tilde{s}(t)$ is the solution to the linear differential equation:

$$\frac{d^2\tilde{s}}{dt^2} + (\tau_r^{-1} + \tau_d^{-1})\frac{d\tilde{s}}{dt} + \tau_r^{-1}\tau_d^{-1}\tilde{s} = 0, \quad \frac{d\tilde{s}}{dt}(0) = 1.$$

(i.e., the over-damped harmonic oscillator). Therefore, because the synaptic responses are assumed to add linearly, when the j-th neuron fires at times $t_{\text{spike,k}}$, its synaptic output $\overline{g}_{\text{syn}}s_j$ is given by

$$\frac{d^2 s_j}{dt^2} + (\tau_r^{-1} + \tau_d^{-1})\frac{ds_j}{dt} + \tau_r^{-1}\tau_d^{-1}s_j = 0$$

with update conditions

$$\frac{ds_j}{dt}\left(t_{\text{spike}}^+\right) = \frac{ds_j}{dt}\left(t_{\text{spike}}^-\right) + 1.$$

2.1.3. Network Connectivity & Inter-ICNS Synaptic Input. Within the ICNS network, there are excitatory and inhibitory synaptic connections [**69**] between ICNS neurons. Random recurrent connections from an excitatory presynaptic neuron j to a postsynaptic neuron k occur with probability $p_{\text{ICNS,e}}$ and from an inhibitory presynaptic neuron j to a postsynaptic neuron k with probability $p_{ICNS,i}$. Neurons are excitatory with probability p and inhibitory with probability $1 - p$. The inter-ICNS synaptic input current to the j-th neuron is

$$I_{syn,j} = \sum_{k=1}^{N} w_{k,j}^k g_{syn,f(k)} s_k (v_j - E_{syn,f(k)})$$

where $w_{k,j}^k$ are synaptic weights, and $E_{\text{syn,f(k)}}$ are the reversal potentials for the synaptic currents between neurons. The function $f(k)$ outputs e or i, depending on whether the k-th cell is excitatory or inhibitory. The synaptic weights $w_{k,j}$ were equal to 1 if neuron k synapses onto neuron j or equal to 0 if there was no connection. The maximal synaptic conductances $g_{\text{syn,e}}$ and $g_{\text{syn,i}}$ were chosen to approximate values from previous models [**45**, **72**, **81**]

2.1.4. Afferent Cardiovascular Feedback. To model afferent feedback from the cardiovascular system, each neuron in the ICNS receives independent periodically modulated stochastic input. The input is described by a non-stationary Poisson process with arrival function $\lambda(t)$ that determines the probability of firing times of the presynaptic afferent cardiovascular feedbck neurons that synapse onto the ICNS neurons. $\lambda(t)$ is a function with a period of 1000 msec (to approximate length of human cardiac cycle) with the qualitative shape of the left ventricular pressure curve (shown in figure 2.4) taken from the output of

14

a mechanical model of the heart (previous work from [**60, 77**]) described in a later chapter. The function is scaled to have a tonic value of A_t and an amplitude of A_p. This tonic input can be said to be a result of central drive to the ICNS. Figure 2.4 plots a single period of the periodic arrival function $\lambda(t)$ used to generate the spike times of the presynaptic input to a model GIF neuron.
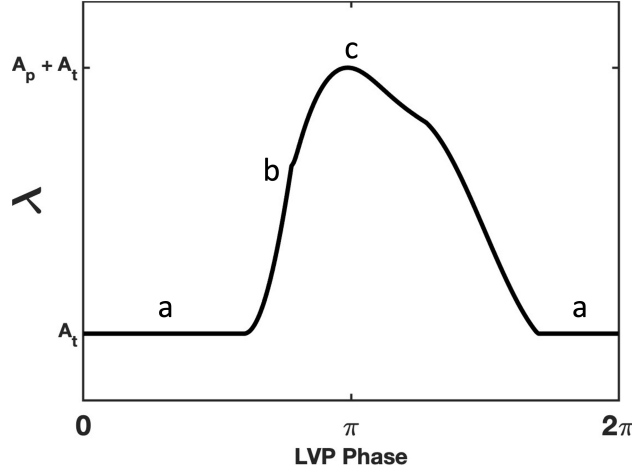

FIGURE 2.4. Periodic arrival function λ as a function of the phase of the cardiac cycle (with period $T = 1000$ msec) for the poisson process which generates the presynaptic spike times for the input to a model neuron. a: Diastole, b: Isovolumetric Contraction, c: Systole.

The afferent cardiovascular feedback synaptic input into the j-th neuron is described by

$$I_{cv,j} = \sum_{k=1}^{N} w_{k,j}^{cv} g_{syn,e} s_k (v_j - E_{syn,cv})$$

where $w_{k,j}^{cv}$ are synaptic weights, and $E_{\text{syn,cv}}$ is the reversal potentials for the synaptic currents of the network input. The reversal potentials $E_{\text{syn,e}}$ and $E_{\text{syn,i}}$ were chosen to approximate the values represented by nicotinic receptor and GABA receptor activation, respectively. As noted eaerlier, all parameter values are shown in Table 2.1 in appendix.

The network model was implemented for 10.5-minutes of simulated time with 30 seconds of recorded data omitted to account for transient dynamics. The level of tonic input is set to a constant value $A_t = 0.005$, with $r_{pt} = \frac{A_p}{A_t}$ drawn from a beta distribution $\beta(a, b)$ with parameters $a = b = 0.75$, and then scaled to have a maximum value of 1.5. The resulting

15

arrival function is given by $\lambda(t) = A_p y(t) + A_t$, and then A_p and A_t are adjusted so that the average firing frequency of the presynaptic afferent cardiovascular feedback neuron is 5.75 Hz.

GIF model parameters where set to elicit similar firing properties of autonomic cardiac neurons [72] (see figure 2.6) and are provided in Appendix Table 2.1. In all simulations thoughout this thesis, except when mentioned otherwise, parameters for the neurons were homogeneous; g_M was chosen from a uniform distribution with minimum and maximum values taken to approximate values from previous models [45]. The use of a GIF model introduces the possibility for accumulation of error due to spikes between time-steps. The use of linear interpolation to approximate firing times between time-steps is discussed in Appendix 2.5.3.

2.2. Model Reproduces Firing Activity Observed in ICNS

2.2.1. Response of Isolated ICNS Neurons to Constant Input. In Springer et al. 2015 [72], disassociated autonomic cardiac neurons were stimulated for 1000 msec with various magnitudes of input. Figure 2.5 plots the response of the autonomic cardiac neurons, displaying three types of firing: tonic, accommodating, and phasic. Tonic neurons fired repetitively at frequencies related to strength of stimulus. Accommodating neurons adapted and ceased firing at lower stimulus levels. Phasic neurons fired one to four spikes and ceased firing. Figure 2.6 plots the membrane potential of isolated GIF neurons with various levels of M-current in response to various magnitudes of constant current input $I_{syn,j} = I_{stim}$, $I_{cv,j} = 0$, for 1000 msec. For a fixed input current magnitude I_{stim}, the value of the maximal M-current conductance g_M dictated if the model GIF neuron displayed tonic, accomodating, or phasic firing. These simulations imply that the M-current is a possible mechanism for the tonic, accomodating, and phasic firing dynamics observed in autonomic cardiac neurons (shown in figure 2.5).
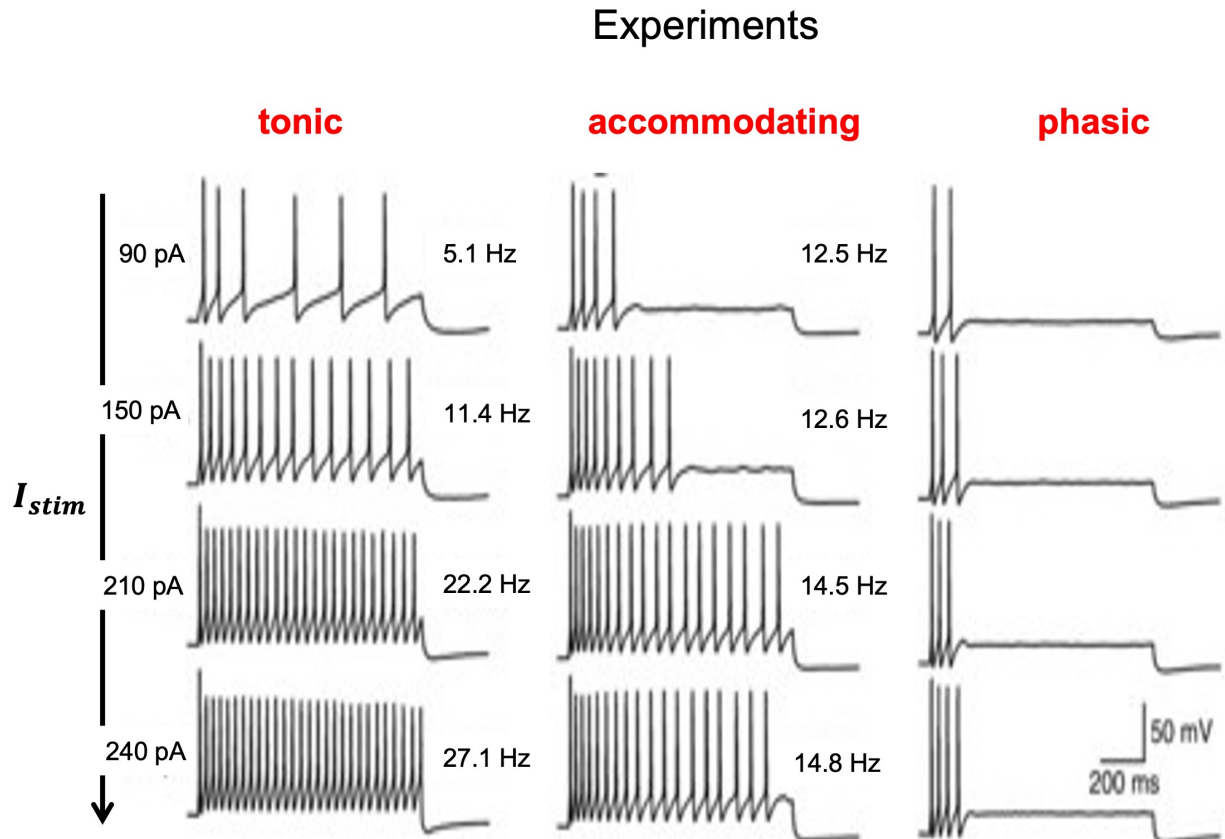
FIGURE 2.5. Disassociated autonomic cardiac neuron membrane potential recorded in Springer et al. 2015 ([**72**], figure 1) by using a 1000 msec stimulus with various amplitudes of current I_{stim}. Neurons displayed three types of firing: tonic, accommodating, and phasic. Tonic neurons fired repetitively at frequencies related to strength of stimulus. Accommodating neurons adapted and ceased firing at lower stimulus levels. Phasic neurons fired one to four spikes and ceased firing.

Model GIF Neurons

FIGURE 2.6. Single-cell GIF model neurons recorded by using a 1000 msec stimulus with various amplitudes of current I_{stim}. Neurons displayed three types of firing: tonic, accommodating, and phasic. Tonic neurons fired repetitively at frequencies related to strength of stimulus. Accommodating neurons adapted and ceased firing at lower stimulus levels. Phasic neurons fired one to four spikes and ceased firing. Variations in maximal M-current conductance (g_M) elicited a change in firing dynamics and provide a possible mechanism to explain the firing dynamics in Springer et al. 2015 [**72**] figure 1.
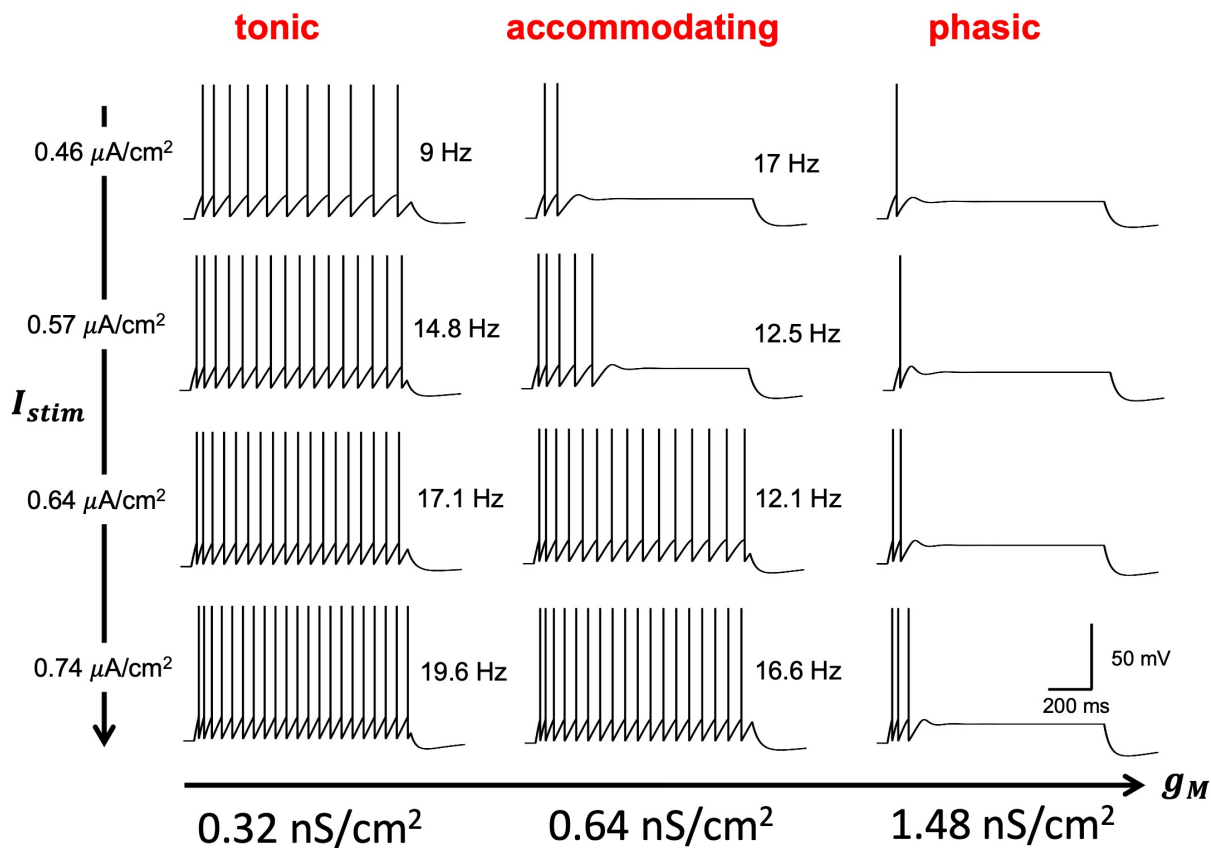
2.2.2. Response of ICNS Neurons to Afferent Cardiovascular Feedback. Next, the firing dynamics of neuronal network model neurons were subjected to periodic input that modeled the afferent cardiovacular feedback from the cardiovascular system shown in figure 2.4. (Note that all neurons in the analysis below had a firing frequency of at least 0.1 Hz). (Note also that all results of the ICNS network model in this chapter are taken from a single simulation, but similar results were obtained in many independent simulations). The "baseline frequency" of an ICNS neuron is defined as the average firing frequency of the neuron without any experimental intervention [**9**,**63**], i.e., the average firing frequency of the neuron without any stimulus application. The distribution of (baseline) firing frequencies of the ICNS network model neurons in figure 2.7c reproduces the distribution of firing frequencies of ICNS neurons observed experimentally. [**9**,**63**]

(a)   **(b)**   **(c)**
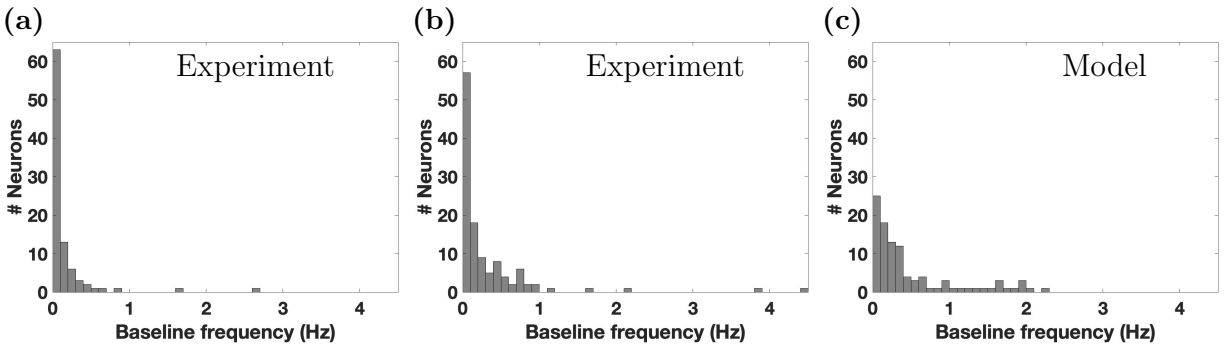
FIGURE 2.7. Distribution of frequency of action potentials at steady-state (baseline) from N neurons in the ICNS with a majority firing action potentials at less than 1Hz. (a) Data extracted from Beaumont et al. 2013 [**9**] with $N = 92$. (b) Data extracted from Rajendran et al. 2016 [**63**] with $N = 118$. (c) Firing frequency of ICNS network model neurons with $N = 100$.

Firing histograms were computed to analyze the firing behavior of the model neurons. To compute the firing histograms of a GIF neuron, the firing times (after the removal of the first 30 sec of data to account for transience) of the neuron are sorted into 10 bins representing 100msec each based on the phase of the LVP at the time of the spike. Figure 2.8 plots the firing histograms of 49 model GIF neurons from the ICNS network model similar to experimental data in figure 2.1. The overall firing dynamics of the GIF network model neurons

were very similar to those seen experimentally [**9**]. Figure 2.9 plots three firing histograms obtained from ICNS neuronal network model GIF neurons that express the three canonical firing types. Similar to the experimental data, follower neurons preferentially fire during systole with maximal probability near peak systole and phasic neurons fire predominantly during isovolumetric contraction. The firing of tonic neurons have no correlation with the phase of the cardiac cycle.
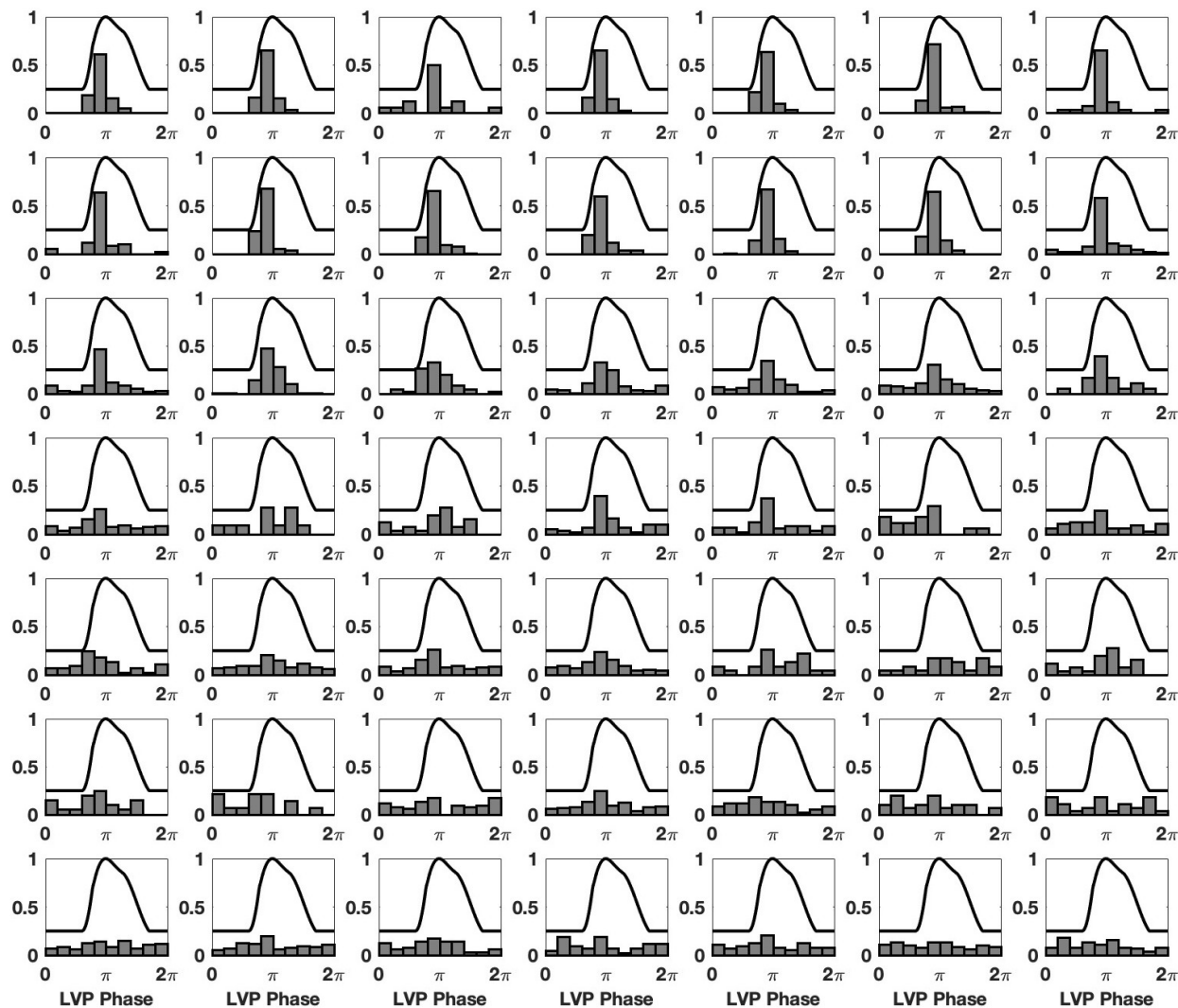

FIGURE 2.8. Neuronal firing histograms (probability density) with arrival function λ modeling LVP input to network. Data extracted from 49 out of 100 network model neurons with firing frequency at least 0.1 Hz over 10 minutes of simulated time. Vertical axis is probability density.
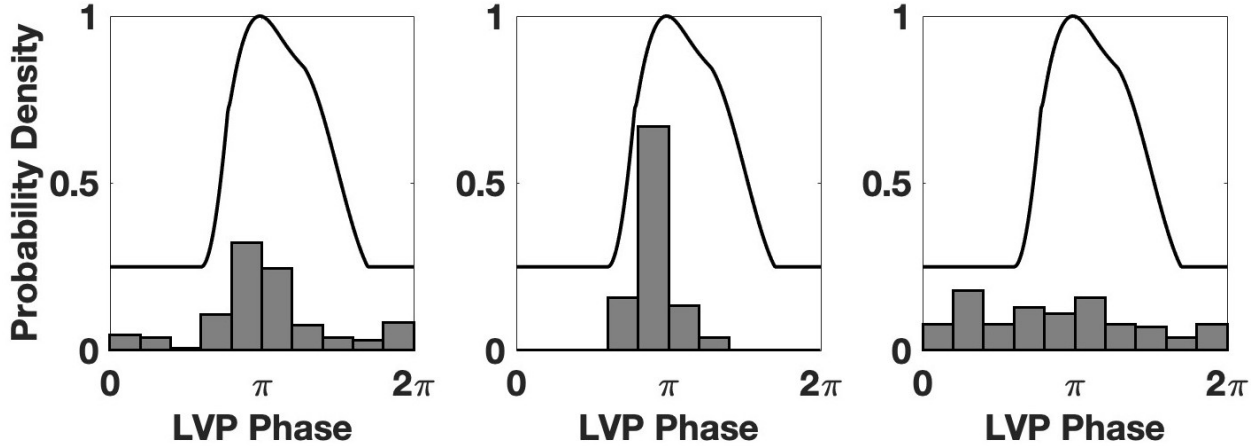
FIGURE 2.9. Probability density of 3 example model neurons (follower, phasic, and tonic neurons with data taken from the ICNS network model simulation) firing times as a function of the phase of the average left ventricular pressure. Solid curves indicate the LVP.

Many neurons in the network model can be distinctly categorized as one of the three canonical firing type,. however similar to the experimental data, there are also neurons that do not cleanly fit into any of the canonical firing types. Figure 2.10 plots three firing histograms from such neurons. The first neuron fires almost as a follower, but the firing profile is shifted so that the peak of the firing histogram is not aligned with peak systole. The second neuron fires as a mixture of a follower and a phasic neuron. The third neuron appears to share firinig properties with follower and tonic neurons. Like the experimental data, clustering analysis on the model data indicate a continuum of firing behavior rather than a distinct set of canonical firing types. The canonical firing types naturally arise from the GIF network model without any tuning of the network connectivity or a detailed model for intrinisic neuronal dynamics, and therefore the mechanisms (e.g., M-current, network connectivity, afferent cardiovascular feedback) included in the model are largely responsible for shaping firing in the ICNS.

21

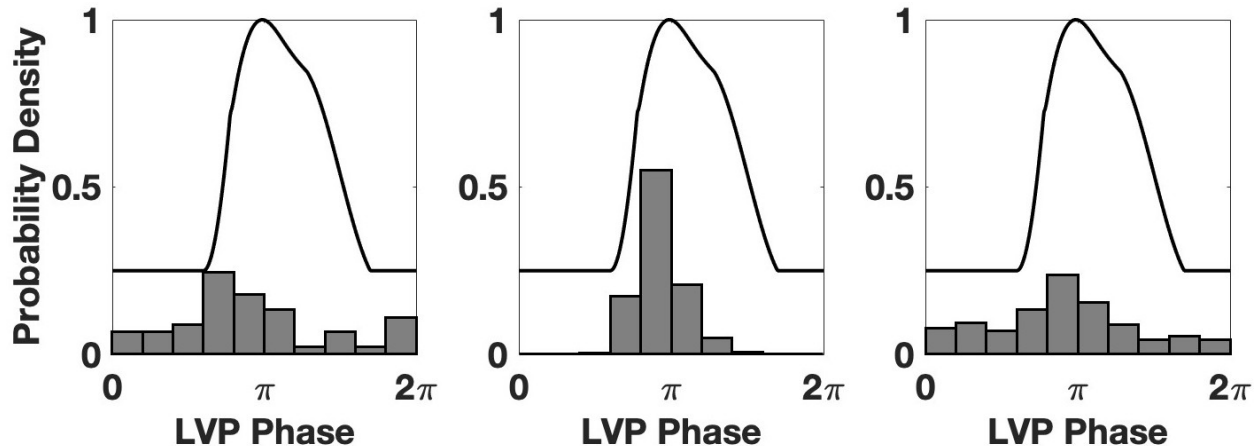FIGURE 2.10. Firing histograms of 3 example model GIF neurons firing times as a function of the phase of the average left ventricular pressure that do not fire clearly as phasic, follower, or tonic. Solid curves indicate the LVP function.

2.3. Mechanisms Underlying Firing Types of ICNS Neurons

Experimental data [9] and our network simulations suggest that there are three canonical neuronal firing types in the ICNS. However, the mechanisms underlying these canonical firing types are unclear. In this section, we suggest three mechanisms that can (individually or combined) bestow ICNS neurons with the canonical firing dynamics: excitatory input to ICNS neurons, the M-current in the neurons, and feed-forward inhibition. First, we show that the follower and tonic firing dynamics can be induced in an isolated model neuron by controlling the ratio of the amplitude of the periodic and tonic input that the neurons receieve,, and that both the M-current and feed-forward synaptic inhibition can change a model neuron's firing behavior from follower to phasic. We then assess the presence of these mechanisms in the ICNS network model.

2.3.1. The Influence of Periodic-to-Tonic Input Amplitude Ratio. The input that a cell receives clearly influences its firing properties. In this subsection, we consider an isolated GIF neuron without M-current that is subjected to tonic input and periodic afferent feedback from the cardiovascular system (schematic shown in figure 2.11, top), and that the ratio of the amplitude of a periodic portion of the arrival function A_p to the magnitude of the

22

tonic portion of the arrival function A_t dictates if the firing dynamics of a neuron resemble a tonic neuron, a follower neuron, or somewhere between.

Figure 2.11 (bottom) plots five firing histograms for values of $r_{pt} = A_p/A_t$ fromo 0 to 1.5, which are the simulatioin data of isolated model GIF neurons. When $r_{pt} = 0$ (i.e., there is no periodic input), the neuron fires in a manner independent of the cardiac cycle i.e. the canonical tonic firing type. As the value of r_{pt} is increased, the periodic portion of the input increases and firing types go from tonic to follower in a smooth fashion, but it is not clear when the model GIF neuron becomes a follower. Note that $r_{pt} = 1.5$ is the maximum value used in the network model.

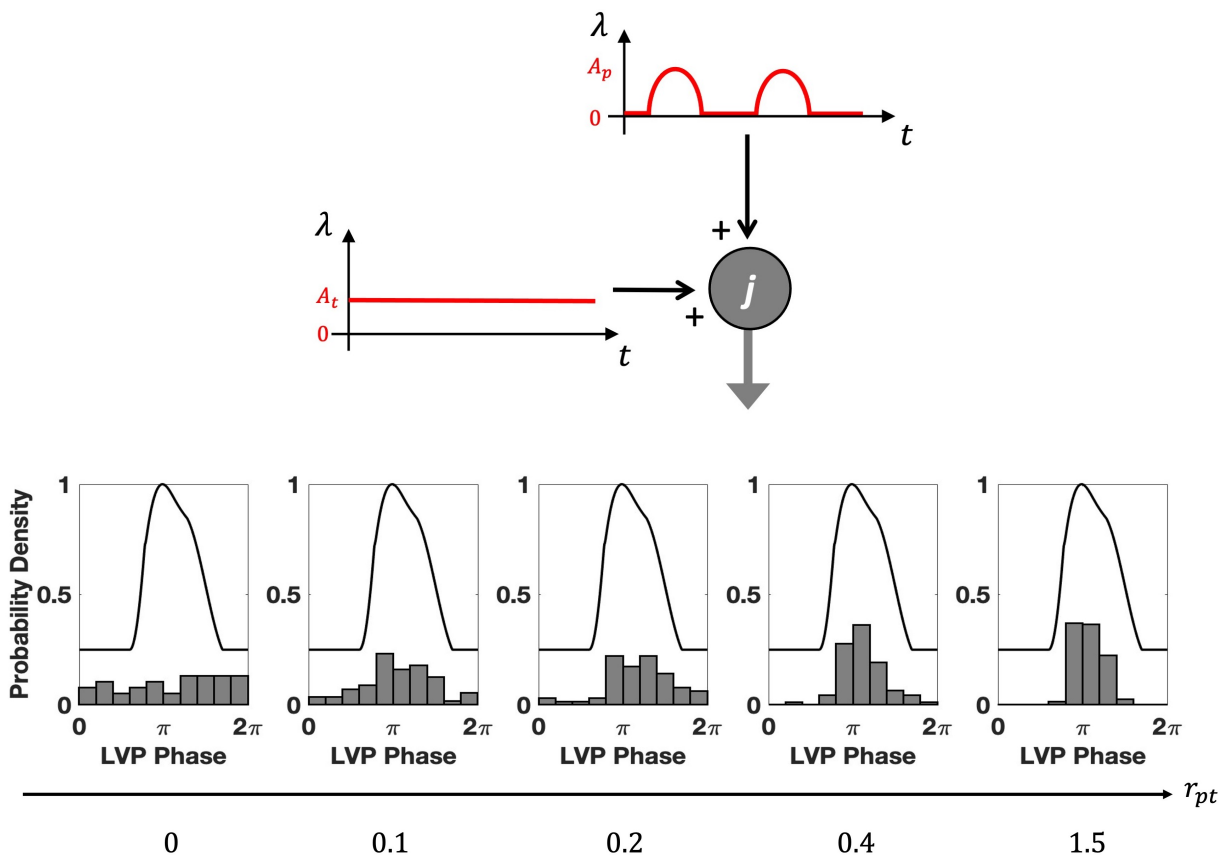FIGURE 2.11. (top) Motif of input received byiisolated GIF model neuron with no M-current ($g_M = 0$) that receive tonic and periodic input, according to the functin in figure 2.4. (bottom) Firing histograms for five values of $r_{pt} = A_p/A_t$. The value of r_{pt} dictates the firing type of the model neurons, low r_{pt} results in tonic firing and high r_{pt} results in follower firing.

Next, we check the network model neurons for tonic neurons, follower neurons, and those somewhere between and look at the corresponding values of r_{pt} to see if the input is dictating the firing types. Figure 2.12 plots firing histograms of GIF neurons from the network model simulation for various values of periodic-to-tonic amplitude ratio r_{pt} and maximal M-current conductance g_M. As in the case of the isolated neuron, the firing type of the neuron in the ICNS network model change from tonic to follower as the value of r_{pt} increases, with a continuum of firing types that display both tonic and follower-like behaviors. This implies that the periodic-to-tonic input amplitude ratio r_{pt} can induce tonic, follower, or somewhere between firing behavior in ICNS neurons.
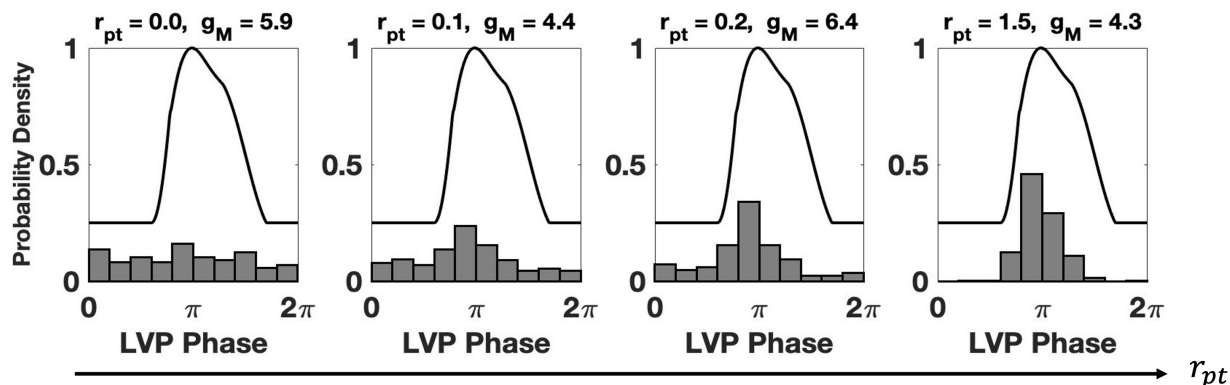
FIGURE 2.12. Firing histograms for neurons in the ICNS network model as a function of the cardiac phase. Similar to the isolated model neuron, the value of r_{pt} controls the firing behavior of the cells and can induce both tonic and follower-type firing.

2.3.2. The Influence of the M-Current. The M-current modulates the ability of cells to fire action potentials by effectively increasing the firing threshold of the membrane. The slow build-up of the M-current also leads to adaptation/accomodation, where the firing frequency of the neuron is decreases over time and can even stop firing. Thus, it is likely that the M-current plays a key role in the emergence of the canonical phasic firing type. We extend the results of the previous section on the influence of the input on the firing types of neurons and show that the M-current can change the firing type of a neuron from a follower to a phasic firing neuron. In this subsection, we first show that an isolated GIF neuron can be

changed from a follower to a phasic neuron when the M-current is included. We then check the network and assess if the phasic model neurons have a high value of maximal M-current conductance g_M and periodic-to-tonic input amplitude ratio r_{pt}, and if the follower neurons have a low value of g_M and a high value of r_{pt}.

Figure 2.13 shows the firing statistics of an isolated GIF model neuron for various values of periodic-to-tonic input amplitude ratio (r_{pt}) and maximal M-current conductance (g_M). When the maximal M-conductance g_M is small, the value of r_{pt} dictates the firing type of the neurons, as shown in figures 2.11 and 2.12. However, the firing behavior of follower neurons change as the maximal M-current conductance g_M is increased and begin to fire predoominantly during the isovlumetric contraction phase of the cardiac cycle. Tonic neurons behavior remains uncorrelated with the cardiac cycle as g_M increases. (Note that increasing the maximal conductance of the M-current g_M enough will suppress the model GIF neurons from firing at all.)
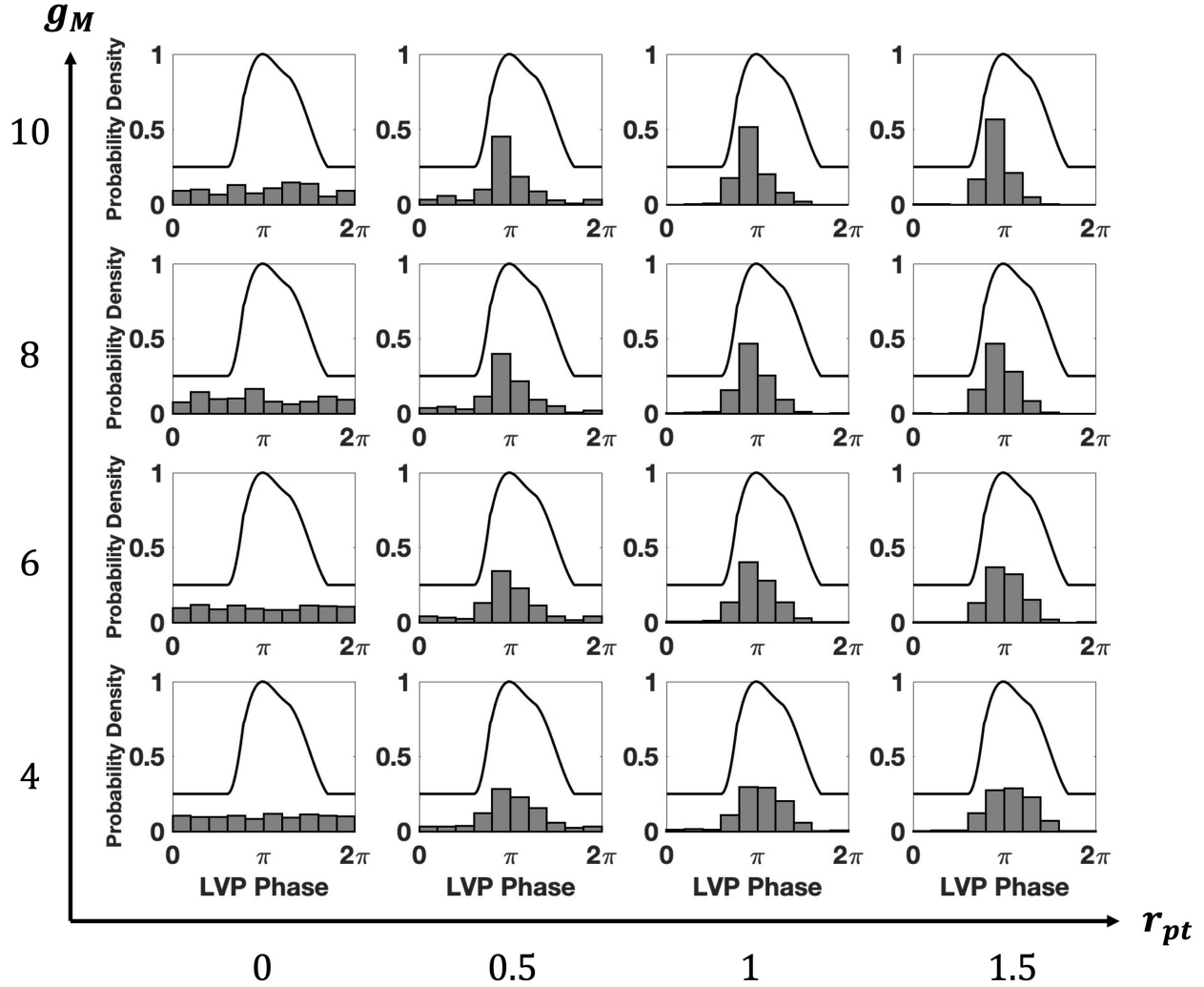
FIGURE 2.13. Firing histograms for an iisolated GIF neuron as a function of the phase of the cardiac cycle. The values of r_{pt} and g_M implemented are indicated on the horizontal and vertical axes. The horizontal axis corresponds to values of the ratio of periodic-to-tonic input amplitude magnitude r_{pt}, and the vertical axis corresponds to varying values of maximal M-current conductance values g_M. Solid curve indicates LVP.

Next, we check the ICNS network model neurons for tonic neurons, follower neurons, and phasic neurons. We look at the corresponding values of r_{pt} and g_M to see if the input and M-current are dictating the firing types. Figure 2.14 plots firing histograms of model GIF neurons picked from the ICNS network model to fit the structure of figure 2.13. As in the case of the isolated neuron, when the maximal M-current conductance g_M is small, the

value of r_{pt} dictates the firing type of the neuron, as shown in figures 2.11 and 2.12. However, the firing behavior of follower neurons changes to phasic firing as g_M is increased, while tonic neurons remain tonic. This implies that the combination of afferent cardiovascular feedback and M-current can bestow ICNS neurons with tonic, follower, and phasic firing types, or somewhere between.
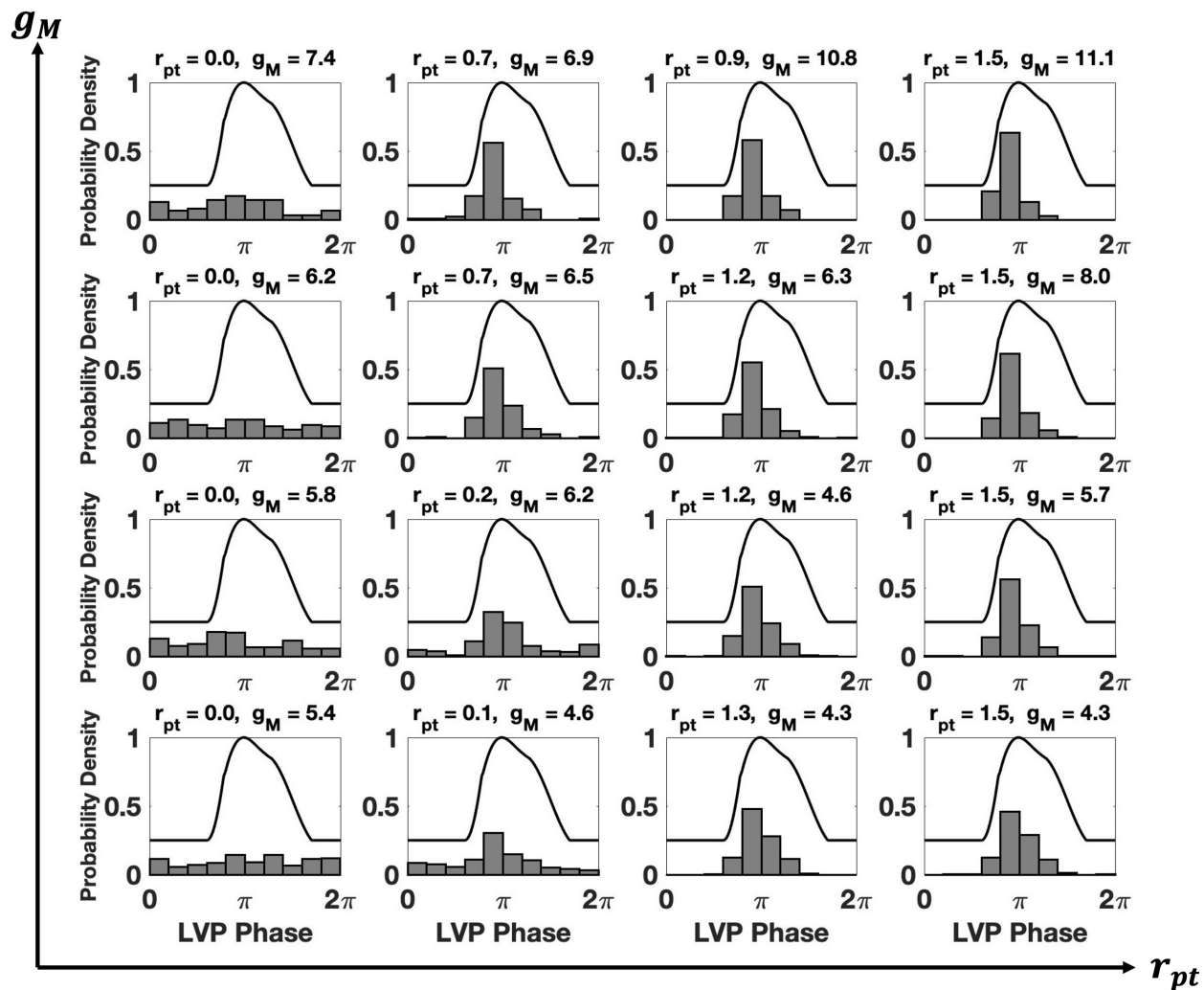
FIGURE 2.14. Examples of firing histograms from GIF neurons in the full ICNS network model, indicating firing times as a function of the phase of the cardiac cycle. The values of r_{pt} and g_M are indicated above subfigures. Firing histograms were picked to present a similar structure to the isolated GIF neurons in figure 2.13.

2.3.3. Role of Feed-Forward Inhibition. Intra-network connectivity can have a profound effect on the firing behaviors of neurons. Feed-forward inhibition is a fundamental motif in neural circuits [20], including in the autonomic nervous system [82]. Feed-forward inhibition can sculpt follower firing activity into canonical phasic firing behavior. Figure 2.15a shows a schematic of feed-forward inhibition. Cell 1 and cell 2 receive excitatory input with a high periodic-to-tonic amplitude ratio r_{pt}, which alone would elicit follower type behavior. However, after a delay, cell 2 supresses firing of cell 1 via inhibitory input, leading to cell 1 only firing at the onset of systole, i.e. during isovolumetric contraction.

Figure 2.15b plots the firing histogram of neuron 1 in the feed-forward inhibitory circuit (fir $g_M = 0$, $r_{pt} = 1.5$). We note that an increase in the maximal inhibitory conductance by a factor of 30 ($g_{\text{syn,i}} = 150$ nS/cm^2) was required to induce the change in firing behavior of neuron 1 from a follower neuron to a phasic neuron, but a sufficiently increased number of presynaptic neurons synapsing onto the post-synaptic target neuron will reproduce similar results without altering the maximal conductance parameter $g_{\text{syn,i}}$. We conclude that feed-forward synaptic inhibition is a possible mechanism for inducing a change in neuronal firing behavior from a follower neuron into a phasic neuron.
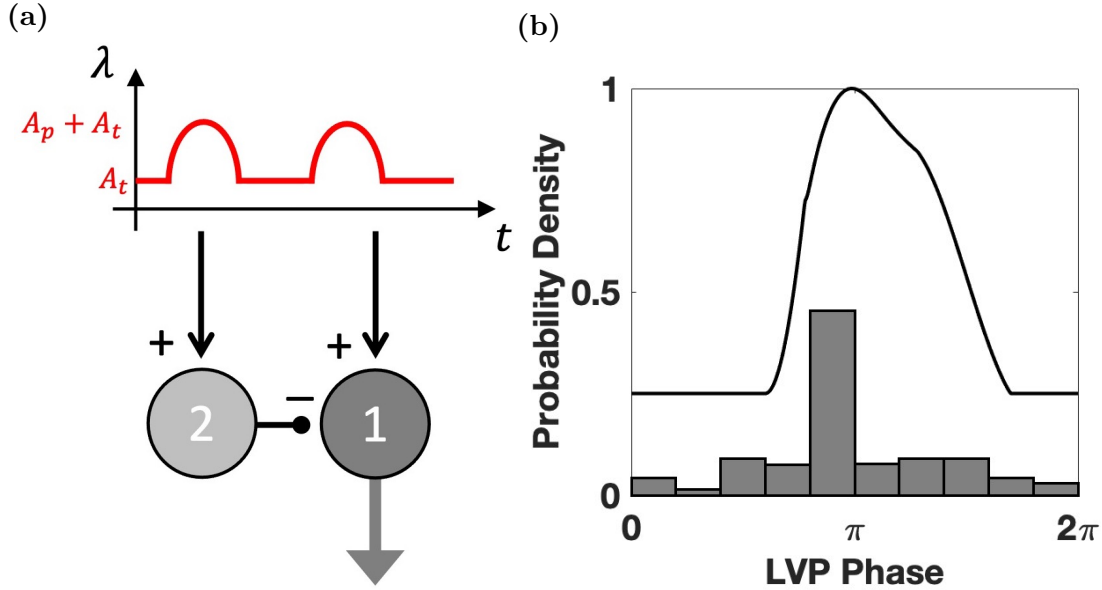
FIGURE 2.15. (a) Motif of suggested network connectivity that leads to phasic firing behavior. Both neurons 1 and 2 receive combined tonic and periodic excitatory input. Presynaptic neuron 2 induces inhibitory current in post-synaptic neuron 1. (b) Firing histogram of neuron 1 from 10-minutes of simulated time showing phasic firing behavior in responds to periodic and tonic input with inhibitory synaptic current from a follower neuron.

Examination of all phasic neurons in the ICNS network model indicates that feed-forward synaptic inhibition is not responsible for the phasic firing. While feed-forward synaptic inhibition is present, we see that on average, the magnitude of the inhibitory synaptic currents is not sufficiently large to induce phasic firing in a neuron. Note, however, that two possible parameter changes that could lead to feed-forward synaptic inhibition induced phasic firing: (1) increased maximal inhibitory synaptic conductance $g_{syn,i}$, and (2) increased probability of inhibitory connections $p_{ICNS,i}$ in the ICNS network.

2.4. Leakage Current and M-Current Combine to Counteract Slowly Varying Synaptic Currents on Average

We have demonstrated that the structure of the input and the presence of the M-current can combine to induce the three canonical firing types (follower, phasic, and tonic) in ICNS neurons. The structure of the input controls how much like a follower or a tonic firing pattern a neuron has, while an increase in the maximal conductance of the M-current g_M of a cell can reshape the neuron from a follower to a phasic neuron. In the analysis of these firing patterns, we observed an interesting phenomenon that is shown in figure 2.16. The combination of the M-current and the leakage current appear to (on average) counteract the slow variation in the input current related to the cardiac cycle, and therefore it is "faster" fluctuations in the input that appear to drive ICNS neurons to fire action potentials.

Figure 2.16 shows the firing histograms, averaged currents over the cardiac cycle, and total averaged currents over the cardiac cycle. Note that the combination of the M-current and the leakage current appear to counteract the "very slow" changes of the input current, but not the some of the higher frequency fluctuations, despite the difference in maximal M-conductances g_M. This implies that fluctuations of input over an intermediate range of frequencies are driving the firing of ICNS neurons. This leads us to question what properties the M-current bestow the model GIF neurons. This motivates our study in the next chapter: How does the combination of the leakage current and the M-current counteract slow variations in the synaptic current while allowing the fast varying components to drive the neuron to fire?
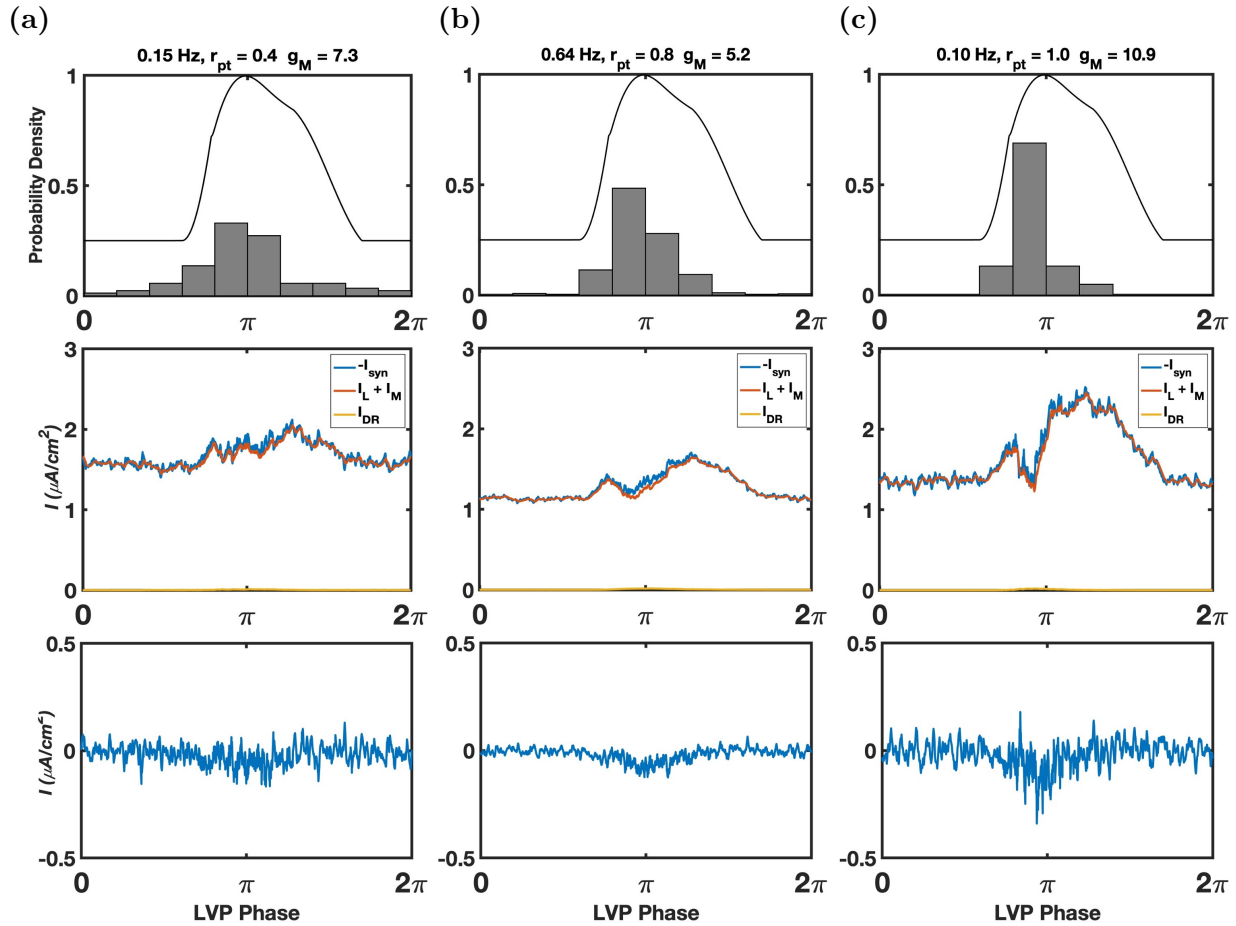
FIGURE 2.16. ICNS network model firing histograms, separated currents, and total current as functions of phase of cardiac cycle showing that the M-current and the leakage current combine to counteract the slowly varying synaptic input currents but respond to fast fluctutations. Top row: Firing histograms of (a) combined tonic/follower, (b) a follower, and (c) a phasic neuron, respectively with firing frequency, periodic-to-tonic amplitude ratio, and maximal M-current conductance labeled. Middle row: Average membrane currents over the periods of the cardiac cycle the neuron fired an action potential, Bottom row: Total membrane currents over the periods of the cardiac cycle the neuron fired an action potential.

2.5. Appendix

2.5.1. Parameters.

Parameter	Value	Parameter	Value
C	0.77 μF/cm^2	$E_{syn,C}$	0 mV
g_L	0.1 nS/cm^2	τ_n	75 ms
g_K	100 nS/cm^2	τ_w	165 ms
$g_{M,max}$	12 nS/cm^2	τ_r	2 ms
$g_{M,min}$	4 nS/cm^2	τ_d	4 ms
$g_{syn,e}$	5 nS/cm^2	v_{reset}	-68 mV
$g_{syn,i}$	5 nS/cm^2	v_T	-52 mV
E_L	-70 mV	$p_{\text{ICNS,e}}$	$4\log(100)/99$
E_K	-90 mV	$p_{\text{ICNS,i}}$	$8\log(100)/99$
$E_{syn,e}$	0 mV	p	0.7
$E_{syn,i}$	-90 mV	t_{ref}	0.5 ms

TABLE 2.1. Table of parameter values used for cell-based ICNS network model.

2.5.2. Clustering Analysis of ICNS Neurons.

To rigorouosly determine if the firing types of ICNS neurons can be cleanly separated into different categories, we perform clustering analysis. Because the firing histograms are $2\pi-$periodic, it is necessary to implement directional statistics [61]. The first moment of a firing histogram is a vector representing the mean firing behavior of the neuron, with respect to the phase of the cardiac cycle. The angle of the first moment θ_1 is the average phase of the cardiac cycle a neuron fires at, and the magnitude of the first moment R_1 provides a measure of the "spread" of a neurons firing - $R_1 = 0$ indicates a perfectly uniform tonic neuron and $R_1 = 1$ indicates a neuron that only fires at a single phase of the cardiac cycle, i.e., a perfectly phasic neuron.

The angle θ_1 and magnitude R_1 of the first moment for each of the ICNS neuronal firing histograms from figure 2.1, and for the firing histograms computed from the network model from figure 2.8 were computed. Figures 2.17a and 2.17b aree scatter plots of the magnitude of the first moment versus the angle of the first moment of the experimental firing-histograms and the model firing histograms, respectively. The distribution of the angle and magnitude of first moments does not have obvious clusters that correlate to the three canonical firing types.

To quantitatively confirm that no clusters exist, two types of clustering algorithms (k-means with $k = 3, 4, 5$ & hierarchical) were used on (1) the (θ_1, R_1) dataset computed from the firing-histograms in figure 2.1 and (2) the (θ_1, R_1) dataset computed from the firing-histograms of the ICNS network model in figure 2.8. Indeed, the results from the clustering analysis did not show any distinction between the firing-histograms. However, we note that even when we restricted our dataset to only those firing histograms that we thought clearly display phasic, follower, or tonic firing patterns, our clusteriing failed to produce a quantifiable way of sorting the firing histograms. k-means (with $k = 3, 4, 5$) and hierarchical clustering methods were repeated using the angle and magnitudes of the first N moments for $N = 1, 2, 3, 4$ but results did not indicate a clear grouping. This implies that the clustering methods were not good enough, and future work is needed to improve the analysis.

The sparse distribution of the (θ_1, R_1) data and lack of quantifiable differences between canonical firing types implies that there is a continuum of firing behaviors among the experimental recordings and the ICNS network model neurons. Note that the scatter plot of the model firing-histograms shown in figure 2.17b over-represents the high magnitude R_1 neurons concentrated near $\theta_1 = \pi$, compared to the experimental data. This over-representation could be changed with an alteration of the distribution of periodic-to-tonic amplitude ratio r_{pt} values of the model neurons.
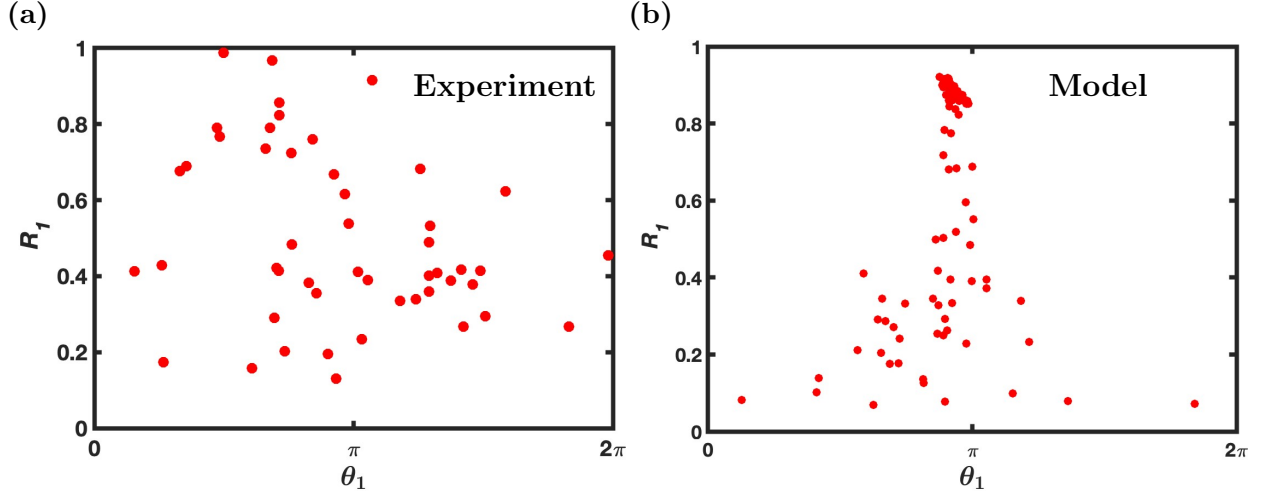
FIGURE 2.17. Scatter plot of magnitude of first moment R_1 versus angle of first moment θ_1 of neurons. (a) Experiment: Directional statistics computed from the firing-histograms recorded and presented in Beaumont et al. 2013 [9] figure 8. (b) Model: Directional statistics computed from the firing-histograms of the cell-based network model.

2.5.3. Numerical Methods. The reset dynamics in the integrate-and-fire model used in the mathematical model of the ICNS allow for numerical errors each time a spike occurs between time-steps. To account for this, we adapt a spike time approximation method introduced by Shelley, M and Tao, L [68]. The method is a modified Runge-Kutta 2 method that uses the standard RK2 method until a neuron fires, and then uses linear interpolation to approximate the firing time between steps.

The following description details the standard RK2 method implemented between spikes. With several assumptions, we are able to exploit the structure of our system (i.e., the linear equations) and analytically solve for n^i, s^i, and u^i at each time step, which simplifies the numerical method used. (Note here that we are using a superscript to denote the i-th neuron for the sake of notational ease.) First, we define $n_\infty = 0$, and thus for any initial condition $n^i(t_0) = n_0^i$,

$$(2.3) \qquad n^i(t) = n_0^i e^{-\frac{t-t_0}{\tau_{n_i}}}, \quad t \geq t_0$$

34

To explicity solve for s^i and u^i, let

$$x^i = \begin{bmatrix} s^i \\ u^i \end{bmatrix}$$

Then we can write the coupled differential equations for s^i and u^i as

$$\frac{d}{dt}x^i = Lx^i, \quad x^i(t_0) = x_0^i.$$

where

$$L = \begin{bmatrix} 0 & 1 \\ -\alpha\beta & -(\alpha+\beta) \end{bmatrix}$$

is a diagonalizable matrix such that $P^{-1}LP = \Lambda$, where $P = [\ p_1 \mid p_2\ ]$ is a matrix of the eigenvectors of L and Λ is a diagonal matrix of eigenvalues of L.

Let $y^i = P^{-1}x^i$, and note that by substitution,

$$\frac{d}{dt}y^i = P^{-1}\frac{d}{dt}x^i = P^{-1}Lx^i = P^{-1}LPy^i = \Lambda y^i.$$

Since Λ is diagonal, the solution to this system of ODEs is givem by

$$y = e^{\Lambda t}y_0^i,$$

and by substituting back in,

(2.4) $$\qquad\qquad x^i(t) = Pe^{\Lambda t}P^{-1}x_0^i, \quad t \geq t_0$$

Consider an initial time $t = t_0$. Then, the standard RK2 method (with exact solutions for n, s, and u) gives the $(m+1)th$ state variable time step, i.e., $t_m = t_0 + (m+1)\Delta t$ as

$$v^i_{m+1} = v^i_m + \frac{\Delta t}{2}(k^i_{v,1} + k^i_{v,2})$$

$$n^i_{m+1} = e^{-\frac{\Delta t}{\tau n_i}} n^i_m$$

(2.5)

$$x^i_{m+1} = P e^{\Lambda \Delta t} P^{-1} x^i_m$$

$$w^i_{m+1} = w^i_m + \frac{\Delta t}{2}(k^i_{w,1} + k^i_{w,2}).$$

Let $\frac{dv^i}{dt} = f(v^i, n^i, s^i, w^i)$, and $\frac{dw^i}{dt} = g(v^i, w^i)$. We define $k^i_{v,1}$, $k^i_{v,2}$ and $k^i_{w,1}$, $k^i_{w,2}$ be such that

$$k^i_{v,1} = f(v^i_m, n^i_m, s^j_m)$$

$$k^i_{v,2} = f(v^i_m + k^i_{v,1}\Delta t, n^i_{m+1}, s^j_{m+1}, w^i_m + k^i_{w,1}\Delta t)$$

(2.6)

$$k^i_{w,1} = g(v^i_m, w^i)$$

$$k^i_{w,2} = g(v^i_m + k^i_1 \Delta t, w^i_m + k^i_{w,1}\Delta t).$$

Next, we describe the method used to approximate the spike time between time steps and how this is incoporated into the RK2 method .Consider an integer m and a neuron i such that $v^i_m < v_{\text{threshold}} \leq v^i_{m+1}$. We first approximate the time $t = t_s$ such that

$$v^i(t_s) = v_{\text{threshold}}.$$

To do this, we set up a linear interpolation between v^i_m and v^i_{m+1}:

$$v(t) = \left(\frac{v^i_{m+1} - v^i_m}{\Delta t}\right) t + (1+m)v^i_m - m v^i_{m+1},$$

where $v(t_m) = v^i_m$ and $v(t_{m+1}) = v^i_{m+1}$. Then t_s must satisfy

$$v_{\text{threshold}} = \left(\frac{v^i_{m+1} - v^i_m}{\Delta t}\right) t_s + (1+m)v^i_m - m v^i_{m+1}.$$

36

Now that we know our spike time, let $dt_1 = t_s - m\Delta t$ and $dt_2 = (m+1)\Delta t - t_s$. We can calculate the values of our variables at the time of the spike (including the reset dynamics) by simulating the evolution of the exact equations and then adding our reset dynamics, and exploiting the fact that our method forces v^i to reset:

$$v^i(t_s) = v_{\text{reset}}$$

$$n^i(t_s) = e^{-\frac{dt_1}{\tau_{n_i}}} n^i_m + dn^i$$

$$x^i(t_s) = Pe^{\Lambda dt_1}P^{-1}x^i_m + \begin{bmatrix} 0 \\ 1 \end{bmatrix}$$

$$w^i(t_s) = w^i_m + \frac{dt_1}{2}(k^i_{w,1} + k^i_{w,2}) + \Delta w^i_m$$

where Δw^i_m is a saturation factor $\Delta w = (w-1)(e^{-\frac{1}{\tau_w}} - 1)$ to account for the M-current activation occuring up until the spike. To find the values at $t = t_m$, we use an classic RK2 step from $t = t_s$ to $t = t_{m+1} = (m+1)\Delta t$ for v^i by recalculating $k^i_{v,1}$, $k^i_{v,2}$ and $k^i_{w,1}$, $k^i_{w,2}$ and changing our initial conditions for the variables we have explicit solutions for,

$$v^i_{m+1} = v_{\text{reset}} + \frac{dt_2}{2}(k^i_1 + k^i_2)$$

$$n^i_{m+1} = n^i(t_s) + e^{-\frac{dt_2}{\tau_{n_i}}} dn^i$$

$$x^i_{m+1} = x^i(t_s) + Pe^{\Lambda dt_2}P^{-1}\begin{bmatrix} 0 \\ 1 \end{bmatrix}$$

$$w^i_{m+1} = w^i(t_s) + \frac{dt_2}{2}(k^i_{w,1} + k^i_{w,2}) + \Delta w^i(t_s)$$

After this calculation, we continue our RK2 method until another spike occurs.

CHAPTER 3

M-Current Induces Band-Pass Filter Behavior In ICNS Neurons

Neurons response to input changes with different frequency components [**19**, **23**]. This property is called low-pass, high-pass, or band-pass filtering, depending on the frequency components that provoke the largest response from the neuron. The filtering properties of a neuron provides a mechanism for information processing at the single neuron level [**16**].

In the previous chapter, we observed that, on average, the combination of the leakage current and the M-current appear to counteract the "slow" ($\sim$ 1 Hz) variations in input current related to the cardiac cycle, while "fast" fluctuations in the input current drive the model neurons to fire. This behavior seems different than the canonical neuron, which acts as a low-pass filter [**19**, **23**, **48**, **50**, **56**], i.e. the "response" of the neuron is largest to low-frequency inputs. In this chapter, we analyze the effect that the M-current has on the response of the model neuron to fluctuations in synaptic current, and show that the addition of the M-current endows the GIF model neuron with band-pass filter properties and a resonant frequency.

This chapter is outlined as follows. First, we introduce a non-dimensional model of a single GIF model neuron. We then show, through simulation results, that the GIF model neuron (with M-current) acts as a band-pass filter with a resonant frequency. For context, the input-output gain of a Leaky Integrate-and-Fire (LIF) neuron (i.e. without M-current) as a function of the frequency of oscillatory input is shown to be monotonically decreasing. Next, we exploit time-scale differences in GIF model neurons with M-current to asymptotically approximate the input-output gain as a function of the frequency of oscillatory input. Analysis of the eigenvalues of the equilibria of GIF model neurons indicates that the resonant

properties of the GIF model neuron is not caused by the standard mechanism for linear oscillators, i.e. the natural frequencies of the model neuron do not interact with oscillatory input to induce resonant behavior. To understand how the activation properties of the M-current induces the band-pass filter and resonant properties of the GIF model neuron, perturbations are made to the steady-state activation function of the M-current. (All numerical simulations were computed using MATLAB R2022b.)

3.1. Filtering Properties of GIF Model Neuron with M-Current

We study the filtering properties of the GIF model neuron in the subthreshold regime. We need to include the M-current because, unlike the DR-current, it is substantially activated at subthreshold potentials [**14**, **17**]. Therefore, this allows us to remove the spike and reset conditions of the GIF model neuron as well as the DR-current. Thus, we only need to consider a reduced neuronal membrane model

(3.1)
$$C\frac{dv}{dt} = -g_L(v - E_L) - g_M M(v - E_K) + I_{\text{inp}}(t)$$
$$\tau_M\frac{dM}{dt} = M_\infty(v) - M,$$

Despite the non-linearity in the model due to the M-current we want to understand how the neuron responds to different frequencies, slow and fast. To model this, synaptic input of the form

$$I_{\text{inp}}(t) = A_0(1 + \sin(2\pi\omega t))$$

is implemented, where ω is the frequency of the input, and A_0 is the amplitude of the oscillations of the input current and also the mean of the input current.

We nondimensionalize the system by setting $v = (E_L - E_K)\tilde{v} + E_L$, $t = \tau\tilde{t} = \frac{C}{g_L}\tilde{t}$ where $\tau = C/g_L$ is the membrane time constant, and $\tilde{M}_\infty(\tilde{v}) = M_\infty(v)$. Note that M is the fraction

of open M-channels and thus is already nondimensional. The nondimensional system is

$$\frac{d\tilde{v}}{d\tilde{t}} = -\tilde{v} - \tilde{g}_M M(\tilde{v} - \tilde{E}_K) + \tilde{A}_0(1 + \sin(2\pi\tilde{\Omega}\tilde{t}))$$

(3.2)

$$\frac{dM}{d\tilde{t}} = \epsilon(\tilde{M}_\infty(\tilde{v}) - M)$$

where $\tilde{g}_M = g_M/g_L$, $\tilde{A}_0 = A_0/[g_L(E_L - E_K)]$, $\tilde{\Omega} = \omega\tau$, $\tilde{E}_K = -1$, and $\epsilon = \tau/\tau_M$. The parameter values g_L, E_L, E_K, C, and τ_M are set to the values provided in the appendix of chapter 2. The value $\tilde{A}_0 = 0.45$ was chosen so that the membrane potential of the nondimensional LIF neuron (i.e $\tilde{g}_M = 0$) approached close to but did not surpass the firing threshold $\tilde{v}_T = 0.9$.

The analysis in this chapter is based on the set value $\tilde{A}_0 = 0.45$. The effect of the M-current on the GIF model neuron is decreased if $\tilde{A}_0$ is decreased. If $\tilde{A}_0$ is increased, the membrane potential surpassed the firing threshold $\tilde{v}_T$ and superthreshold dynamics had to be reintroduced.

The form $\tilde{I}_{\text{inp}} = \tilde{A}_0(1 + \sin(2\pi\tilde{\Omega}\tilde{t}))$ of input was chosen so that only excitatory input to the model GIF neuron was included. Figure 3.1 provides an example of the membrane potential of the GIF model neuron ($\tilde{v}$) and the activation of the M-current (M) in response to the oscillatory input current $\tilde{I}_{\text{inp}}$ with frequency $\tilde{\Omega} = 0.007727$ (1 Hz).
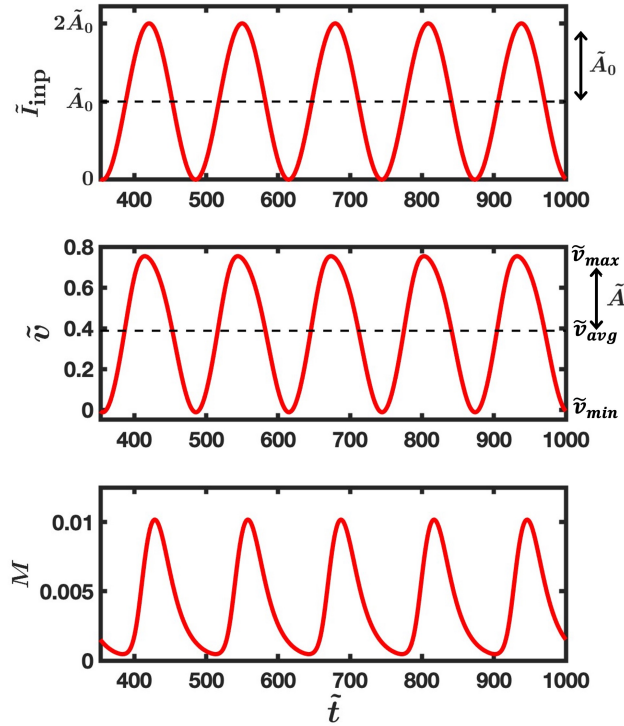
FIGURE 3.1. Basic response of GIF model neuron to input current $\tilde{I}_{\text{inp}}$, with amplitude $\tilde{A}_0 = 0.45$, input frequency $\tilde{\Omega} = 0.007727$, and magnitude of M-current $\tilde{g}_M = 10$. Oscillations in input current induce oscillations in both membrane potential $(\tilde{v})$ and activation of M-current (M) at the same frequency. The average membrane potential is $\tilde{v}_{\text{avg}} = 0.3873$. $\tilde{A}$ is the amplitude of the oscillations in $\tilde{v}$. The gain of the neuron is defined to be $\tilde{G} = \tilde{A}/\tilde{A}_0$.

To study the response of the model neuron to varying input, $\tilde{A}$ is defined in figure 3.1 as the amplitude of the oscillations of the membrane potential of the model neuron $\tilde{v}$

$$\tilde{A} = \frac{\tilde{v}_{\text{max}} - \tilde{v}_{\text{min}}}{2}$$

where $\tilde{v}_{\text{max}}$ and $\tilde{v}_{\text{min}}$ are the maximum and minimum values, respectively, of the nondimensional membrane potential $\tilde{v}$ periodic response. The gain $\tilde{G}$ of the system in response to the input $\tilde{I}_{\text{inp}}$ is defined in figure 3.1 as the ratio of the amplitude of the oscillations of the

41

membrane potential $\tilde{A}$ to the amplitude of the oscillations of the synaptic input $\tilde{A}_0$

$$\tilde{G} = \frac{\tilde{A}}{\tilde{A}_0}.$$
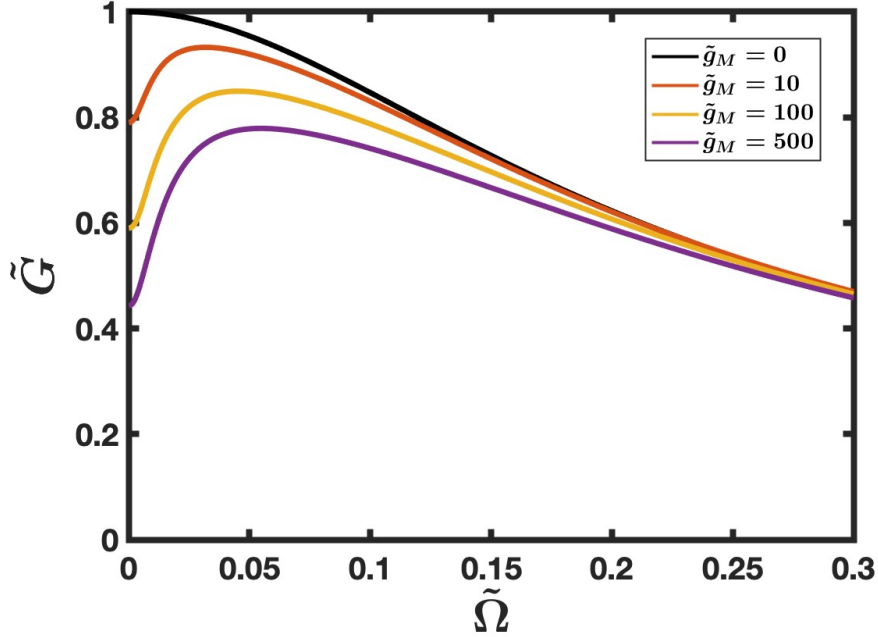
FIGURE 3.2. Gain $\tilde{G} = \tilde{A}/\tilde{A}_0$ of the GIF model neuron with various magnitude of M-current values $\tilde{g}_M$ as a function of the frequency $\tilde{\Omega}$ of the periodic input with amplitude $\tilde{A}_0$. The nondimensionalization of the input frequency is given by $\tilde{\Omega} = \omega\tau \approx 7.727\omega$ where ω has the units kHz. Note the "resonance frequency" occurs at $\tilde{\Omega} \approx 0.03 - 0.05$, or about $4 - 7$ Hz. The frequency associated with the M-current is $1000/\tau_M \sim 6$ Hz.

Figure 3.2 plots the gain $\tilde{G}$ of the GIF neuron as a function of the input frequency $\tilde{\Omega}$ for various values of the magnitude of the M-current $\tilde{g}_M$. Increasing the M-current ($\tilde{g}_M > 0$) decreases the gain at low frequencies, altering the response from a low-pass filter (at $\tilde{g}_M = 0$) to a band-pass filter. The decrease of the gain $\tilde{G}$ at low input frequencies $\tilde{\Omega}$ increases as a function of the magnitude of the M-current $\tilde{g}_M$. Furthermore, the resonance peak (maximized value of gain curve $\tilde{G}$) emerges at a resonance frequency of $\tilde{\Omega} \approx 0.03 - 0.05$, corresponding to $4 - 7$ Hz. The frequency associated with the M-current is $1000/\tau_M \sim 6$ Hz, implying that the resonance peak is due to the M-current.

The input related to the cardiac cycle discussed in the previous chapter oscillates at 1Hz ($\tilde{\Omega} \approx 0.007727$). The gain curves plotted in figure 3.2 suggest that the M-current reduces the response of the GIF model neuron to input oscillating at this frequency, while frequencies between $4 - 7$ Hz result in a larger response from the GIF model.

In the next section, we show that the LIF neuron ($\tilde{g}_M = 0$) acts as a low-pass filter to provide context for the analysis of the influence the M-current has on the gain of the GIF model as a function of the input frequency.

3.2. Leaky Integrate-and-Fire Neuron Acts as a Low-Pass Filter

The Leaky Integrate-and-Fire (LIF) model, which is often used to model neuronal activity [25,48,50,56], is known to act as a low-pass filter [47,73]. The LIF model corresponds to the GIF model without M-current ($\tilde{g}_M = 0$). Therefore, to provide context, we review the filtering properties of the LIF neuron, and then show how the addition of the M-current endows the GIF neuron with band-pass filter properties.

The voltage response of the nondimensional GIF model with no M-current ($\tilde{g}_M = 0$, LIF model) to periodic input $\tilde{A}_0(1 + \sin(2\pi\tilde{\Omega}\tilde{t})$ is given by

$$\tilde{v}(\tilde{t}) = \frac{\tilde{A}_0}{\sqrt{1 + 4\pi^2\tilde{\Omega}^2}} \sin\left(2\pi\tilde{\Omega}\tilde{t} + \tan^{-1}\left(-2\pi\tilde{\Omega}\right)\right) + \tilde{A}_0,$$

where a transient exponential decay term has been omitted. The amplitude of the oscillations in voltage is $\tilde{A} = \frac{\tilde{A}_0}{\sqrt{1+4\pi^2\tilde{\Omega}^2}}$, and thus the gain of the model in response to the fluctuating synaptic input is given by

$$(3.3) \qquad\qquad \tilde{G}(\tilde{\Omega}) = \frac{1}{\sqrt{1 + 4\pi^2\tilde{\Omega}^2}}.$$

Note that the gain is monotonically decreasing in $\tilde{\Omega}$, confirming that the LIF model is a low-pass filter. The maximum gain of 1 obtained with constant input, and the "cutoff frequency" (where the gain $\tilde{G}$ reaches ~ 0.707 its maximum value [85]) is $\tilde{\Omega}_c = 0.1592$, corresponding

to ~ 20 Hz. Figure 3.3 plots the gain curve of the LIF model as a function of the input frequency $\tilde{\Omega}$.
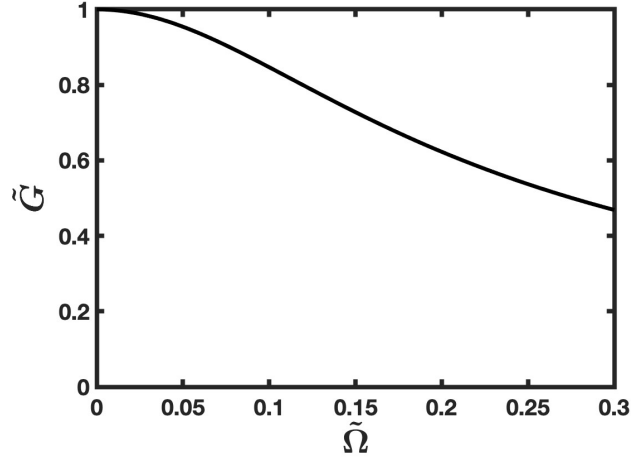

FIGURE 3.3. Gain $\tilde{G} = \tilde{A}/\tilde{A}_0$ of the LIF model neuron, i.e. the GIF model neuron with no M-current ($\tilde{g}_M = 0$) as a function of the frequency $\tilde{\Omega}$ of the oscillatory input with an amplitude and mean of $\tilde{A}_0$. LIF model neuron acts as a low-pass filter with cutoff frequency of $\tilde{\Omega} \approx 0.16$, i.e., approximately 20 Hz.

3.3. The M-Current Induces Band-Pass Filter Properties: Asymptotic Approximations of Gain as a Function of Input Frequency

In this section, we exploit the difference in time-scales of the membrane τ, the M-current τ_M, and the synaptic input $1/\tilde{\Omega}$ in the GIF neuron and use perturbation theory to show that: (1) For sufficiently low input frequency $\tilde{\Omega} = \mathcal{O}(\epsilon^2)$, the gain $\tilde{G}$ is larger than the limit of the gain $\tilde{G}$ as $\tilde{\Omega} \to 0^+$. (2) For sufficiently high input frequency $\tilde{\Omega} = \mathcal{O}(1)$, the M-current does not have a substantial effect on the gain, i.e., the gain behaves similarily to the LIF model gain. Figure 3.4 shows a schematic of this method - the increase of the gain at $\tilde{\Omega} \sim \epsilon^2$ and decrease of the gain at $\tilde{\Omega} \sim 1$ (similar to the decrease of the LIF gain) implies that the resonance peak must occur at $\tilde{\Omega} \sim \epsilon$, confirming what the simulation results in section 3.1 suggest: The M-current induces band-pass filter behavior in the GIF neuron with a resonance frequency at order ϵ.
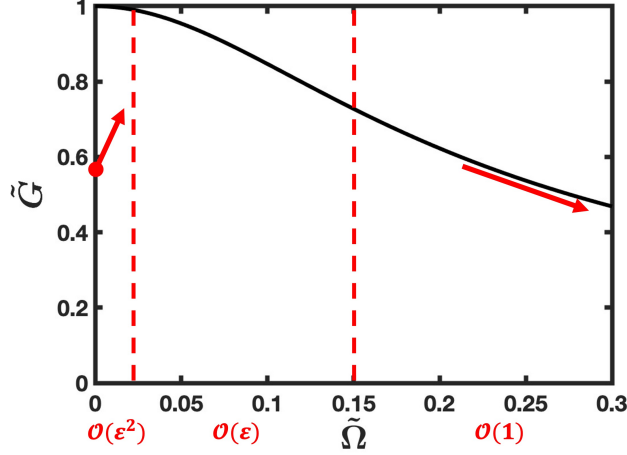
44

FIGURE 3.4. Schematic of approach to show that the M-current induces band-pass filter behavior with a resonance frequency at $\tilde{\Omega} \sim \epsilon$ using asymptotic approximation of gain of GIF model (in red) as function of input frequency. Gain is increased at $\tilde{\Omega} = \mathcal{O}(\epsilon^2)$ from constant input. Gain is decreasing at $\tilde{\Omega} = \mathcal{O}(1)$. Thus, resonance peak occurs at $\tilde{\Omega} = \mathcal{O}(\epsilon)$.

To exploit the time-scales of the membrane τ, the M-current τ_M, and the input current $1/\tilde{\Omega}$ we consider the frequencies of the input that lead to the dynamics of the model occuring at different time scales. The first regime we consider is when the frequency of the oscillations of the input current is much faster than the time-scale of the M-current, i.e. $1/\tilde{\Omega} << \tau_M$. We consider the time-scales of the input and the membrane to find the solutions for the membrane potential $\tilde{v}$ and utilize averaging to find the solutions for the M-current activation M. The second regime we consider is when the frequency of the oscillations of the input current is much slower than the time-scales of both the M-current and the membrane, i.e. $1/\tilde{\Omega} >> \tau_M, \tau$. This allows for the assumption that the membrane potential $\tilde{v}$ and the M-current activation M are at steady-state to find their solutions. In both instances, we utilize perturbation theory to expand the solutions in a small dimensionless parameter ($\epsilon = \tau/\tau_M$) and approximate the gain as a function of the input frequency. [**32**]. We remark that an asymptotic approximation of the gain for the input frequencies where the maximum gain $\tilde{G}$ occurs ($\tilde{\Omega} \sim \epsilon$) is quite complex and left for future work.

3.3.1. Asymptotic Approximation for Gain of GIF Model Neuron with High Frequency Oscillatory Input: Multiple Scales. We consider a regime in which the oscillations of the synaptic input current are much faster than the M-current, that is $\frac{1}{\tilde{\Omega}} <<$ τ_M. Therefore, we utilize multiple scale expansion [**32**], or "two-timing," which involves separating the fast $\tilde{I}_{\text{inp}}$- and v-dynamics and slow M-dynamics into two different temporal variables, expanding our solutions in the small dimensionless parameter $\epsilon = \tau/\tau_M$, and simultaneously solving on both time scales. Note that $\tilde{\Omega} = \mathcal{O}(1)$.

We set a fast time-scale $t_1 = \tilde{t}$, and a slow time-scale $t_2 = \epsilon\tilde{t}$, where $\tilde{v} = \tilde{v}(t_1, t_2)$ and $M = M(t_1, t_2)$. The implementation of two time scales results in a time derivative of $\frac{d}{d\tilde{t}} = \frac{\partial}{\partial t_1} + \epsilon\frac{\partial}{\partial t_2}$, and when substituted into the model equation (3.2) results in a system of PDEs

$$\frac{\partial \tilde{v}}{\partial t_1} + \epsilon\frac{\partial \tilde{v}}{\partial t_2} = -\tilde{v} - \tilde{g}_M M(\tilde{v} - \tilde{E}_K) + \tilde{A}_0(1 + \sin(2\pi\tilde{\Omega}t_1))$$

(3.4)

$$\frac{\partial M}{\partial t_1} + \epsilon\frac{\partial M}{\partial t_2} = \tilde{M}_\infty(\tilde{v}) - M$$

To oobtaini a 1st order approximate solution to this PDE, we expand $\tilde{v}$ and M in powers of ϵ, i.e. $\tilde{v} = \tilde{v}_0 + \epsilon\tilde{v}_1 + \cdots$, and $M = M_0 + \epsilon M_1 + \cdots$, and expand the steady-state activation function as $\tilde{M}_\infty(\tilde{v}) = \tilde{M}_\infty(\tilde{v}_0 + \epsilon\tilde{v}_1 + \cdots) \approx \tilde{M}_\infty(\tilde{v}_0) + \epsilon\tilde{M}'_\infty(\tilde{v}_0)\tilde{v}_1 + \cdots$. Substituting these expansions into system (3.4), the leading order system in ϵ (i.e. $\mathcal{O}(1)$) is

$$\frac{\partial \tilde{v}_0}{\partial t_1} = -\tilde{v}_0 - \tilde{g}_M M_0(\tilde{v}_0 - \tilde{E}_K) + \tilde{A}_0(1 + \sin(2\pi\tilde{\Omega}t_1))$$

(3.5)

$$\frac{\partial M_0}{\partial t_1} = 0.$$

Thus, M_0 is independent of the fast time-scale t_1, i.e., $M_0(t_1, t_2) = M_0(t_2)$ and the solution for the leading order equation of $\tilde{v}_0$ is:

$$
\tilde{v}_0(t_1, t_2) = \frac{\tilde{A}_0}{\sqrt{(1 + \tilde{g}_M M_0(t_2))^2 + 4\pi^2 \tilde{\Omega}^2}} \sin\left(2\pi \tilde{\Omega} t_1 + \tan^{-1}\left(\frac{-2\pi \tilde{\Omega}}{1 + \tilde{g}_M M_0(t_2)}\right)\right)
$$

$$
\cdots + \frac{\tilde{A}_0 + \tilde{g}_M M_0(t_2)\tilde{E}_K}{1 + \tilde{g}_M M_0(t_2)}
$$

$$
= a(M_0) \sin(2\pi \tilde{\Omega} t_1 + \phi(M_0)) + b(M_0)
$$

with a transient exponential decay term omitted. To find $M_0(t_2)$, i.e., how the M-current behaves on the slow time scale, we consider the order ϵ system of system (3.4)

$$
\frac{\partial \tilde{v}_1}{\partial t_1} + \frac{\partial \tilde{v}_0}{\partial t_2} = -\tilde{v}_1 - \tilde{g}_M(M_0\tilde{v}_1 + \tilde{v}_0 M_1 - M_1)
$$

$$
\frac{\partial M_1}{\partial t_1} + \frac{\partial M_0}{\partial t_2} = \tilde{M}_\infty(\tilde{v}_0) - M_0.
$$

We define $X_n = [\tilde{v}_n \ \ M_n]^T$ for $n = 0, 1, ...$, and rewrite the system into the form

(3.6) $$ L\vec{X}_1 = \frac{\partial}{\partial t_1}\vec{X}_1 + A\vec{X}_1 = F(\vec{X}_0), $$

where

$$
A = \begin{bmatrix} 1 + \tilde{g}_M M_0 & \tilde{g}_M(\tilde{v}_0 - \tilde{E}_K) \\ 0 & 0 \end{bmatrix}, \qquad F(\vec{X}_0) = \begin{bmatrix} -\frac{\partial \tilde{v}_0}{\partial t_2} \\ \tilde{M}_\infty(\tilde{v}_0) - M_0 - \frac{\partial M_0}{\partial t_2} \end{bmatrix}.
$$

Note that L is the linear differential operator $D_{t_1} + A$. The adjoint of L is given by $L^* = -D_{t_1} + A^T$. For a solution $\vec{X}_1$ to exist, $F(\vec{X}_0)$ must be orthogonal to the nullspace of the adjoint L^*, that is, for every $\tilde{\Omega}^{-1}$-periodic C^1 function f in the nullspace of L^*, the inner product of f with $F(\vec{X}_0)$ must be equal to 0 (with respect to the standard L^2 inner-product

for periodic functions), and therefore

$$\frac{df_1}{dt_1} = (1 + \tilde{g}_M M_0)f_1$$

$$\frac{df_2}{dt_1} = \tilde{g}_M(\tilde{v}_0 - \tilde{E}_K)f_1$$

From the first equation (note that $\tilde{g}_M M_0 \geq 0$), it is clear that the only $\tilde{\Omega}^{-1}$–periodic solution for f_1 is $f_1 = 0$, and thus f_2 is constant in t_1. Therefore ,the inner-product $\langle f, F(\vec{X}_0) \rangle = 0$ reduces to

$$\frac{1}{\tilde{\Omega}^{-1}} \int_0^{\tilde{\Omega}^{-1}} \left(\tilde{M}_\infty(\hat{v}_0(t_1, M_0)) - M_0 - \frac{\partial M_0}{\partial t_2} \right) dt_1 = 0$$

where we write $\hat{v}_0(t_1, M_0) = \tilde{v}_0(t_1, t_2)$ for convenience. Noting that M_0 is independent of t_1, we rewrite this equation into the form

$$\frac{\partial M_0}{\partial t_2} = \langle \tilde{M}_\infty(\hat{v}_0) \rangle_\infty - M_0$$

provides a differential equation for M_0 where

$$\langle \tilde{M}_\infty(\hat{v}_0) \rangle_\infty = \frac{1}{\tilde{\Omega}^{-1}} \int_0^{\tilde{\Omega}^{-1}} \tilde{M}_\infty(\hat{v}_0(t_1, M_0) dt_1.$$

We are interested in the "long-term" behavior of M_0 on the slow time-scale, so we set $\frac{\partial M_0}{\partial t_2} = 0$ and the resulting equation for M_0 is

$$M_0 = \langle \tilde{M}_\infty(\hat{v}_0) \rangle_\infty,$$

where $\langle \tilde{M}_\infty(\hat{v}_0) \rangle_\infty$ is the average value of the steady-state activation function $\tilde{M}_\infty$ over one period of $\hat{v}_0(t_1, M_0)$. Therefore, the first-order approximation to the "long-term" solution of system (3.5) (the leading order system in ϵ) is given by a system of coupled equations

$$\tilde{v}_0(\tilde{t}) = \frac{\tilde{A}_0}{\sqrt{(1 + \tilde{g}_M M_0)^2 + 4\pi^2 \tilde{\Omega}^2}} \sin\left(2\pi\tilde{\Omega}\tilde{t} + \tan^{-1}\left(\frac{-2\pi\tilde{\Omega}}{1 + \tilde{g}_M M_0} \right) \right) + \frac{\tilde{A}_0 + \tilde{g}_M M_0 \tilde{E}_K}{1 + \tilde{g}_M M_0},$$

with M_0 given by the solution of

$$M_0 - \langle \tilde{M}_\infty(\hat{v}_0) \rangle_\infty = 0.$$

where $\hat{v}_0(t_1, M_0) = \tilde{v}_0(t_1, t_2) = \tilde{v}_0(\tilde{t})$.

The above analysis implies that the gain of the GIF model neuron for sufficiently low frequency input current ($\tilde{\Omega}^{-1} << \tau_M$) is

$$\tilde{G} = \frac{1}{\sqrt{(1 + \tilde{g}_M M_0)^2 + 4\pi^2 \tilde{\Omega}^2}},$$

where M_0 is the solution to the equation

$$M_0 = \langle \tilde{M}_\infty(\hat{v}_0) \rangle_\infty = \tilde{\Omega} \int_0^{\tilde{\Omega}^{-1}} \tilde{M}_\infty(\hat{v}_0(t_1, M_0)) dt_1$$

where $\hat{v}_0(t_1, M_0) = \tilde{v}_0(t_1, t_2) = \tilde{v}_0(\tilde{t})$, i.e. the value of M_0 is the average level of M-current activation over one period. Note that the gain with no M-current ($\tilde{g}_M = 0$) is equal to the gain of the LIF neuron computed in section 3.2. Furthermore, the gain can be bounded from above and below

$$\frac{1}{\sqrt{(1 + \tilde{g}_M)^2 + 4\pi^2 \tilde{\Omega}^2}} \leq \tilde{G} \leq \frac{1}{\sqrt{1 + 4\pi^2 \tilde{\Omega}^2}},$$

i.e., the gain of the GIF model neuron is bounded from above by the gain of the LIF model neuron.

Figure 3.5 plots the gain $\tilde{G}$ of the GIF model neuron for various values of $\tilde{g}_M$ obtained from numerical simulations of the system 3.2 from section 3.1, and the asymptotic approximation of the gain computed by numerically solving for $\tilde{v}_0$ and M_0 from the equations above. For input frequencies above the cutoff frequency $\tilde{\Omega}_c \approx 0.01592$ of the LIF neuron, the M-current does not have a substantial effect on the gain of model GIF neuron and the gain resembles that of the LIF neuron.
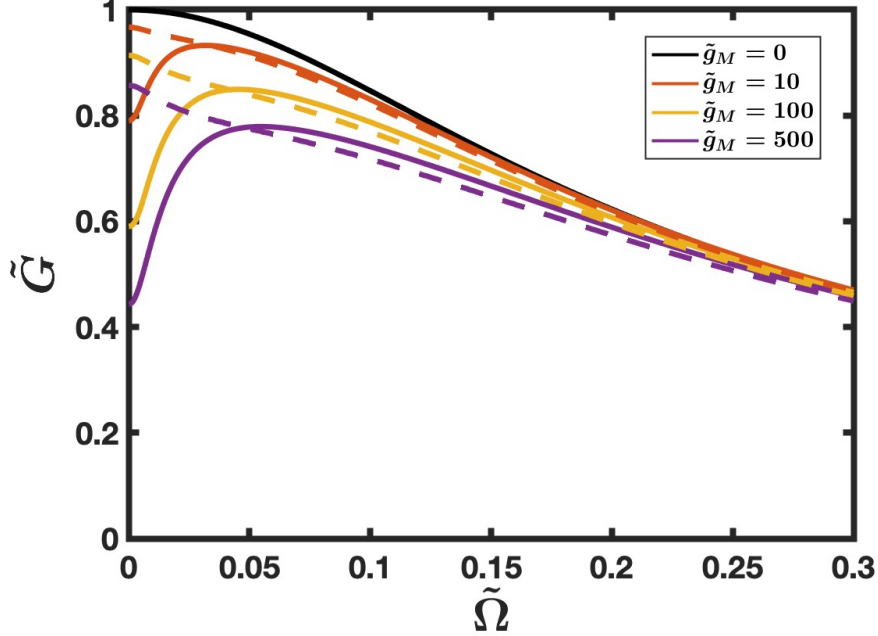
FIGURE 3.5. Amplitude gain $\tilde{G} = \tilde{A}/\tilde{A}_0$ of the solution of a single cell-based nondimensional neuronal GIF model given by equation 3.2 with different maximal M-current conductance valuees $\tilde{g}_M$ as a function of the frequency $\tilde{\Omega}$ of the periodic input with amplitude $\tilde{A}_0$. Solid curves reflect data computed from solutions of the model, dotted curves indicate corresponding approximations. The approximation of the gain is good above the cutoff frequency $\tilde{\Omega}_c \approx 0.01592$. The nondimensionalization of the input frequency is given by $\tilde{\Omega} = \omega \frac{C}{g_L} \approx 7.727\omega$ where ω has the units kHz.

3.3.2. Asymptotic Approximation for Gain of GIF Model Neuron with Low Frequency Oscillatory Input. Now we consider the case in which the period of the oscillatory input is much larger than the time constants of both the M-current and the voltage dynamics. Specifically, we will assume that $\tilde{\Omega} = \mathcal{O}(\epsilon^2)$ and write $\tilde{\Omega} = \epsilon^2 \tilde{\Omega}_0$, where $\tilde{\Omega}_0 = \mathcal{O}(1)$. We show that the amplitude of the voltage $\tilde{v}$ increases above the amplitude of the leading order term, i.e., the limit of the amplitude as $\tilde{\Omega}_0 \to 0^+$. For this analysis, we will assume a general M-current activation function $\tilde{m}_\infty$ that is strictly monotonic, i.e., $\tilde{M}'_\infty(\tilde{v}) > 0$, and satisfies $0 \leq \tilde{M}_\infty(\tilde{v}) \leq 1$.

Rescaling time from the nondimensional GIF model (3.2) so that $s = \epsilon^2 \tilde{t}$ gives

(3.7)
$$\epsilon^2 \frac{d\tilde{v}}{ds} = -\tilde{v} - \tilde{g}_M M(\tilde{v} - \tilde{E}_K) + \tilde{A}_0(1 + \sin(2\pi\tilde{\Omega}_0 s)),$$
$$\epsilon \frac{dM}{ds} = \tilde{M}_\infty(\tilde{v}) - M$$

We expand $\tilde{v}(s) = \tilde{v}_0 + \epsilon\tilde{v}_1 + \cdots$, $M(s) = M_0 + \epsilon M_1 + \cdots$ i ϵ, and $\tilde{M}_\infty(\tilde{v}) = \tilde{M}_\infty(\tilde{v}_0 + \epsilon\tilde{v}_1 + \cdots) \approx \tilde{M}_\infty(\tilde{v}_0) + \epsilon\tilde{M}'_\infty(\tilde{v}_0)\tilde{v}_1$. The resulting leading order $(\mathcal{O}(1))$ system is the set of algebraic equations

(3.8)
$$0 = -\tilde{v}_0 - \tilde{g}_M M_0(\tilde{v}_0 - \tilde{E}_K) + \tilde{A}_0(1 + \sin(2\pi\tilde{\Omega}_0 s))$$
$$0 = \tilde{M}_\infty(\tilde{v}_0) - M_0$$

which implies that $\tilde{v}_0$ track the input, and $M_0 = \tilde{M}_\infty(\tilde{v}_0)$, i.e.,

(3.9)
$$\tilde{v}_0 + \tilde{g}_M \tilde{M}_\infty(\tilde{v}_0)(\tilde{v}_0 - \tilde{E}_K) = \tilde{A}_0(1 + \sin(2\pi\tilde{\Omega}_0 s)).$$

For general $\tilde{M}_\infty$, this equation cannot be solved explicitly for $\tilde{v}_0(s)$. (An explicit example is shown in the appendix where a piece-wise linear description of $\tilde{M}_\infty$ is implemented.) Howeever, we will show that, for monotonically increasing $\tilde{M}_\infty$, the amplitude of oscillations for $\tilde{v}(s)$ increases with frequency $\tilde{\Omega}$.

The $\mathcal{O}(\epsilon)$ equations of system (3.7) are

(3.10)
$$0 = -\tilde{v}_1 - \tilde{g}_M(M_0\tilde{v}_1 + M_1(\tilde{v}_0 - \tilde{E}_K))$$
$$\frac{dM_0}{ds} = \tilde{M}'_\infty(\tilde{v}_0)\tilde{v}_1 - M_1.$$

Note that $\frac{dM_0}{ds} = \tilde{M}'_\infty(\tilde{v}_0)\frac{d\tilde{v}_0}{ds}$. Implicit differention of equation (3.9) yields the derivative of $\tilde{v}_0$

$$\frac{d\tilde{v}_0}{ds} = \frac{2\pi\tilde{\Omega}_0\tilde{A}_0\cos(2\pi\tilde{\Omega}_0 s)}{1 + \tilde{g}_M\tilde{M}_\infty(\tilde{v}_0) + \tilde{g}_M\tilde{M}'_\infty(\tilde{v}_0)(\tilde{v}_0 - \tilde{E}_K)},$$

thus the order ϵ solution is

$$(3.11) \qquad \tilde{v}_1(s) = \tilde{\Omega}_0 2\pi \tilde{A}_0 \tilde{g}_M \frac{\tilde{M}'_\infty(\tilde{v}_0)(\tilde{v}_0 - \tilde{E}_K)\cos(2\pi\tilde{\Omega}_0 s)}{(1 + \tilde{g}_M \tilde{M}_\infty(\tilde{v}_0) + \tilde{g}_M \tilde{M}'_\infty(\tilde{v}_0)(\tilde{v}_0 - \tilde{E}_K))^2}.$$

We rewrite the order ϵ solution as $\tilde{v}_1(s) = \tilde{\Omega}_0 \hat{v}_1(s)$ where

$$\hat{v}_1(s) = 2\pi \tilde{A}_0 \tilde{g}_M \frac{\tilde{M}'_\infty(\tilde{v}_0)(\tilde{v}_0 - \tilde{E}_K)\cos(2\pi\tilde{\Omega}_0 s)}{(1 + \tilde{g}_M \tilde{M}_\infty(\tilde{v}_0) + \tilde{g}_M \tilde{M}'_\infty(\tilde{v}_0)(\tilde{v}_0 - \tilde{E}_K))^2}.$$

Thus, to second-order approximation,

$$\tilde{v}(s) = \tilde{v}_0(s) + \epsilon \tilde{\Omega}_0 \hat{v}_1(s).$$

We now show that the amplitude of the second-order approximation to the solution $\tilde{v}$ is larger than the amplitude of the first-order approximation to the solution $\tilde{v}_0$. Note that $\frac{d\tilde{v}_0}{ds} = 0$ at $s = \frac{1}{4\tilde{\Omega}_0}$ and $\frac{3}{4\tilde{\Omega}_0}$, and the second derivative of the first-order approximation at these points are

$$\frac{d^2\tilde{v}_0}{ds^2}\left(\frac{1}{4\tilde{\Omega}_0}\right) = \frac{-4\pi^2\tilde{\Omega}_0^2\tilde{A}_0}{1 + \tilde{g}_M \tilde{M}_\infty\left(\tilde{v}_0\left(\frac{1}{4\tilde{\Omega}_0}\right)\right) + \tilde{g}_M \tilde{M}'_\infty\left(\tilde{v}_0\left(\frac{1}{4\tilde{\Omega}_0}\right)\right)\left(\tilde{v}_0\left(\frac{1}{4\tilde{\Omega}_0}\right) - \tilde{E}_K\right)} < 0,$$

$$\frac{d^2\tilde{v}_0}{ds^2}\left(\frac{3}{4\tilde{\Omega}_0}\right) = \frac{4\pi^2\tilde{\Omega}_0^2\tilde{A}_0}{1 + \tilde{g}_M \tilde{M}_\infty\left(\tilde{v}_0\left(\frac{3}{4\tilde{\Omega}_0}\right)\right) + \tilde{g}_M \tilde{M}'_\infty\left(\tilde{v}_0\left(\frac{3}{4\tilde{\Omega}_0}\right)\right)\left(\tilde{v}_0\left(\frac{3}{4\tilde{\Omega}_0}\right) - \tilde{E}_K\right)} > 0.$$

This implies that the maximum $\tilde{v}_0^{\max}$ and minimum $\tilde{v}_0^{\min}$ values of $\tilde{v}_0(s)$ occur at $s_0^{\max} = 1/(4\tilde{\Omega}_0)$ and $s_0^{\min} = 3/(4\tilde{\Omega}_0)$, respectively. Furthermore, note that the first derivatives of $\hat{v}_1$ at $s_0^{\max}$ and $s_0^{\min}$ are

$$\frac{d\hat{v}_1}{ds}(s_0^{\max}) = -4\pi^2\tilde{\Omega}_0\tilde{A}_0\tilde{g}_M \frac{\tilde{M}'_\infty(\tilde{v}_0^{\max})(\tilde{v}_0^{\max} - \tilde{E}_K)}{(1 + \tilde{g}_M \tilde{M}_\infty(\tilde{v}_0^{\max}) + \tilde{M}'_\infty(\tilde{v}_0^{\max})(\tilde{v}_0^{\max} - \tilde{E}_K))^2} < 0$$

$$\frac{d\hat{v}_1}{ds}(s_0^{\min}) = 4\pi^2\tilde{\Omega}_0\tilde{A}_0\tilde{g}_M \frac{\tilde{M}'_\infty(\tilde{v}_0^{\min})(\tilde{v}_0^{\min} - \tilde{E}_K)}{(1 + \tilde{g}_M \tilde{M}_\infty(\tilde{v}_0^{\min}) + \tilde{M}'_\infty(\tilde{v}_0^{\min})(\tilde{v}_0^{\min} - \tilde{E}_K))^2} > 0.$$

Because $\hat{v}_1(s_0^{\max}) = \hat{v}_1(s_0^{\min}) = 0$, the value of the second-order approximation is equal to the value of the first order approximation at $s_0^{\max}$ and $s_0^{\min}$, i.e.,

$$\tilde{v}(s_0^{\max}) = \tilde{v}_0(s_0^{\max}) + \epsilon\tilde{\Omega}_0\hat{v}_1(s_0^{\max}) = \tilde{v}_0(s_0^{\max})$$

and

$$\tilde{v}(s_0^{\min}) = \tilde{v}_0(s_0^{\mathrm{mni}}) + \epsilon\tilde{\Omega}_0\hat{v}_1(s_0^{\min}) = \tilde{v}_0(s_0^{\min}).$$

The derivative of the second-order approximation to the solution at at $s_0^{\max}$ and $s_0^{\min}$ is

$$\frac{d\tilde{v}}{ds}(s_0^{\max}) = \frac{d\tilde{v}_0}{ds}(s_0^{\max}) + \epsilon\tilde{\Omega}_0\frac{d\hat{v}_1}{ds}(s_0^{\max}) = \epsilon\tilde{\Omega}_0\frac{d\hat{v}_1}{ds}(s_0^{\max}) < 0$$

and

$$\frac{d\tilde{v}}{ds}(s_0^{\min}) = \frac{d\tilde{v}_0}{ds}(s_0^{\min}) + \epsilon\tilde{\Omega}_0\frac{d\hat{v}_1}{ds}(s_0^{\min}) = \epsilon\tilde{\Omega}_0\frac{d\hat{v}_1}{ds}(s_0^{\min}) > 0.$$

This implies that there exists some $s^{\max} < s_0^{\max}$ and $s^{\min} < s_0^{\min}$ such that $\tilde{v}(s^{\max}) > \tilde{v}_0(s_0^{\max})$ and $\tilde{v}(s^{\min}) < \tilde{v}_0(s_0^{\min})$.
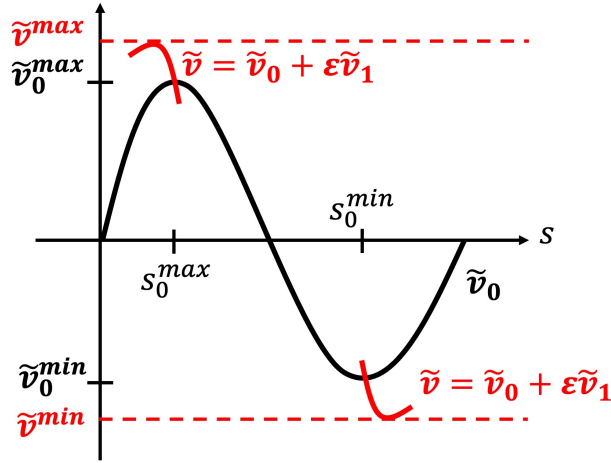

FIGURE 3.6. Schematic showing how the maximum value of how, to second order approximation, the amplitude of $\tilde{v}(s)$ is larger than the amplitude of $\tilde{v}_0(s)$.

We expand $s^{\mathrm{max}} = s_0^{\mathrm{max}} - \epsilon s_1^{\mathrm{max}} + \cdots$ and $s^{\mathrm{min}} = s_0^{\mathrm{min}} + \epsilon s_1^{\mathrm{min}} + \cdots$ in ϵ where $s_1^{\mathrm{max}}, s_1^{\mathrm{min}} > 0$ and $s_1^{\mathrm{max}}, s_1^{\mathrm{min}} = \mathcal{O}(1)$. Then expanding $\tilde{v}(s^{\mathrm{max}})$ and $\tilde{v}(s^{\mathrm{min}})$,

$$\tilde{v}(s^{\mathrm{max}}) = \tilde{v}(s_0^{\mathrm{max}} - \epsilon s_1^{\mathrm{max}}) = \tilde{v}(s_0^{\mathrm{max}}) - \epsilon s_1^{\mathrm{max}} \frac{d\tilde{v}}{ds}(s_0^{\mathrm{max}}) = \tilde{v}_0(s_0^{\mathrm{max}}) - \epsilon^2 \tilde{\Omega}_0 s_1^{\mathrm{max}} \frac{d\hat{v}_1}{ds}(s_0^{\mathrm{max}}),$$

$$\tilde{v}(s^{\mathrm{min}}) = \tilde{v}(s_0^{\mathrm{min}} + \epsilon s_1^{\mathrm{min}}) = \tilde{v}(s_0^{\mathrm{min}}) + \epsilon s_1^{\mathrm{min}} \frac{d\tilde{v}}{ds}(s_0^{\mathrm{min}}) = \tilde{v}_0(s_0^{\mathrm{min}}) + \epsilon^2 \tilde{\Omega}_0 s_1^{\mathrm{min}} \frac{d\hat{v}_1}{ds}(s_0^{\mathrm{min}}).$$

The amplitude of the system to second order is

$$
\begin{aligned}
\tilde{A} &= \frac{\tilde{v}(s^{\mathrm{max}}) - \tilde{v}(s^{\mathrm{min}})}{2} \\
&= \frac{\tilde{v}_0(s_0^{\mathrm{max}}) - \tilde{v}_0(s_0^{\mathrm{min}})}{2} + \epsilon^2 \tilde{\Omega}_0 \frac{-s_1^{\mathrm{max}} \frac{d\hat{v}_1}{ds}(s_0^{\mathrm{max}}) + s_1^{\mathrm{min}} \frac{d\hat{v}_1}{ds}(s_0^{\mathrm{min}})}{2}.
\end{aligned}
$$

Note that $\frac{-s_1^{\mathrm{max}} \frac{d\hat{v}_1}{ds}(s_0^{\mathrm{max}}) + s_1^{\mathrm{min}} \frac{d\hat{v}_1}{ds}(s_0^{\mathrm{min}})}{2} > 0$ and is $\mathcal{O}(1)$. Hence we write the amplitude of the system to second order as

$$\tilde{A} = \frac{\tilde{v}_0(s_0^{\mathrm{max}}) - \tilde{v}_0(s_0^{\mathrm{min}})}{2} + \tilde{\Omega} F(s_1^{\mathrm{max}}, s_1^{\mathrm{min}}, v_0^{\mathrm{max}}, v_0^{\mathrm{min}}, \tilde{g}_M)$$

where $F > 0$ and $F = \mathcal{O}(1)$. Therefore the amplitude $\tilde{A}$ (and thus the gain $\tilde{G}$) of system (3.7) grows with input frequency $\tilde{\Omega}$ for $\tilde{\Omega} = \mathcal{O}(\epsilon^2)$. As shown in section 3.3.1, the gain decreases for $\tilde{\Omega} = \mathcal{O}(1)$, and therefore the GIF model neuron acts as a band-pass filter with a resonance frequency that must be at $\mathcal{O}(\epsilon)$ - this matches the simulation results in section 3.1. However, this provokes the question: what is/are the mechanisms responsible for the M-current endowing the model GIF neuron with band-pass filter and resonance properties? In the following sections we identify and explore mechanisms of the model neuron and the M-current that can provide insight into this question- specifically, analysis of $\tilde{M}_\infty(\tilde{v})$ can provide insight into how the gain of the model GIF neuron in response to oscillatory input depends on the M-current.

3.4. Natural Frequencies of GIF Model Neuron Do Not Induce Resonant Behavior

In the previous section, we showed that the GIF neuron with M-current acts as a band-pass filter with a resonance peak/frequency. Usually, the mechanism responsible for resonant behavior is forcing of the system at a "natural" frequency that is intrinsic to the model. To investigate if a natural frequency is interacting with the oscillatory input to the GIF model, we examine the eigenvalues of the GIF neuron. If the eigenvalues are complex, then the natural frequency of the system is given by the imaginary part of the eigenvalues. If this natural frequency occurs around the resonce frequency $\tilde{\Omega} \sim 0.05$, the resonant behavior in the system is due to the interaction of the frequency of the oscillatory input with the natural frequency of the GIF neuron.

We examine the steady-state of the GIF neuronal model with constant input $\tilde{A}_0$ because of the form of the input. It was chosen to be always positive with an average value of $\tilde{A}_0$ - this defines the point at which the GIF model neuron oscillates around. This steady-state is

(3.12)
$$\tilde{v}^* = \frac{\tilde{A}_0 + \tilde{g}_M M^* \tilde{E}_K}{1 + \tilde{g}_M M^*}$$

$$M^* = \tilde{M}_\infty \left(\frac{\tilde{A}_0 + \tilde{g}_M M^* \tilde{E}_K}{1 + \tilde{g}_M M^*} \right)$$

Because $\tilde{E}_K = -1$, $-1 < \tilde{v}^* \leq \tilde{A}_0$, and $0 \leq M^* \leq 1$ follows from the range of the steady-state activation function $\tilde{M}_\infty$. The Jacobian of the GIF neuronal model evaluated at the steady-state $(\tilde{v}^*, M^*)$ is

$$J(\tilde{v}^*, M^*) = \begin{bmatrix} -(1 + \tilde{g}_M M^*) & -\tilde{g}_M (\tilde{v}^* - \tilde{E}_K) \\ \epsilon \tilde{M}'_\infty(\tilde{v}^*) & -\epsilon \end{bmatrix},$$

and the eigenvalues of $J(\tilde{v}^*, M^*)$ are

$$\lambda = -\kappa \pm \sqrt{\Delta},$$

where

$$\kappa = \frac{\epsilon + 1 + \tilde{g}_M M^*}{2} > 0, \quad \eta = 1 + \tilde{g}_M M^* + \tilde{g}_M \tilde{M}'_\infty(\tilde{v}^*)(\tilde{v}^* - \tilde{E}_K) > 0,$$

and

$$\Delta = \kappa^2 - \epsilon\eta.$$

$\text{Re}(\lambda) = -\kappa < 0$ implies that the steady-state is always stable. If $\Delta < 0$, the eigenvalues are complex, so the equilibrium is a stable spiral with natural frequency $f = \sqrt{-\Delta}/2\pi$. If $\Delta > 0$, the eigenvalues are real, so the equilibrium is a stable node.

Figure 3.7 plots the $\Delta = 0$ curve in $(\epsilon, \tilde{g}_M)$ parameter space, separating the space into two regions: one region in which the steady-state is a stable node and another region where it is a stable spiral. Note that in the GIF model $\epsilon = \tau/\tau_M \approx 0.047$, which is located in the stable node region of the space, i.e., an order of magnitude in ϵ below the boundary. Therefore, local stability analysis indicates that there is no natural frequency in the model that could interact with oscillatory input to induce resonance in the system, and the usual mechanism for resonance is not responsible for inducing the band-pass filtering and resonance properties in the GIF model with M-current.
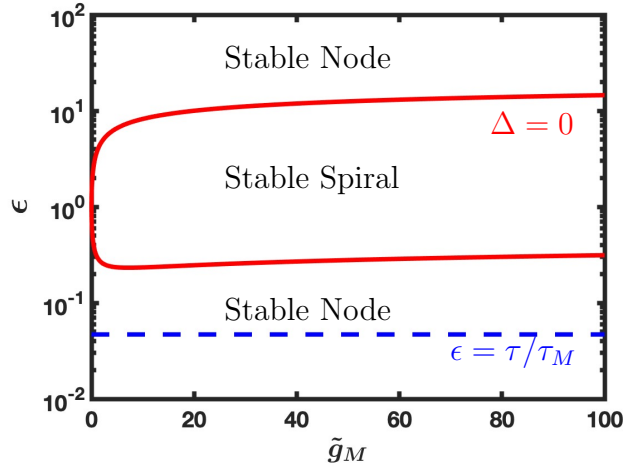
FIGURE 3.7. $(\epsilon, \tilde{g}_M)$ parameter space separated into regions corresponding to the stability of the equilibrium point $(\tilde{v}^*, M^*)$ of the GIF model with constant input $\tilde{A}_0$. The $\Delta = 0$ curve indicates where the equilibrium changes stability between stable spirals and stable nodes. The blue dashed line indicates the parameter value $\epsilon = \tau/\tau_M \approx 0.047$ used in the GIF model. Note that ϵ is on a log scale.

3.5. Subthreshold Activation of M-Current Modulates Resonant Behavior of Model GIF Neuron

Our analysis of the equilibrium points of the GIF model neuron reveals no natural frequencies in the model that could interact with oscillatory input to induce resonant behavior and therefore the standard mechanism for resonance dooes not underlie the band-pass filter and resonance properties of the GIF model. In this section, we show that the magnitude and subthreshold activation of the M-current modulates the maximal response of the neuron, where the maxmimal response occurs in the frequency domain, and how large the "band" of the band-pass filter is in the frequency domain.

In what follows, we define the normalized gain G to be the gain $\tilde{G} = \tilde{A}/\tilde{A}_0$ at an arbitrary input frequency $\tilde{\Omega}$ normalized by the limit of the gain for arbitary low input frequency ($\tilde{\Omega} \to 0^+$). We also define G_{max} to be the maximum normalized gain that occurs at the resonance frequency $\tilde{\Omega}_{\text{res}}$ and resonance length $\tilde{\Omega}_{\text{len}}$ as the range of frequencies that have a normalized gain greater than 1. Normalized gain curves for various magnitudes of M-current ($\tilde{g}_M$) are shown in Figure 3.8a. Figure 3.8b plots the maximal normalized gain G_{max}, figure 3.8c resonance frequency $\tilde{\Omega}_{\text{res}}$, and figure 3.8d resonance length $\tilde{\Omega}_{\text{len}}$ all as functions of $\tilde{g}_M$. The colored dots in figures 3.8b-3.8d correspond to the colored normalized gain curves in figure 3.8a. The black curve in figure 3.8a corresponds to the model neurons response with no M-current (as discussed in section 3.2).
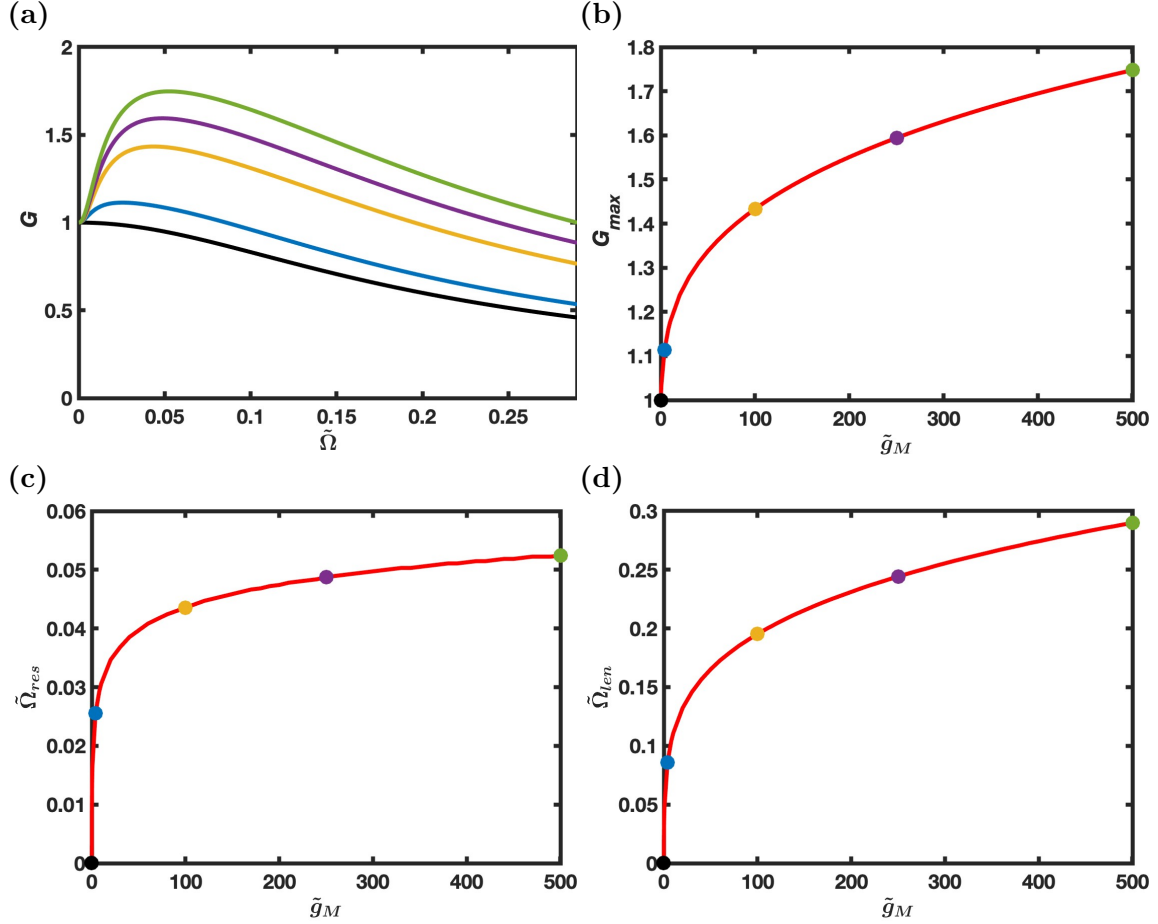
FIGURE 3.8. Resonance induced by the M-current in GIF model neuron. (a) Normalized gain G as a function of $\tilde{\Omega}$ for $\tilde{g}_M = 0,\ 4,\ 100,\ 250,\ 500$ as black, blue, yellow, purple, and green curves, respectively. Corresponding values of peak resonance, resonant frequency, and resonance lengths represented in figures 3.8b-3.8d in corresponding color dots. (b) Peak resonance. (c) Resonant frequency. (d) Resonance length.

As the magnitude of the M-current $\tilde{g}_M$ increases, the maximum gain G_{max}, resonance frequency $\tilde{\Omega}_{\mathrm{res}}$, and resonance length $\tilde{\Omega}_{\mathrm{len}}$ all increase monotonically with $\tilde{g}_M$. Most of the resonance frequencies occur around $\tilde{\Omega}_{\mathrm{res}} \sim 0.03 - 0.05$, correlated with the frequency associated with the M-current, i.e., $1000/\tau_M \sim 6$ Hz. The increase in normalized maximum gain G_{max} and resonance length $\tilde{\Omega}_{\mathrm{res}}$ occurs because the gain $\tilde{G}$ at $\tilde{\Omega} = 0$ decreases as the magnitude of the M-current is increased (shown in figure 3.2). This is due to the fact that

the M-current does not have a substantial effect on the gain of the GIF model to input at sufficiently high frequences (section 3.3.1).

To elucidate the mechanisms that control resonance of the GIF model neurons, we examine how properties of the M-current activation function $\tilde{M}_\infty(\tilde{v})$ affect the normalized gain G, recall that

$$\tilde{M}_\infty(\tilde{v}) = \frac{1}{1 + \exp(-\frac{\tilde{v} - \tilde{v}_H}{\tilde{s}})}$$

where $\tilde{v}_H = (v_H - E_L)/(E_L - E_K)$ determines the half-maximum of the curve, i.e., it sets the activation threshold of the M-current, and $\tilde{s} = s/(E_L - E_K)$ determines the steepness of the activation curve. To test how the steepness $\tilde{s}$ and half-maximum $\tilde{v}_H$ parameters modulate the resonance properties of the GIF model neuron, the steepness $\tilde{s}$ and half-maximum $\tilde{v}_H = \tilde{v}_T + \tilde{s} \log(1/\tilde{M}_\infty^{\max} - 1)$ are simultaneously increased so that (a) the steady-state activation at the firing threshold $\tilde{M}_\infty(\tilde{v}_T)$ of the GIF neuron is fixed at $\tilde{M}_\infty^{\max} = 0.05134$ (the value at the firing threshold with unperturbed parameters $\tilde{s}$ and $\tilde{v}_H$), and (2) the level of activation of the M-current at subthreshold membrane potentials varies from only active immediately below $\tilde{v}_T$ to active for all subthreshold potentials, as shown in Figure 3.9. That is, as $\tilde{s}$ and $\tilde{v}_H$ are increased together, the system limits to a case in which the M-current remains activated and therefore simply acts like a leakage current; and when $\tilde{s}$ and $\tilde{v}_H$ are decreased, the subthreshold activation of the M-current decreases, so that it is only non-zero close to threshold.
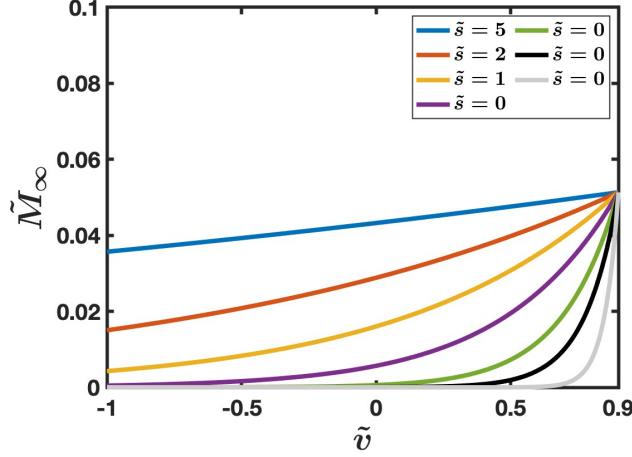
FIGURE 3.9. The steady-state activation curve $\tilde{M}_\infty(\tilde{v})$ for various values of slope parameter $\tilde{s}$ specified in the legend and the corresponding half-maximum parameter $\tilde{v}_H = \tilde{v}_T + \tilde{s}\log(1/\tilde{M}_\infty^{\max} - 1)$. The black curves indicate the default parameter values $s = 2.4$, $v_H = -45$. Variations in $\tilde{s}$ and $\tilde{v}_H$ induce a change in the subthreshold activation of the M-current while maintaining the maximum activation level $\tilde{M}(\tilde{v}_T) = \tilde{M}_\infty^{\max}$. Note the firing threshold of the model GIF neuron is $\tilde{v}_T = 0.9$.

Figure 3.10 plots a bar chart of the (normalized) peak resonance $G_{\max}$ of the model GIF neuron against the magnitude of subthreshold activation of the M-current, and the corresponding normalized gain curves below. Note that the color of the bar and normalized gain curve corresponds to the parameter values of the M-current activation curve in figure 3.9. The bar chart and corresponding normalized gain curves are plotted for various magnitudes of the M-current $\tilde{g}_M$. At lower magnitudes of the M-current $\tilde{g}_M$ the peak resonance values do not vary significantly as the subthreshold activation is changed.

As the magnitude of the M-current $\tilde{g}_M$ increases, the maximum value of the peak resonance bar plots becomes significantly greater than the surrounding values. This implies that (at sufficiently large magnitude of M-current $\tilde{g}_M$) the subthreshold activation level of the M-current modulates the resonant behavior of the model, and also provides a mechanism for maximizing the response of the model GIF neuron to oscillatory input.
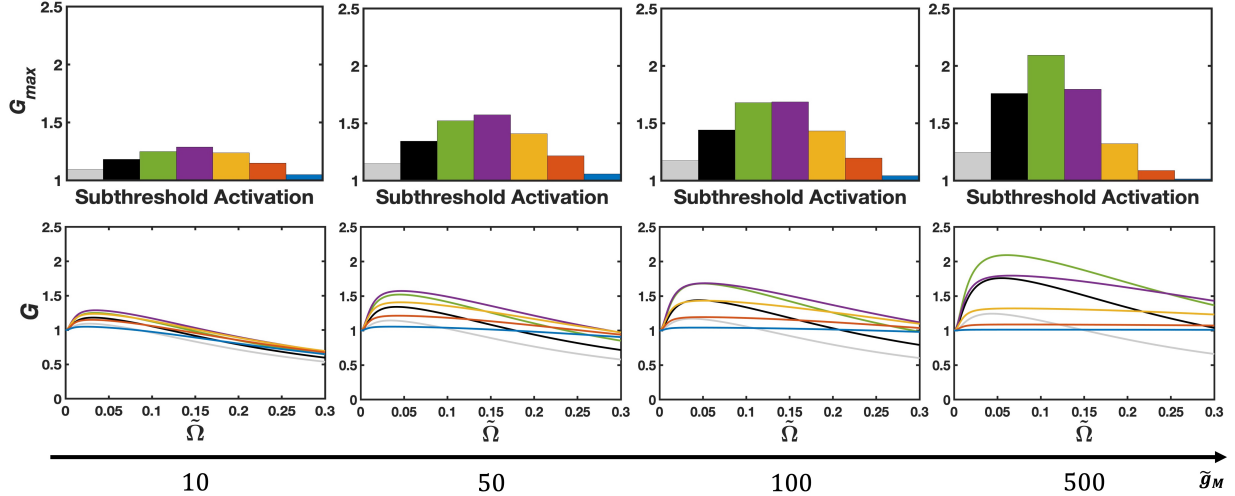
FIGURE 3.10. Effects of changing subthreshold activation level of M-current activation function on normalized gain of GIF neuron. Subthreshold activation correlates to colors in figure 3.9. The default subthreshold activation level corresponds to the black curves and bars. TOP: normalized peak resonance $G_{\max}$ of GIF model neuron against magnitude of subthreshold activtion various values of magnitude of M-current $\tilde{g}_M$. BOTTOM: Normalized gain curves G of GIF model neuron change with various subthreshold activation levels for various values of magnitude of M-current $\tilde{g}_M$. Colors of bars and normalized gain curves correspond to parameter values of M-current activation curves in figure 3.9.

3.6. Summary

In the previous chapter we observed how, together, the leakage current and the M-current counteract the slowly fluctuating synaptic currents due to the input but not faster fluctuations that occur. In this chapter we considered single cell model GIF neurons with only sub-threshold dynamics and showed that the leakage current induces low-pass filter behavior in the model neuron. We showed that the M-current endows the GIF model neuron with band-pass filter and resonance properties while not substationally altering the gain at very high frequencies. Furthermore, the resonance frequency occurs near the frqeuency associated wiith the M-current.

We studied the effects of changing the subthreshold activation of the M-current and showed that it regulates the resonance behavior of the model GIF neuron and our analysis

61

implies that if the subthreshold activation of the M-current is at a critical value, then the (normalized) peak resonance of the model GIF neuron is maximized.

The analysis in this chapter provides insight into the phenomenon in the previous chapter where the leakage current and M-current appeared to counteract the slow ($\approx$ 1Hz) oscillations but allow faster transient fluctuations in input current to induce an spike in the ICNS neurons. We showed that the normalized peak resonance as well as the resonancee frequency of the ICNS network model neurons from chapter 2 depend on the magnitude of the M-current g_M in individual cells. This implies that the ICNS model neurons respond preferentially to specific frequencies and the response of the cells in the network can be tuned by altering the strength of the M-current in the model.

3.7. Appendix

3.7.1. Asymptotic Approximation for Gain of GIF Model Neuron with Low Frequency Oscillatory Input: Piece-Wise Linear Approximation of Steady-State Activation Function $\tilde{M}_\infty$.

We approximate the steady-state function $\tilde{M}_\infty$ as a piece-wise linear function

$$\tilde{M}_\infty(\tilde{v}) \approx f(\tilde{v}) = \begin{cases} \tilde{a}(\tilde{v} - v_{\min}) & \text{if } \tilde{v} \geq v_{\min} \\ \\ 0 & \text{else} \end{cases}$$

where we assume $v_{\min} > 0$. We validate this assumption and discuss how the parameters of the piece-wise linear approximation are chosen to minimize the error below. We now show that the gain for sufficiently low frequency $\tilde{\Omega} = \epsilon^2 \tilde{\Omega}_0$ is larger than the limit of the amplitude gain as $\tilde{\Omega}_0 \to 0$.

The assumption of a piece-wise linear approximation of $\tilde{M}_\infty$ means that the solution $\tilde{v}$ will consist of two different solutions stitched together: one for $\tilde{v}_0 \geq v_{\min}$ and one for $\tilde{v}_0 < v_{\min}$. The M-current is not activated for $\tilde{v}_0 < v_{\min}$ (i.e. $M_0 = 0$) and the M-current and membrane potential are much faster than the input (the solution is enslaved to the input)

thus the solution for $\tilde{v}_0$ is

(3.13)
$$\tilde{v}_0(s) = \tilde{A}_0(1 + \sin(2\pi\tilde{\Omega}_0 s))$$

when $\tilde{A}_0(1 + \sin(2\pi\tilde{\Omega}_0 s)) < v_{\min}$. When the M-current is activated (i.e. $\tilde{v}_0 \geq v_{\min}$) we have $M_0 = \tilde{a}(\tilde{v}_0 - v_{\min})$ and the solution for $\tilde{v}_0$ is

(3.14)
$$\tilde{v}_0(s) = \alpha + \sqrt{\beta + \gamma \sin(2\pi\tilde{\Omega}_0 s)}$$

where

(3.15)
$$\alpha = \tilde{E}_K + v_{\min} - \frac{1}{\tilde{a}\tilde{g}_M}$$
$$\beta = \alpha^2 - \frac{4}{\tilde{a}\tilde{g}_M}(v_{\min}\tilde{E}_K - \tilde{A}_0)$$
$$\gamma = \frac{4}{\tilde{a}\tilde{g}_M}\tilde{A}_0$$

Note that $\beta - \gamma > 0$ so the solution $\tilde{v}_0(s)$ is always real.

We consider two cases: the first in which the M-current is activated over the entire period of the solution, and the second where the M-current becomes non-activated over some portion of the period of the solution. The case where the M-current is non-activated over the entire period reduces to the LIF analysis shown in section 3.2.

Suppose the M-current is activated over the entire period of the solution, i.e. $\tilde{v}_0(s) \geq v_{\min}$ for all $s \in [0, 1]$. The second-order approximation to the solution is given by

$$\tilde{v}(s) = \tilde{v}_0(s) + \epsilon\tilde{\Omega}_0\hat{v}_1(s)$$

with $\tilde{v}_0$ and $\tilde{v}_1 = \tilde{\Omega}_0\hat{v}_1$ are from 3.14 and 3.11. We note that the first order approximation $\tilde{v}_0$ has a minimum and a maximum at $s_{\min}^0 = 3/(4\tilde{\Omega}_0)$ and $s_{\max}^0 = 1/(4\tilde{\Omega}_0)$, respectively, where

$$\frac{d\tilde{v}_0}{ds}(s_{\max}^0) = \frac{d\tilde{v}_0}{ds}(s_{\min}^0) = 0.$$

Substituting the last equality into 3.11 implies

$$\tilde{v}_1(s^0_{\max}) = \tilde{v}_1(s^0_{\min}) = 0,$$

Hence $\hat{v}_1(s^0_{\max}) = \hat{v}_1(s^0_{\min}) = 0$. Following from the previous equality,

$$\tilde{v}(s^0_{\max}) = \tilde{v}_0(s^0_{\max}),$$

and Recall that $\tilde{v}_1 = \tilde{\Omega}_0 \hat{v}_1$. Thus it suffices to show that $\frac{d\tilde{v}_1}{ds}(s^0_{\max}) < 0$. We rewrite the order ϵ approximation as

$$\tilde{v}_1 = \frac{\tilde{M}'_\infty(\tilde{v}_0)(\tilde{v}_0 - \tilde{E}_K)}{\frac{1}{\tilde{g}_M} + \tilde{M}_\infty(\tilde{v}_0) + \tilde{M}'_\infty(\tilde{v}_0)(\tilde{v}_0 - \tilde{E}_K)}.$$

Assuming the use of the piece-wise linear approximation of $\tilde{M}_\infty$ and that $\tilde{v}_0 \geq v_{\min} > 0$ simplifies the expression for the order ϵ approximation to

$$\tilde{v}_1 = \frac{(\tilde{v}_0 - \tilde{E}_K)\frac{d\tilde{v}_o}{ds}}{\frac{1}{\tilde{a}\tilde{g}_M} + 2\tilde{v}_0 - v_{\min} - \tilde{E}_K}.$$

The derivative of the order ϵ approximation is

$$\frac{d\tilde{v}_1}{ds} = \frac{\left(\frac{1}{\tilde{a}\tilde{g}_M} + 2\tilde{v}_0 - v_{\min} - \tilde{E}_K\right)\left(\frac{d\tilde{v}_0}{ds}^2 + (\tilde{v}_0 - \tilde{E}_K)\frac{d^2\tilde{v}_0}{ds^2}\right) - 2(\tilde{v}_0 - \tilde{E}_K)\frac{d\tilde{v}_0}{ds}^2}{\left(\frac{1}{\tilde{a}\tilde{g}_M} + 2\tilde{v}_0 - v_{\min} - \tilde{E}_K\right)}.$$

Therefore

$$\frac{d\tilde{v}_1}{ds}(s^0_{\max}) = \frac{(\tilde{v}_0(s^0_{\max}) - \tilde{E}_K)}{\frac{1}{\tilde{a}\tilde{g}_M} + 2\tilde{v}_0(s^0_{\max}) - v_{\min} - \tilde{E}_K} \cdot \frac{d^2\tilde{v}_0}{ds^2}(s^0_{\max}).$$

It suffices to show that $\frac{d^2\tilde{v}_0}{ds^2}(s^0_{\max}) < 0$. The second derivative of the order 1 approximation is

$$\frac{d^2\tilde{v}_0}{ds^2} = \frac{-\pi\tilde{\Omega}_0\gamma(\tilde{v}_0 - \alpha)\sin(2\pi\tilde{\Omega}_0 s) - \cos(2\pi\tilde{\Omega}_0 s)\frac{d\tilde{v}_0}{ds}}{(\tilde{v}_0 - \alpha)^2}$$

and thus

$$\frac{d^2\tilde{v}_0}{ds^2}(s^0_{\max}) = \frac{-\pi\tilde{\Omega}_0\gamma}{\tilde{v}_0(s^0_{\max}) - \alpha} < 0$$

64

follows from $\tilde{v}_0 > \alpha$. A similar computation shows that $\frac{d\hat{v}_1}{ds}(s^0_{\min}) > 0$. Thus

$$\frac{d\tilde{v}}{ds}(s^0_{\max}) = \epsilon\tilde{\Omega}_0\frac{d\hat{v}_1}{ds}(s^0_{\max}) < 0.$$

Therefore there exists some $s_{\max} < s^0_{\max}$ such that

$$\tilde{v}(s_{\max}) = \tilde{v}_0(s_{\max}) + \epsilon\tilde{\Omega}_0\hat{v}_1(s_{\max}) > \tilde{v}_0(s^0_{\max}).$$

A similar argument can be made that there exists some $s_{\min} < s^0_{\min}$ such that

$$\tilde{v}(s_{\min}) = \tilde{v}_0(s_{\min}) + \epsilon\tilde{\Omega}_0\hat{v}_1(s_{\min}) < \tilde{v}_0(s^0_{\min}).$$

We expand $s^{\max} = s^{\max}_0 - \epsilon s^{\max}_1 + \cdots$ and $s^{\min} = s^{\min}_0 + \epsilon s^{\min}_1 + \cdots$ in ϵ where $s^{\max}_1, s^{\min}_1 > 0$ and $s^{\max}_1, s^{\min}_1 = \mathcal{O}(1)$. Then expanding $\tilde{v}(s^{\max})$ and $\tilde{v}(s^{\min})$,

$$\tilde{v}(s^{\max}) = \tilde{v}(s^{\max}_0 - \epsilon s^{\max}_1) = \tilde{v}(s^{\max}_0) - \epsilon s^{\max}_1\frac{d\tilde{v}}{ds}(s^{\max}_0) = \tilde{v}_0(s^{\max}_0) - \epsilon^2\tilde{\Omega}_0 s^{\max}_1\frac{d\hat{v}_1}{ds}(s^{\max}_0),$$

$$\tilde{v}(s^{\min}) = \tilde{v}(s^{\min}_0 + \epsilon s^{\min}_1) = \tilde{v}(s^{\min}_0) + \epsilon s^{\min}_1\frac{d\tilde{v}}{ds}(s^{\min}_0) = \tilde{v}_0(s^{\min}_0) + \epsilon^2\tilde{\Omega}_0 s^{\min}_1\frac{d\hat{v}_1}{ds}(s^{\min}_0).$$

The amplitude of the system to second order is

$$\tilde{A} = \frac{\tilde{v}(s^{\max}) - \tilde{v}(s^{\min})}{2}$$

$$= \frac{\tilde{v}_0(s^{\max}_0) - \tilde{v}_0(s^{\min}_0)}{2} + \epsilon^2\tilde{\Omega}_0\frac{-s^{\max}_1\frac{d\hat{v}_1}{ds}(s^{\max}_0) + s^{\min}_1\frac{d\hat{v}_1}{ds}(s^{\min}_0)}{2}$$

$$= \frac{\sqrt{\beta + \gamma} - \sqrt{\beta - \gamma}}{2}$$

$$\cdots + \epsilon^2\tilde{\Omega}_0\left(\frac{s^{\max}_1\pi^2\tilde{\Omega}_0\sqrt{\beta + \gamma}(\alpha + \sqrt{\beta + \gamma} - \tilde{E}_K)}{(\alpha\tilde{g}_M)^{-1} + 2\alpha + 2\sqrt{\beta + \gamma} - v_{\min} - \tilde{E}_K}\right.$$

$$\cdots \left. - \frac{s^{\min}_1\pi^2\tilde{\Omega}_0\sqrt{\beta - \gamma}(\alpha + \sqrt{\beta - \gamma} - \tilde{E}_K)}{(\alpha\tilde{g}_M)^{-1} + 2\alpha + 2\sqrt{\beta - \gamma} - v_{\min} - \tilde{E}_K}\right)$$

Note that $\frac{-s_1^{\max}\frac{d\hat{v}_1}{ds}(s_0^{\max})+s_1^{\min}\frac{d\hat{v}_1}{ds}(s_0^{\min})}{2} > 0$ and is $\mathcal{O}(1)$. Hence we write the amplitude of the system to second order as

$$\tilde{A} = \frac{\sqrt{\beta+\gamma}-\sqrt{\beta-\gamma}}{2} + \tilde{\Omega}F(s_1^{\max}, s_1^{\min}, \alpha, \beta, \gamma, \tilde{g}_M)$$

where $F > 0$ and $F = \mathcal{O}(1)$. Therefore the amplitude $\tilde{A}$ (and thus the gain $\tilde{G}$) of system (3.7) grows with input frequency $\tilde{\Omega}$ for $\tilde{\Omega} = \mathcal{O}(\epsilon^2)$.

When the M-current becomes non-activated for some portion of the solution, i.e. $\tilde{v}_0(s) < v_{\min}$ for some portion of the period, the minimum value of that solution is independent of the M-current (eq. 3.13) and $\tilde{v}(s_{\min}) = 0$. Following the same reasoning from the previous case,

$$\tilde{A} = \frac{\tilde{v}(s^{\max})}{2}$$

$$= \frac{\sqrt{\beta+\gamma}}{2} + \epsilon^2\tilde{\Omega}_0 \left(\frac{s_1^{\max}2\pi^2\tilde{\Omega}_0\sqrt{\beta+\gamma}(\alpha+\sqrt{\beta+\gamma}-\tilde{E}_K)}{(\alpha\tilde{g}_M)^{-1}+2\alpha+2\sqrt{\beta+\gamma}-v_{\min}-\tilde{E}_K} \right)$$

$$= \frac{\alpha+\sqrt{\beta+\gamma}}{2} + \tilde{\Omega} \left(\frac{s_1^{\max}\pi^2\tilde{\Omega}_0\sqrt{\beta+\gamma}(\alpha+\sqrt{\beta+\gamma}-\tilde{E}_K)}{(\alpha\tilde{g}_M)^{-1}+2\alpha+2\sqrt{\beta+\gamma}-v_{\min}-\tilde{E}_K} \right)$$

and we reach the same conclusion, i.e., the amplitude gain $\tilde{A}/A$ grows in $\tilde{\Omega}$ for $\tilde{\Omega} = \mathcal{O}(\epsilon^2)$.

3.7.2. Validation of Piece-Wise Linear Approximation of $\tilde{M}_\infty$ In Asymptotic Approximation for Gain of Model GIF Neuron with Low Frequency Input.

In this section, we validate our assumption of a piece-wise linear approximation of the steady-state M-current activation function in our analysis of the resonant behavior of the model GIF neuron. We consider two different cases: (1) Fix $f(\tilde{v}_T) = \tilde{M}_\infty(\tilde{v}_T)$ and vary the activation threshold value v_{min}. The equation for this approximation is given by

$$f(v; v_{\min}) = \begin{cases} \frac{\tilde{M}_\infty(\tilde{v}_T)}{\tilde{v}_T - v_{\min}} (\tilde{v} - v_{\min}) & \text{if } \tilde{v} \geq v_{\min} \\ 0 & \text{if } \tilde{v} < v_{\min} \end{cases},$$

and (2) Fix the activation threshold value v_{min} and vary a parameter $M_{\max}$ that determines the maximum value of f in the operating regime of the model. The equation for this approximation is given by

$$f(\tilde{v}; M_{\max}) = \begin{cases} \frac{M_{\max}}{\tilde{v}_T - v_{\min}} (\tilde{v} - v_{\min}) & \text{if } \tilde{v} \geq v_{\min} \\ 0 & \text{if } \tilde{v} < v_{\min} \end{cases}$$

Figure 3.11 shows the two types of approximations for various parameter values $M_{\max}$ and $v_{\min}$ along with the normalized gain curves for magnitude of M-current $\tilde{g}_M = 10, 100$. The approximation where $v_{\min}$ is fixed appears to result in a more accurate approximation of the gain curve $\tilde{G}$, especially when the limit of the gain $\tilde{G}$ is taken as $\tilde{\Omega} \to 0$. We compute the maximum gain, resonant frequency, and resonance length curves for each type of approximation to learn how these approximations change the response of the model GIF neuron to oscillatory input.

Figure 3.12 shows the maximum gain $G_{\max}$, resonant frequency $\tilde{\Omega}_{\text{res}}$, and resonance length $\tilde{\Omega}_{\text{len}}$ of the two different approximations for various parameter values $M_{\max}$ and $v_{\min}$. The second approximation scheme where $M_{\max}$ is varied and the activation threshold $v_{\min}$ is fixed results in more qualitatively accurate resonant behavior with respect to the full model and thus appears to be the more appropriate scheme to implement.
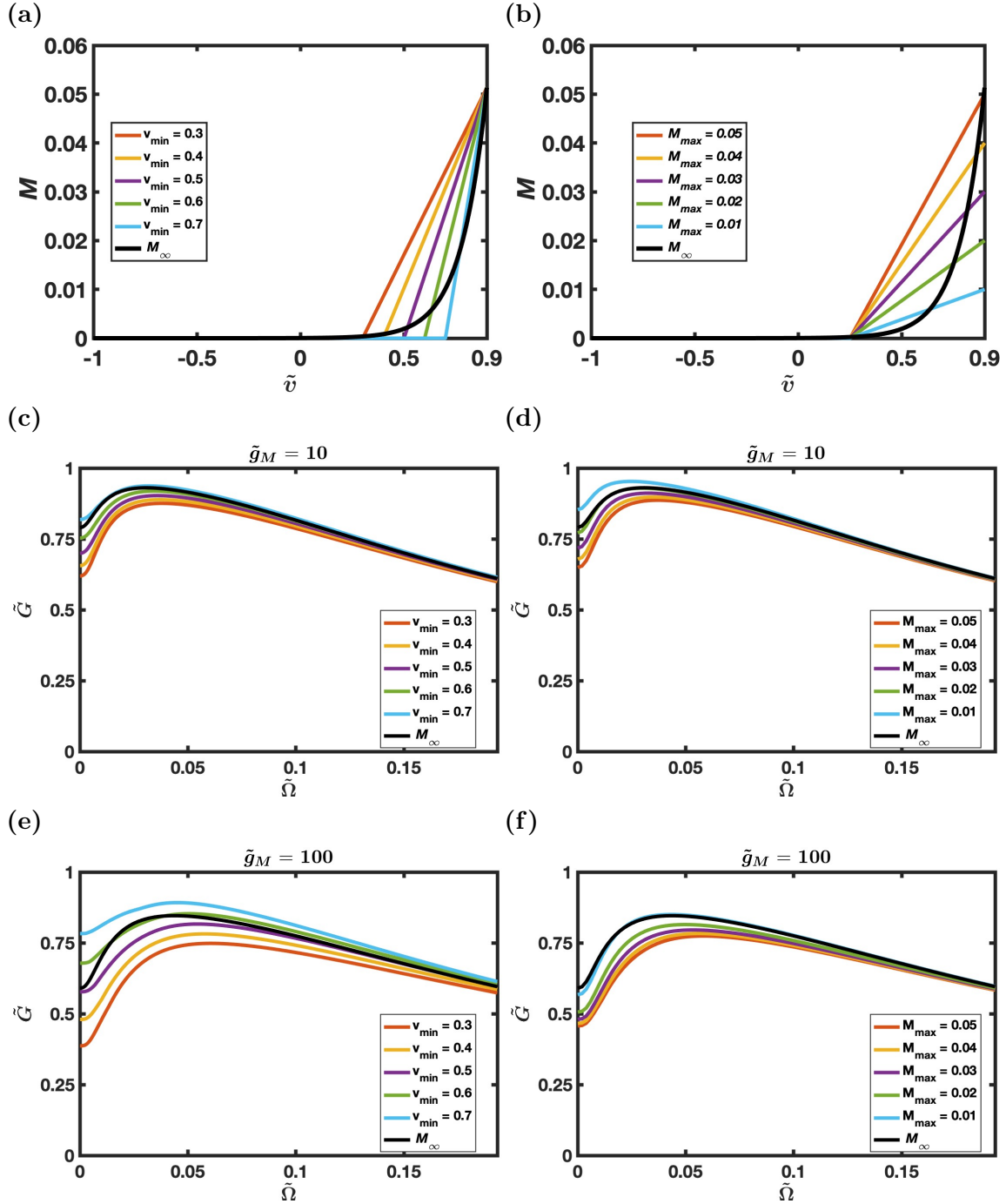
FIGURE 3.11. (a)-(b) Examples of different approximations for the steady-state activation curve $f(\tilde{v}) \approx \tilde{M}_\infty(\tilde{v})$. (c) - (f) Normalized gain for several approximation parameters. (a),(c),(e): Fix the maximum value of the activation curve at $f(\tilde{v}_T) = \tilde{M}_\infty(\tilde{v}_T)$ and vary the activation threshold v_{min}. (b,)(d),(f): Fixing the activation threshold and varying the maximum value of the approximated steady-state curve.
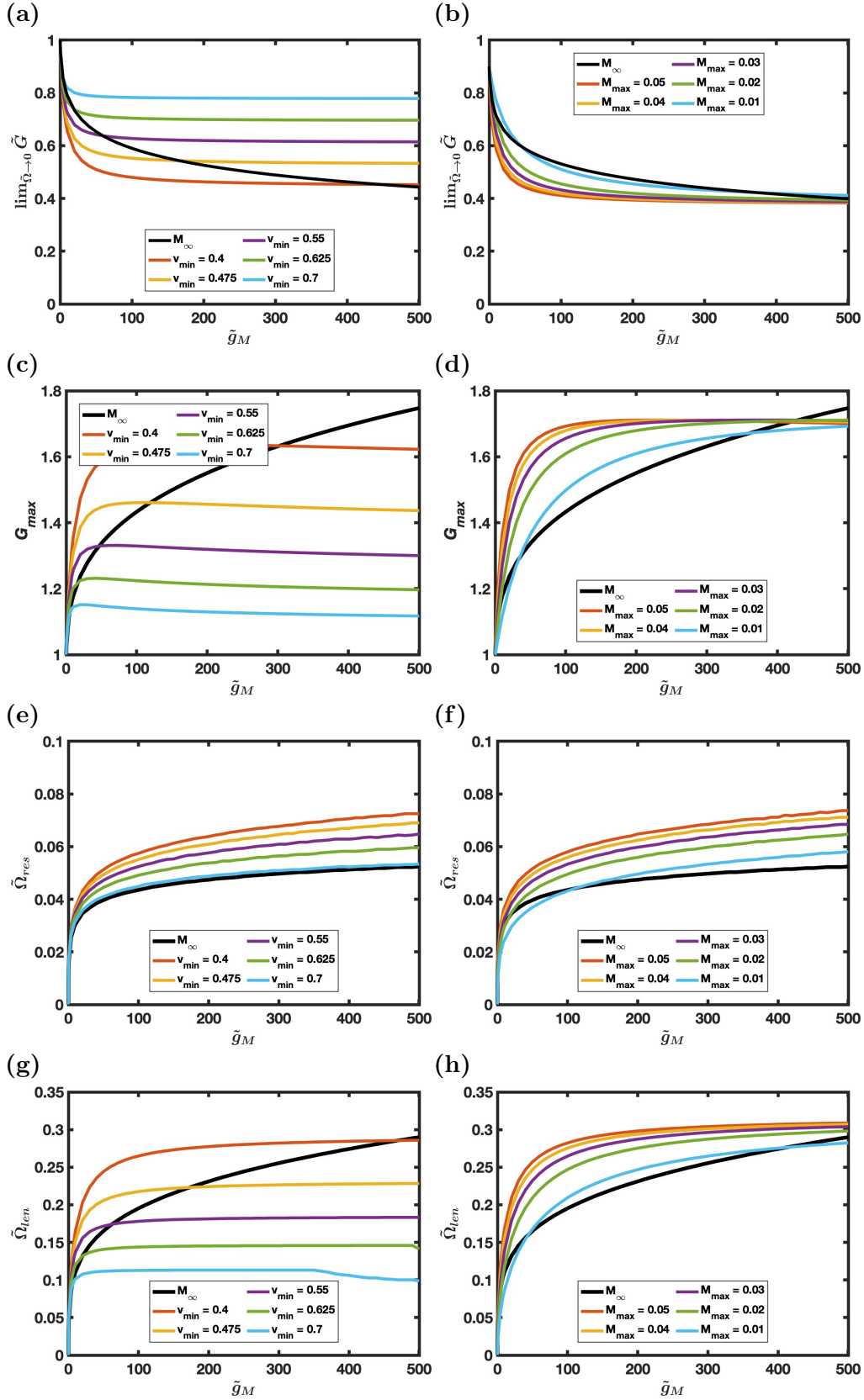
69

FIGURE 3.12. Effects on maximum gain, resonant frequency, and resonance length of different approximation schemes for the function $f(\tilde{v}) \approx \tilde{M}_\infty(\tilde{v})$ compared with those from full model with $\tilde{M}_\infty$ as functions of the nondimensional maximal M-current conductance parameter $\tilde{g}_M$. Left column: approximation scheme (1) where $v_{\min}$ is the varied parameter. right column: approximation scheme (2) where $M_{\max}$ is the varied parameter. (a)-(b) Limit of gain of model GIF neuron in response to oscillatory input $\tilde{G}$ as frequency of input approaches 0. (c)-(d) Maximum gain $G_{\max}$ (e)-(f) Resonant frequency $\tilde{\Omega}_{\text{res}}$. (g)-(h) Resonance length $\tilde{\Omega}_{\text{len}}$.

CHAPTER 4

M-Current Promotes Bistability in ICNS Network: Insights from Firing Rate Model

The details included in the cell-based ICNS network model provide the ability to link firing dynamics to biophysical parameters. However, the complexity of the cell-based network model makes it difficult identify the dynamical mechanisms that influence the network behaviour and to characterize behavior over a large portion of parameter space. Mathematical reduction of the cell-based ICNS network model to a firing rate model yields a low-dimensional model that lends itself to mathematical analysis while preserving network-level activity. Such a low-dimensional model can include the effects of the M-current as an adaptation variable. Thus, a firing rate model can be used to identify dynamical mechanisms of network behavior and to predict further activity of the cell-based ICNS network model that is induced by the M-current.

In this chapter, we derive a firing rate model from data generated by the cell-based ICNS network model described in chapter 2. The firing rate model is two-dimensional with a mean firing rate $(r(t))$ of the network and an adaptation variable $(w(t))$ to model the mean activation of the M-current across cells in the network. We show that bistable and excitable dynamics emerge in the firing rate model, and utilize phase-plane and bifurcation analysis to gain an understanding of how certain parameters promote or inhibit the bistability or excitability. The analysis of the firing rate model indicates that the cell-based ICNS network model with default parameters is not bistable or excitable, but it predicts cell-based network model parameters that do yield bistability. We confirm firing rate model predictions and show bistability and excitability in the cell-based ICNS network model.

4.1. Reduction of ICNS Network Model to Firing Rate Model

Firing rate models are often implemented as a simplified version of a more complex and biophysically detailed model. They have been used to model the firing activity of a single neuron [**43**], a population of neurons [**8, 15, 52, 57, 58, 66**], and multiple interacting populations of neurons [**15,57,58,66**]. While rigorous analytical techniques exist for reducing cell-based network models to firing rate models, they are difficult to implement on models that include intra-network connections, adaptation, or non-constant input. Instead, we use a model fitting approach, where the steady-state firing rate and M-current activation of the cell-based ICNS network model neurons are averaged over the population and used to fit the parameters of the steady-state firing rate and adaptation functions that govern the dynamics of the firing rate model.

4.1.1. Mean Firing Rate $r(t)$**.** We define the mean firing rate (or population firing rate) $r(t)$ of the ICNS network model as the ratio of the number of action potentials fired per unit time to the number of neurons in the population, thus the units of firing rate are spikes per neuron per second. In this chapter, for convenience, we drop the "mean" and refer to $r(t)$ simply as firing rate. More precisely, the firing rate of the cell-based ICNS network model $r(t)$ at time t (msec) is defined as the number of spikes in a sliding window around t divided by the number of neurons N and window length Δt

$$r(t) = 1000 \frac{|\{t_j \in S \mid t_j \in [t - \frac{\Delta t}{2}, t + \frac{\Delta t}{2}]\}|}{N \Delta t}$$

where $S = \{t_1, t_2, ..., t_K\}$ are the spike times of all cells in the network. (For the edge cases $t < \Delta t/2$, or $t > T - \Delta t/2$ where T is total simulation time, we shrink the appropriate side of the window and account for the change in Δt.) We also define the mean adaptation level of the network model $w(t)$ as the level of M-current activation averaged across the population

$$w(t) = \frac{1}{N} \sum_{j=1}^{N} w_j(t),$$

72

where $w_j(t)$ is the M-current activation variable of a neuron j in the network. Figure 4.1 shows examples of two raster plots of neurons from the cell-based ICNS network model, as well as the corresponding firing rate $r(t)$ and the adaptation $w(t)$, in response to constant input current and sinusoidal input current.

Note that changing the window length Δt affects the smoothness of the resulting mean firing rate, and thus we choose a value of the window length that reflects the expected time-scale of changes in the firing rate of the network. In this chapter, we focus on the effects of the M-current on the model (e.g., bistability) that occurs on a slow time-scale and hence we choose a window length $\Delta t = 100$ msec to ensure a clear representation of data while preserving the response of the network.
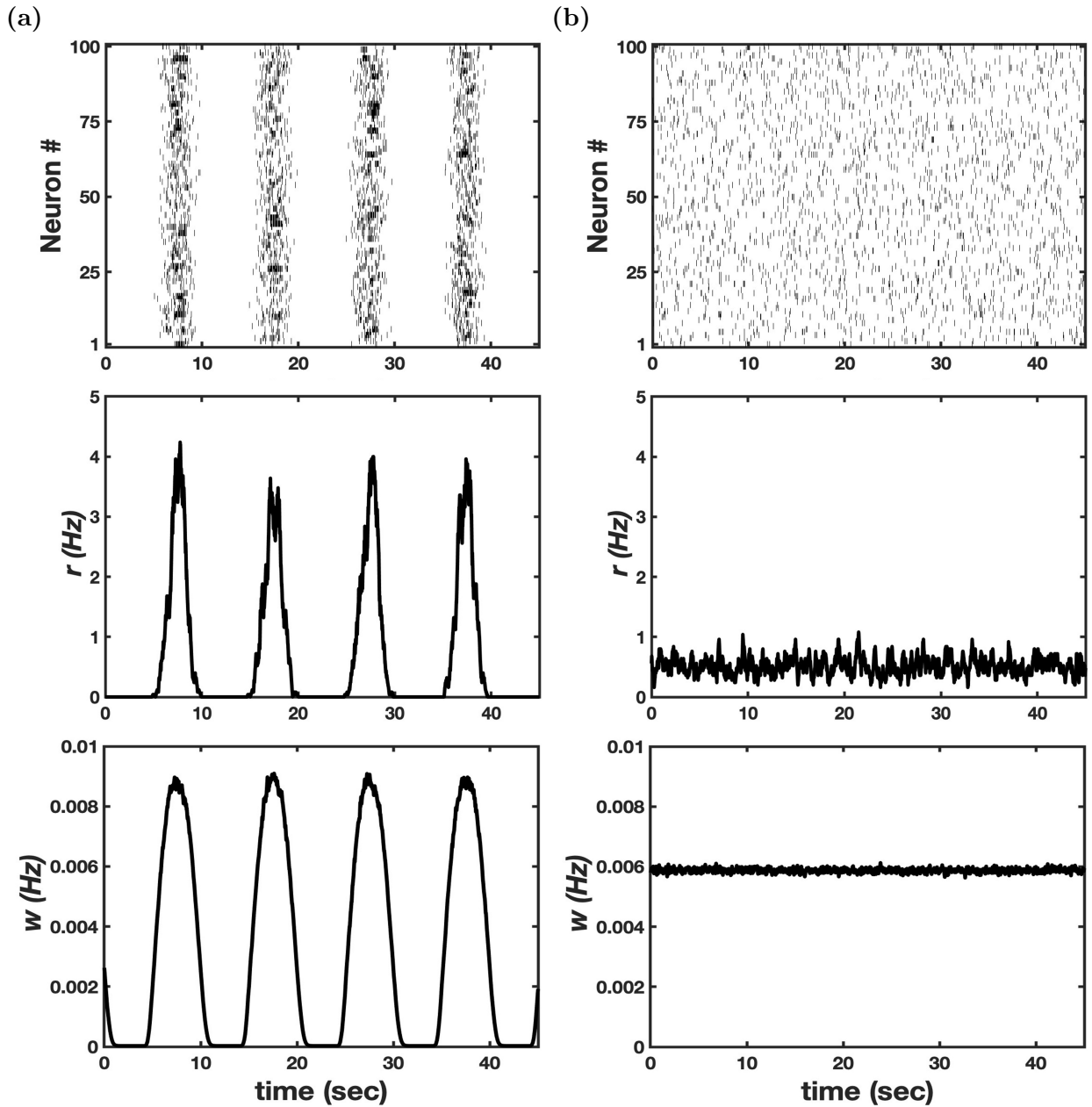
FIGURE 4.1. Raster plot (top), firing rate $r(t)$ (middle), and adaptation $w(t)$ (bottom) of cell-based ICNS network model simulations in response to two type of input for 60 sec of simulated time with first 15 seconds omitted to acount for transient dynamics. (a) sinusoidal input current, (b) constant input current.

4.1.2. Firing Rate Model Description. The structure of our firing rate model (schematic shown in figure 4.2) includes (1) Input $I(t) = \lambda(t)$ where λ describes a random process determining the spike times of the pre-synaptic input to the network, (2) the effect of recurrent connections proportional to the firing rate of the network with strength α to model intra-network synaptic inputs, and (3) an adaptation variable w that models the mean level of M-current activation over cells in the the network model. These elements are included to capture the mechanisms from the cell-based ICNS network model that have a significant impact on the macro-level.
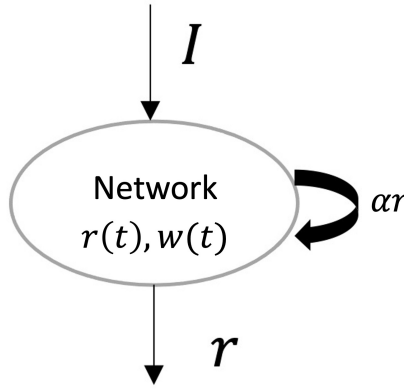

FIGURE 4.2. Schematic of firing rate model with input I and recurrent connections. r is the firing rate, and w is the intrinsic adaptation variable w.

The firing rate model takes the form

$$(4.1) \qquad \tau_r \frac{dr}{dt} = -r + f(I + \alpha r - \beta w)$$

$$(4.2) \qquad \tau_w \frac{dw}{dt} = -w + w_\infty(r)$$

where τ_r, τ_w are the time-constants of the firing rate and adaptation, respectively. $f(I_{tot})$ is the steady-state mean firing rate of the ICNS network model at constant total input I_{tot}, $w_\infty(r)$ is the steady-state adaptation level of the ICNS network at firing rate r, α is the strength of recurrent connections, and β is the strength of the adaptation.

The steady-state firing rate function is assumed to be a sigmoidal function (i.e., a Hill or Naka-Rushton function [**29**])

75

$$(4.3) \qquad f(I) = r_{\max} \frac{I^n}{I^n + I_{\text{half}}^n},$$

where $r_{\max}$ is the maximum mean firing rate of the network, I_{half} is the total input at which the firing rate is half-maximum, and n determines the steepness of the sigmoidal function. The steady-state adaptation function is assumed to take the form

$$(4.4) \qquad w_\infty(r) = a(e^{-br} - e^{-cr}) + d,$$

where a determines the maximal steady-state adaptation level, b and c determine the rate of rise and decay of $w_\infty(r)$, and d is the mean adaptation level when the network is inactive $(r = 0)$. The choice of the forms of f and w_∞ was informed by the dynamics of the network model and M-current (figure 4.3).

4.1.3. Fitting Firing Rate Model Parameters to Cell-Based ICNS Network Model Data. Careful consideration must be taken during fitting the firing rate model to cell-based network model data. Specifically, the mean firing rate data (figure 4.3) in the cell-based network model arises from the combination of impact from external input, input from recurrent connections, and effects of the M-current. Therefore, each of these components must be included in the fitting and reduction process. When the firing rate of the network is at steady-state with a constant input I, $\frac{dr}{dt} = 0$, and $\frac{dw}{dt} = 0$, and thus

$$(4.5) \qquad \begin{aligned} r^* &= f(I + \alpha r^* - \beta w^*), \\ w^* &= w_\infty(r^*). \end{aligned}$$

or

$$(4.6) \qquad \begin{aligned} I &= f^{-1}(r^*) - \alpha r^* + \beta w^* \\ w^* &= w_\infty(r^*). \end{aligned}$$

where r^* and w^* are the steady-state values of r and w.

To obtain the data $(r^*, w^*; I)$ for the parameter fitting of the firing rate model, simulations of the cell-based ICNS network model were run with various values of constant input I, (i.e. $I = A_t$ and $A_p = 0$, where A_t and A_p are the magnitude of the tonic and periodic portions of the input, respectively) for 315 sec with the first 15 seconds omitted to account for transient dynamics. The values of I were chosen to allow the fit of the data to capture the qualitative features of the steady-state firing function of the cell-based network model.

We then obtained the parameters of the steady-state firing rate model $(\alpha, \beta, I_{half}, r_{max}, n, a, b, c, d)$ by applying the least-squares method to the $(r^*, w^*; I)$ data from the cell-based ICNS network model to the steady-state firing rate model functions in equation (4.6). The data from the cell-based network model and the fit of the firing rate model is shown in figure 4.3, and parameters fit from this reduction process are listed in table 4.1.
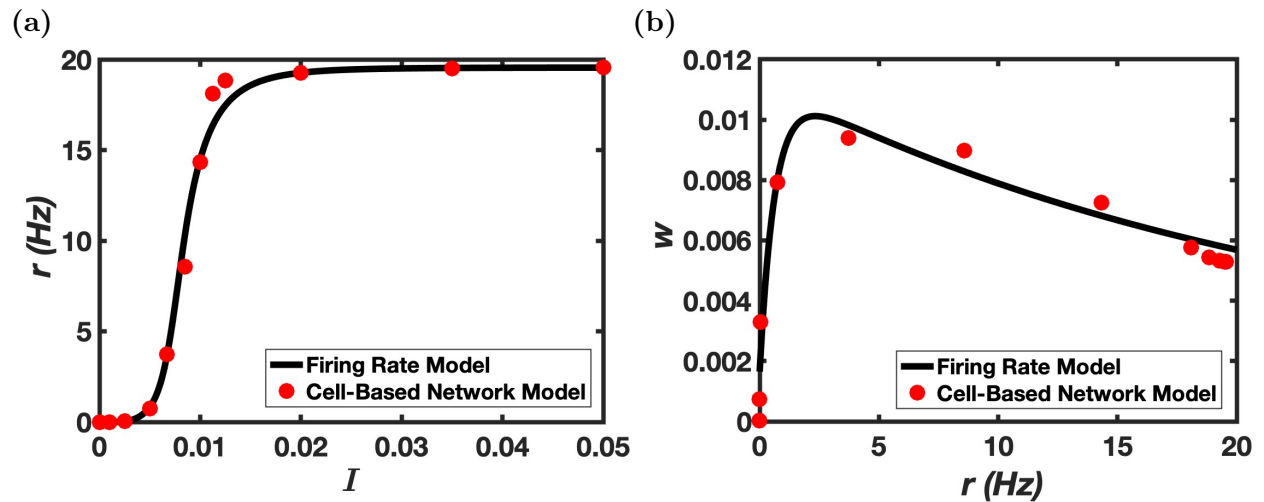
(a) **(b)**

FIGURE 4.3. Steady-state data from the cell-based ICNS network model and the fit of the firing rate model. Network simulation in red with $N = 100$ neurons. Data recorded from 315 sec simulated time with first 15 seconds omitted to take into account transient firing. (a) Steady-state firing rate as a function of the strength of input I. (b) Steady-state adaptation level of network as a function of the steady-state firing rate. Parameters for the firing rate model are shown in table 4.1.

Fitting the time-constants τ_r and τ_w requires time series data from the cell-based ICNS network model that provides information about the dynamics of the mean firing rate and adaptation level of the network. To generate this data, simulations of the cell-based ICNS network model were run constant input $(A_t = I_0, A_p = 0)$ until it reached steady-state firing and adaptation level. Then, a step change in the input was made $(A_t = I_1, A_p = 0)$, and exponentials were fit to the time-series data of the mean firing rate $r(t)$ and adaptation level $w(t)$ of the cell-based ICNS network model. Figure 4.4 shows an example of this data for $I_0 = 0.01$ and $I_1 = 0.0065$. This process was repeated for various values of I_0 and I_1 to obtain a distribution of potential τ_r and τ_w values. This distribution was used to constrain the fitting of τ_r and τ_w. The values obtained through the fitting process are shown in table 4.1.
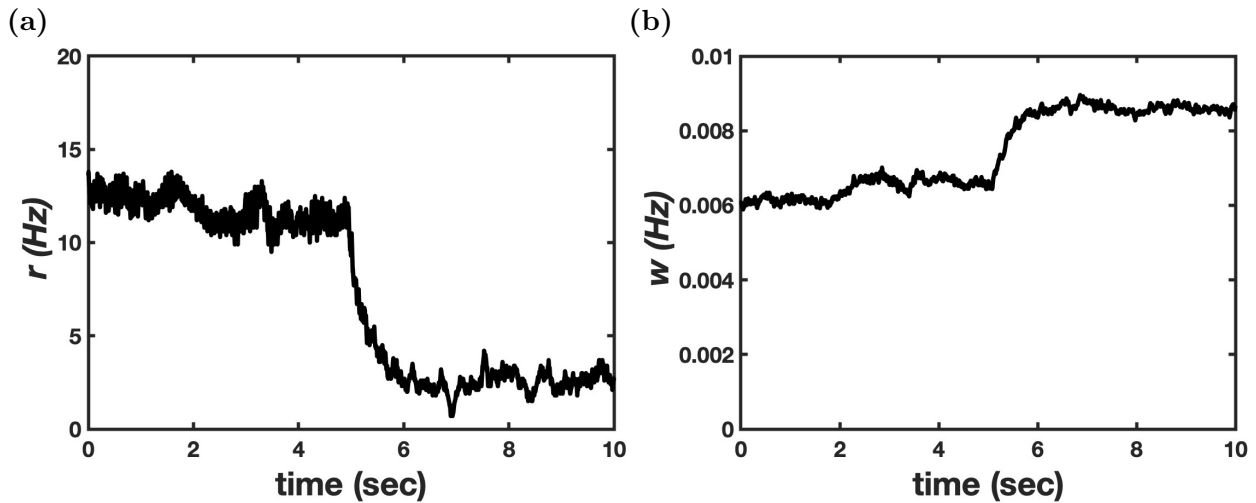

FIGURE 4.4. Response of cell-based ICNS network model to a step change in input from $I_0 = 0.01$ to $I_1 = 0.0065$ at $t = 5$ sec. (a) Mean firing rate $r(t)$, (b) adaptation level $w(t)$.

Parameter	Value
$r_{\max}$	19.55308 Hz
I_{half}	0.009
n	5.7
α	0.000108 sec
β	0.05
a	0.00964
b	0.0435 Hz^{-1}
c	1.584 Hz^{-1}
d	0.00165
τ_r	100 msec^{-1}
τ_w	165 msec^{-1}

TABLE 4.1. Default parameter values of the firing rate model of the ICNS network. Values obtained through fitting process described in text. Note that the input parameter I is a control parameter.

4.2. Bistability & Excitability In Firing Rate Model of ICNS Network

4.2.1. Dynamics of Default Firing Rate Model of ICNS Network. The dynamics of the default firing rate model are relatively simple. Figure 4.5 shows examples of these simple dynamics. Figures 4.5a and 4.5b plot two firing rate solutions $r(t)$ to the default firing rate model for different initial conditions. The firing rate solutions $r(t)$ asymptotically approaches steady-states for both values of input I. Figures 4.5c and 4.5d plot the corresponding phase-planes of the default firing rate model with nullclines and solutions. In each case, only one fixed point exists, which is a stable node in both cases. The solutions in each figure asymptotically approach the stable fixed point (r^*, w^*) for both initial conditions $(r(0), w(0))$. The steady-state firing rate r^* increases with I, consistent with the behavior of the cell-based ICNS network model.
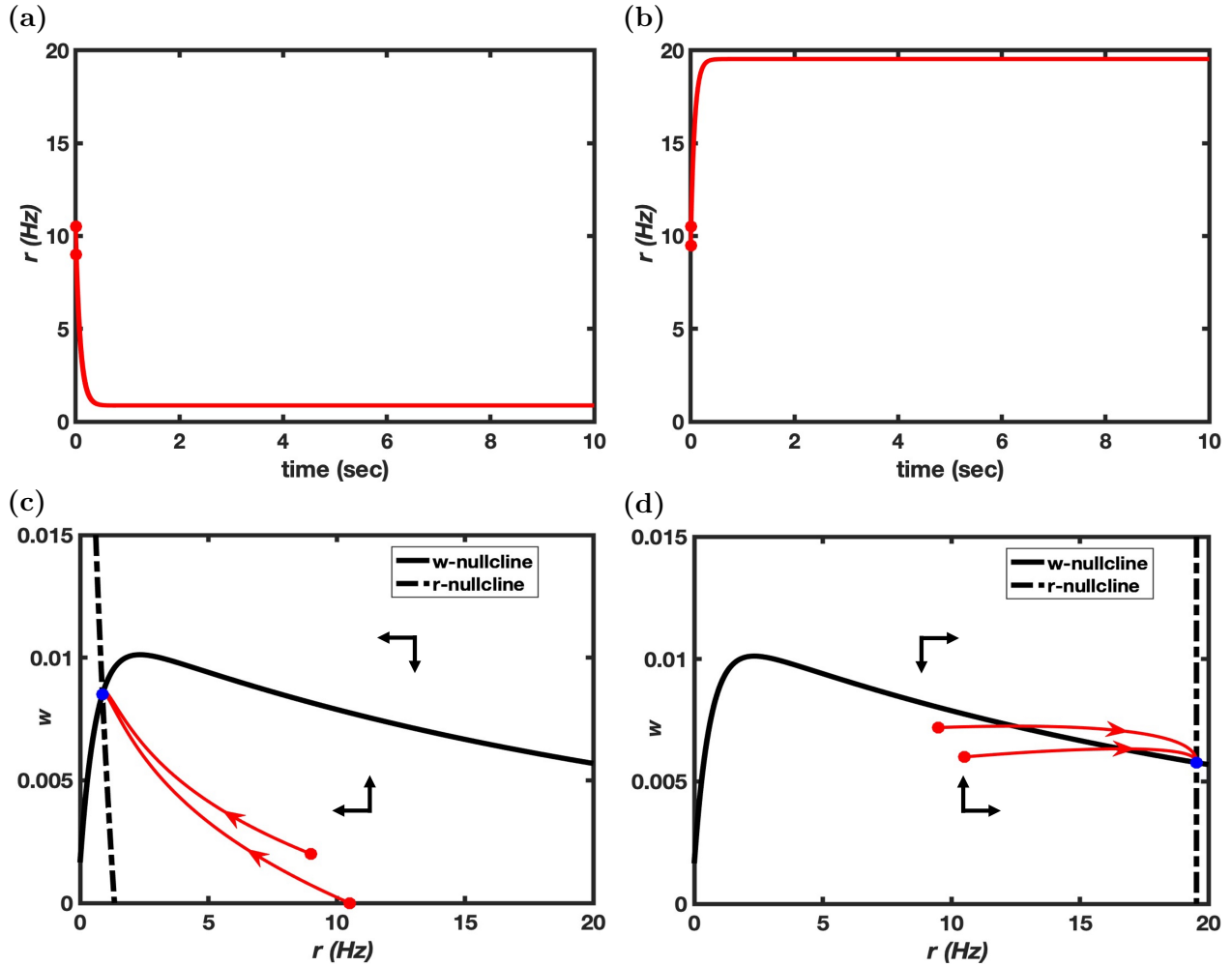
79

FIGURE 4.5. Default firing rate model dynamics for (a),(c) input value $I = 0.005$ and (b),(d) input value $I = 0.0375$ with small differences in initial conditions $(r(0), w(0))$. (a)-(b) time series of firing rate solutions $r(t)$. (c)-(d) Phase-plane in (r, w) space with black curves to indicate nullclines, red curves to indicate solutions, blue dots to indicate steady-states, and black arrows to indicate qualitative dynamics of region.

4.2.2. Bistability in Firing Rate Model. While the default firing rate model expresses relatively simple dynamics, we find that changes in recurrent connection strength α or adaptation strength β can lead to the emergence of bistable dynamics. Figure 4.6 plots the time-series of the firing rate solution $r(t)$ and the corresponding phase-plane of the firing rate model with default parameters except for changes in α or β as indicated in the figure. The initial conditions and input value I for the simulations with a change in α (figures 4.6a & 4.6c) are the same as those in figure 4.5c, and the initial conditions and input value I for the simulations with a change in β (figures 4.6b & 4.6d) are the same as those in figure 4.5c.

Both of the firing rate solutions $r(t)$ in figures 4.6c increase initially. However, the larger solution asymptotically approaches a larger steady-state, while the smaller solution stops increasing and then decays to a smaller steady-state. Similar dynamics occur in figure 4.6c, but the smaller solution decays quickly and then oscillates for a short period of time before settling around the steady-state. This implies that, in both altered parameter sets, the firing rate model displays bistability. We can see these bistable dynamics in the phase-plane of the firing rate model in figures 4.6b & 4.6d. The change in α and β bestowed the system with three steady-states: two stable and one unstable.
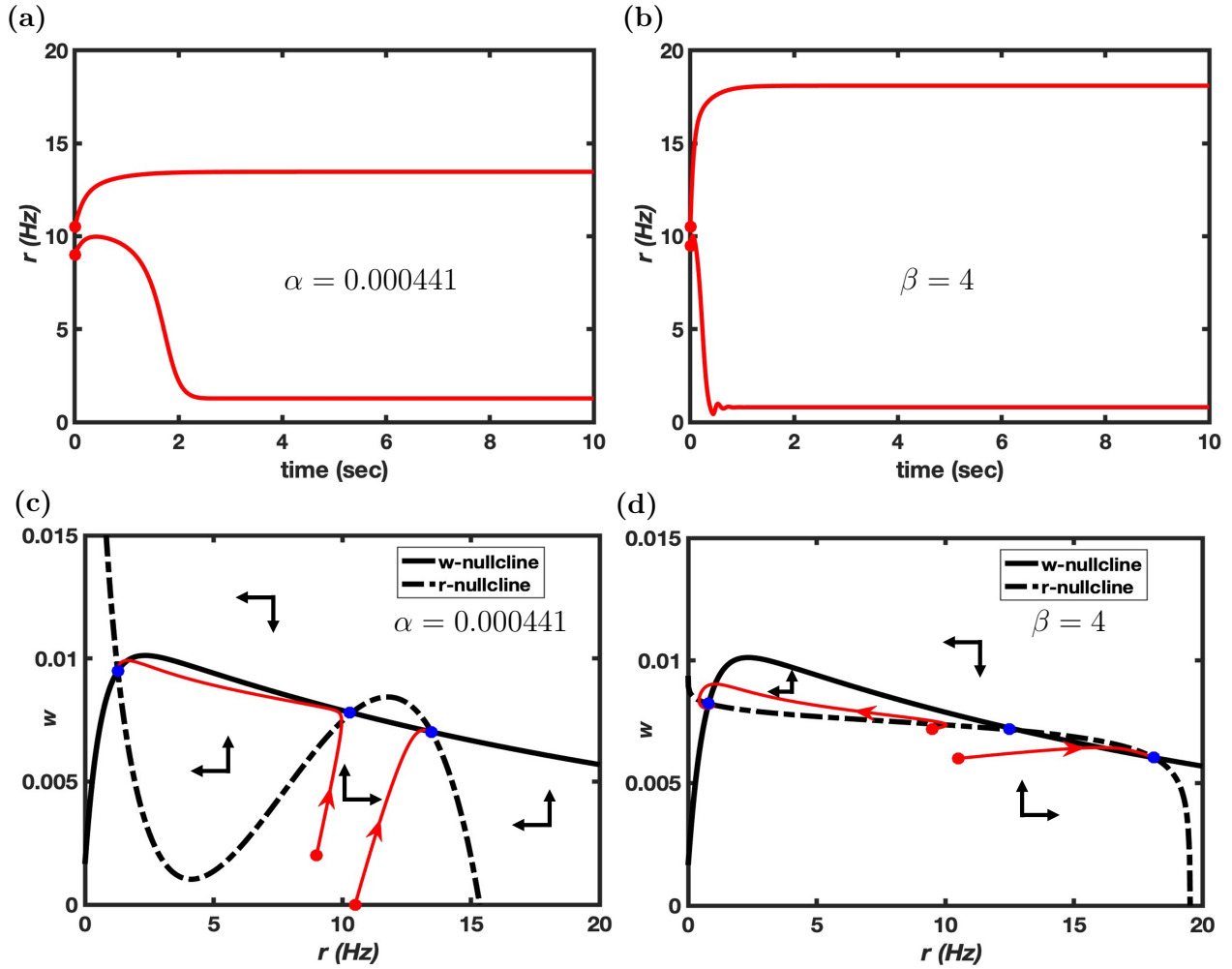
FIGURE 4.6. Changing the parameter values of α or β bestows the firing rate model with bistable dynamics. (a)-(b) Firing rate solutions $r(t)$ approaching two different steady-states, (c)-(d) Phase-plane of firing rate model shows three steady-states. black curves indicate nullclines, red curves indicate solutions, black arrows indicate qualitative dynamics of the region. Parameters different from default set indicated in figures. Input constant at $I = 0.005$ in (a),(c) and $I = 0.0375$ in (b),(d).

4.2.3. Excitability In Firing Rate Model. The bistable dynamics observed in the previous subsection imply that excitable dynamics can emerge with further parameter changes. In fact, implementing the same two parameter sets and set of initial conditions in the firing rate model as in the previous subsection but decreasing the input value(s) I results in the excitable dynamics shown in figure 4.7.

Figures 4.7a and 4.7b plot the firing rate solution $r(t)$ of the firing rate model for altered α and altered β, respectively. The solution with the smaller firing rates decay to a low firing rate steady state value, but the larger solutions show excitation, increasing in magnitude and remaining at the "active" state (high firing rate state) before decaying to the low firing rate steady-state after a time period on the order of seconds. The corresponding phase-planes in figures 4.7c and 4.7d show that the slight decrease in I results in a loss of the larger two steady-states compared to figures 4.6c and 4.6d. The solution(s) that exhibit excitation first approach where the larger stable fixed points were, and then eventually decay back to the lone remaining fixed point.

Quantifying the parameter changes that promote bistability or excitability in the firing rate model can provide insight into parameter values that could endow the cell-based network model with bistable dynamics. In the following section, we perform bifurcation and parameter sensitivity analysis on the firing rate model to gain an understanding of how bistability is detered or promoted.
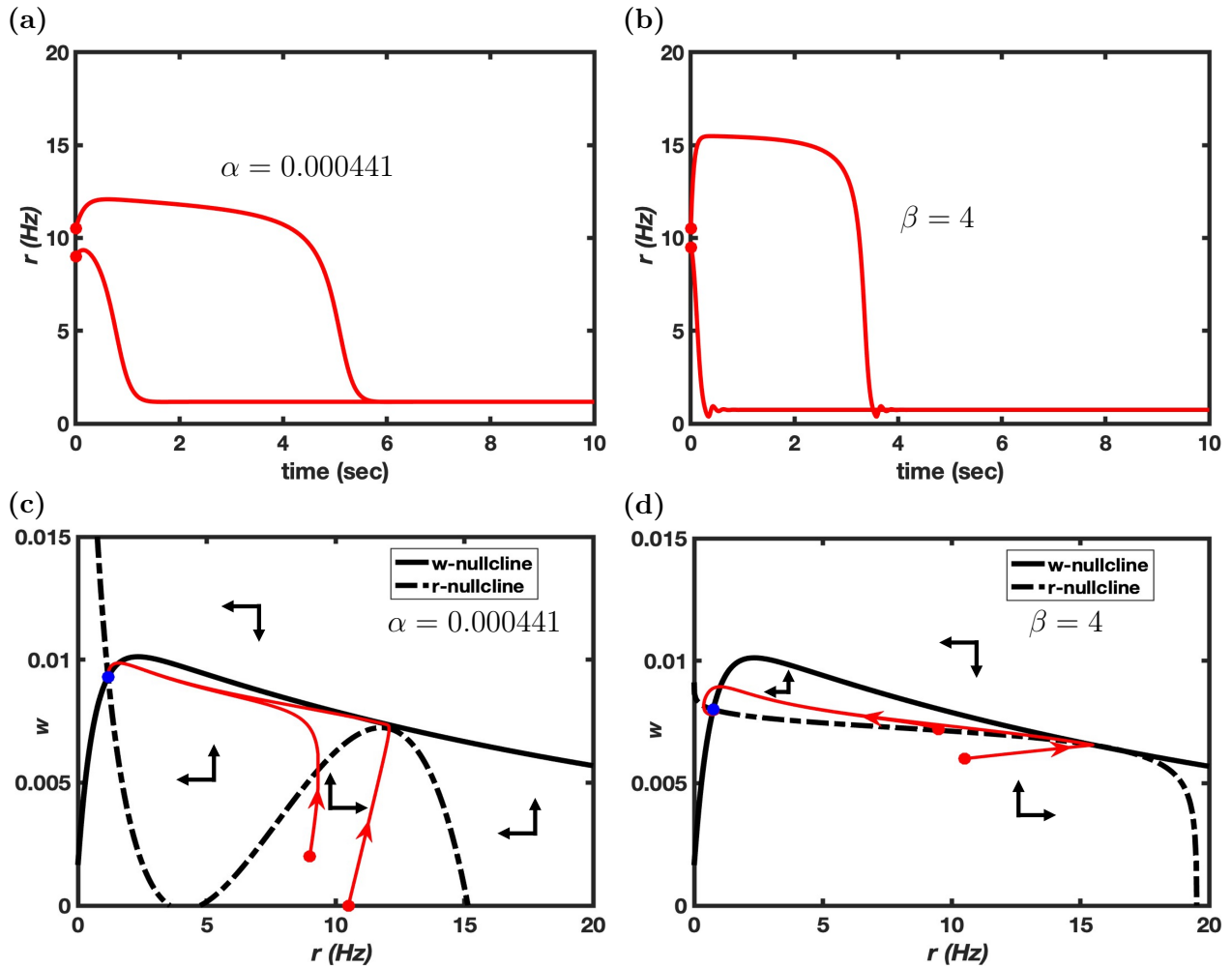
FIGURE 4.7. Changing the values of α or β and slightly decreasing the input value I bestows the firing rate model with excitable dynamics. (a)-(b) Firing rate solutions $r(t)$ showing excitation before approaching a steady-state, (c)-(d) Phase-plane of firing rate model shows a single steady-state. Black curves indicate nullclines, red curves indicate solutions, black arrows indicate qualitative dynamics of the region. Parameters different from default set indicated in figures. Input constant at $I = 0.00499$ in (a),(c) and $I = 0.0365$ in (b),(d).

4.3. Bifurcation & Parameter Sensitivity Analysis of Firing Rate Model

In the previous section, we observed that bistable dynamics emerge when changes to recurrent connection strength α and adaptatation strength β, i.e., the system gained two new fixed points. The standard mechanism through which a system gains/loses two fixed points is called a saddle-node bifurcation [74]. A saddle-node bifurcation occurs when, as a parameter is (continuously) varied, two fixed points move together, collide, and are subsequently destroyed [74]. The bifurcation point occurs at the parameter value that the two fixed points collide. (Note that this can also happen in reverse, where a single fixed point appears and then splits into two distinct fixed points).

In this section, phase-plane and bifurcation analysis are used to analyze the firing rate model and explore the sensitivity of the bistable dynamics observed in section 4.2 to parameter changes. First, the dynamics of the default firing rate model is examined through variation of the input control parameter I. Next, the sensitivity of the default firing rate model to changes in recurrent connection strength α and adaptation strength β is explored. The saddle-node bifurcations that emerge as a result of the changes in α and β represent a transition from monostable dynamics to bistable dynamics, providing a natural method to map the regions in parameter spaces that correspond to bistable dynamics. Then, we show that the non-monotonicity of the steady-state adaptation function $w_\infty(r)$ promotes bistability in the firing rate model.

Note that excitable dynamics can occur when the firing rate model is monostable but parameter values are sufficiently close to a parameter set that corresponds to a saddle-node bifurcation (e.g., figures 4.7c, 4.7d). (XPPAUTO software was used to generate the bifurcation data presented in this chapter.)

4.3.1. Effects of Input Magnitude: I.

The single fixed point of the default firing rate model for various input values I shown in section 4.2 implied that the dynamics of the default firing rate model are simple, i.e., no bifurcations emerge as a result of the variation of the input control parameter I. Figure 4.8a plots the (r, w) phase-plane for various input values

I. As I changes, the r-nullcline moves across the (r, w) plane, but for all valuees of I there is only one intersect of the w-nullcline. Furthermore, no qualitative changes to the phase plane occur as I is varied. Figure 4.8b plots a bifurcation diagram for the firing rate model in (r, I) space. A single, stable fixed point exists for all values of the input control parameter I, and no saddle-node bifurcations occur as I is varied. This implies that the default firing rate model does not exhibit bistable dynamics, which is consistent with cell-based network model simulations. However, the results in section 4.2 for the firing rate model suggest that changes to the recurrent connection strength α and adaptation strength β parameters can alter the qualitative dynamics of the firing rate model and induce saddle-node bifurcations, i.e., promote bistability.
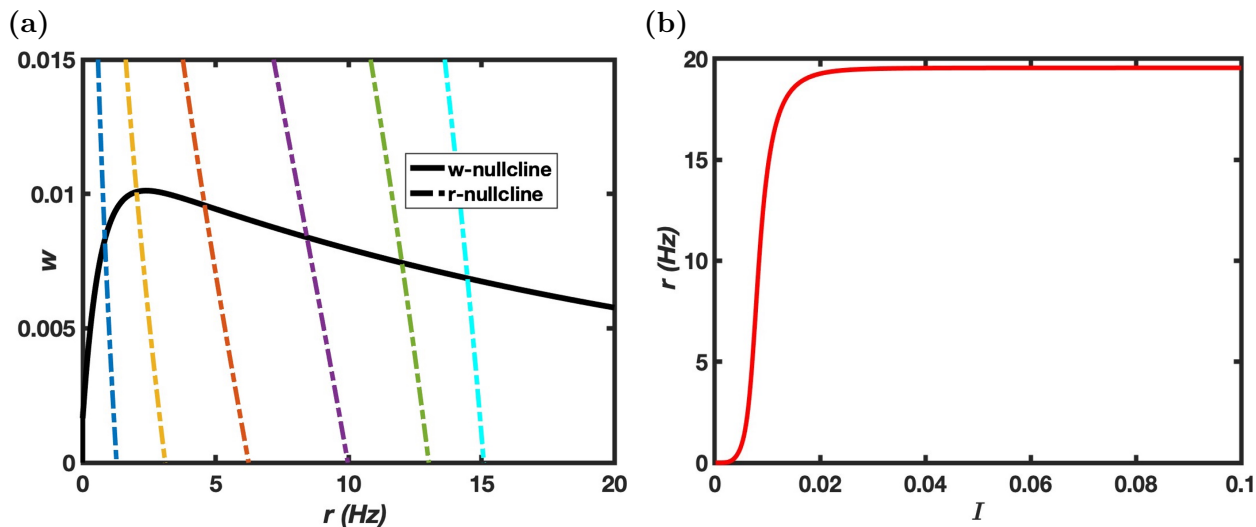

FIGURE 4.8. Steady-states in the default parameter regime change a function of the constant input parameter I. (a) Phase-plane with w-nullcline in solid black, and r-nullclines for various values of I (from left to right, $I = 0.005, 0.006, 0.007, 0.008, 0.009, 0.01$). (b) Single-parameter bifurcation diagram of the fixed points of the firing rate $r = r^*$ of the default firing rate model as a function of the input parameter I. Note that this is the steady-state $f - I$ curve.

4.3.2. Effects of Recurrent Connection Strength: α. In section 4.2, we observed that an increase in recurrent connection strength α led to the emergence of bistable dynamics in the firing rate model. Note that, $\alpha > 0$ implies that recurrent coonnections in the network have a net excitatory effect on the network, whereas if $\alpha < 0$, then the recurrent connections have a net inihibitory effect. The default recurrent connection strength $\alpha = 0.000108 > 0$ implies that the firing rate model upregulates its own activity, and suggests that the recurrent connections in the cell-based network model have a net excitatory effect on.

Figure 4.9a plots the (r, w) phase plane for the default firing rate model with input value $I = 0.005$ and various r-nullclines that depend on the recurrent connection strength parameter α. Two saddle-node bifurcations occur at two critical values of the recurrent connection strength parameter (see the yellow and purple r-nullclines). When α is between these two critical values, the firing rate model has three fixed points (bistable), otherwise a single fixed point exists (monostable). Figure 4.9b plots a bifurcation diagram of the firing rate model in the (α, r) parameter space with $I = 0.005$. The red curves indicate stable fixed points, and the black curve indicates saddle points. Thus, bistability exists when the system has 3 fixed points - two stable and one saddle.
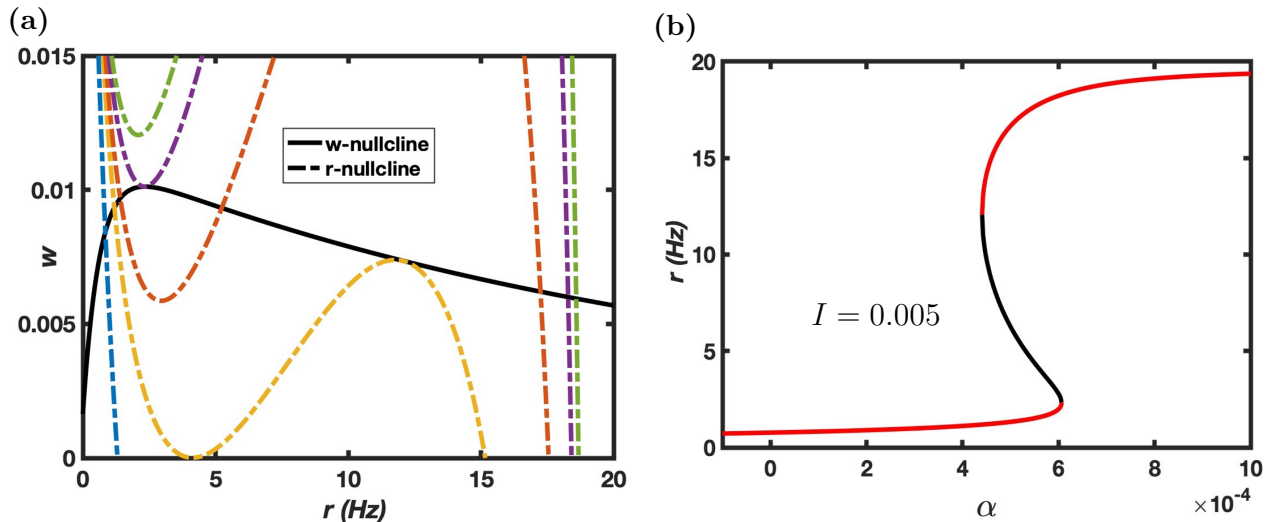
FIGURE 4.9. Steady-states of the default firing rate model with fixed input $I = 0.005$ change as a function of the recurrent connection strength parameter α. (a) Phase-plane with w-nullcline in solid black and various r-nullclines in dashed colors. From left to right, $\alpha = 0.000108$ (blue), 0.000440786 (yellow), 0.000525 (orange), 0.000606325 (purple), 0.00065 (green). (b) Single-parameter bifurcation diagram of the fixed points of the firing rate $r = r^*$ of the firing rate model as a function of the parameter α with constant input $I = 0.005$ shows bistability. Red curves indicate stable fixed points, black curve indicates saddle points.

The range of α values that result in bistability can change with the input I. Next, we examine the relationship between α and I to determine the sensitivity of bistable dynamics in the firing rate model to changes in the recurrent connection strength α. Figure 4.10 plots a two parameter bifurcation diagram for the default firing rate model in (α, I) parameter space. The red curve plots saddle-node bifurcations, separating (α, I) space into two regions with distinct dynamics: monostable (single, stable fixed point) and bistable (two stable fixed points and a saddle point). The blue, yellow, red, purple, and green dots correspond to the parameter values of the nullclines in figure 4.9a. (The blue dot in the monostable region represents the default firing rate model at $I = 0.005$). In figure 4.10, the robustness of the bistable dynamics are maximized at a value $\alpha_c = 0.0007912$, i.e., bistability exists for the largest range of input values I at this value of $\alpha = \alpha_c$.

The bifurcation analysis in this subsection implies that bistability does not exist in the firing rate model if the recurrent connection strength is not sufficiently large, which suggests that in the cell-based network model, the strength of the intra-network excitatory synapses compared to the intra-network inhibitory synapses can determine if the network exhibits bistability.
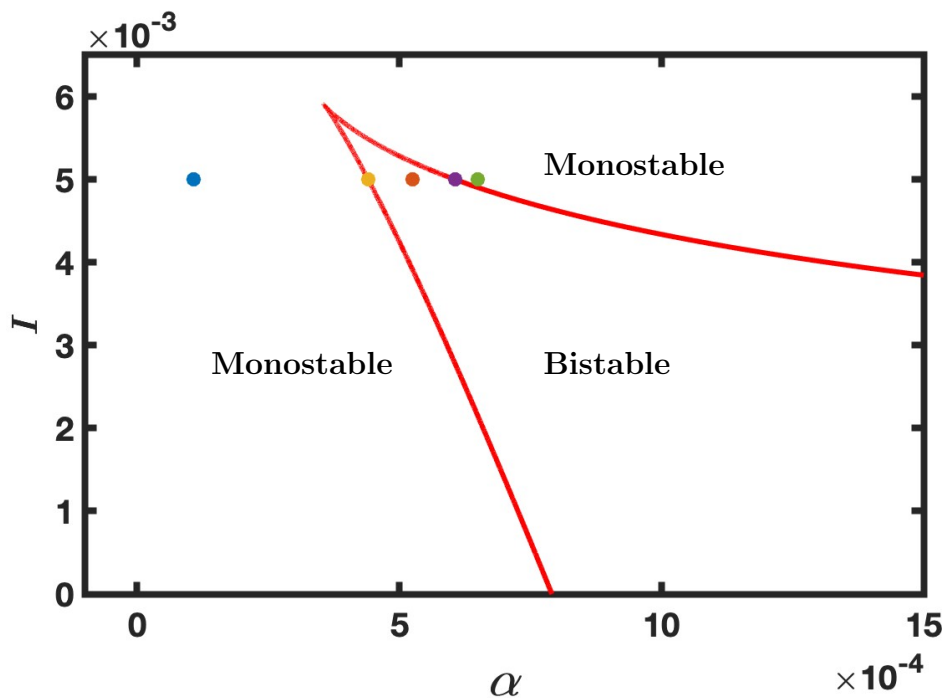

FIGURE 4.10. Two parameter bifurcation diagram in (α, I) parameter space. The red curve plots saddle-node bifurcations and separates the space into two regions: monostable (single, stable fixed point) and bistable (two stable fixed points, one saddle point). The colored dots correspond to the parameters of the firing rate model in figure 4.9a. An extended version of this figure for larger α values is shown in Appendix figure 4.21a.

4.3.3. Effects of Adaptation Strength: β. Adaptation strength β is a measure of how much influence the M-current exerts on the firing rate model. Note that we restrict our analysis to $\beta \geq 0$ as the M-current has an "inhibitory" effect. Figure 4.11a plots the (r, w) phase-plane of the default firing rate model with r-nullclines for several values of the adaptation strength β. Two saddle-node bifurcations occur at critical values of β. Bistable dynamics occur when β is between the two critical values. Figure 4.12 plots a bifurcation diagram in the (β, I) parameter space with fixed input $I = 0.05$, explicitly showing the range of adaptation strength β values for which bistability occurs.
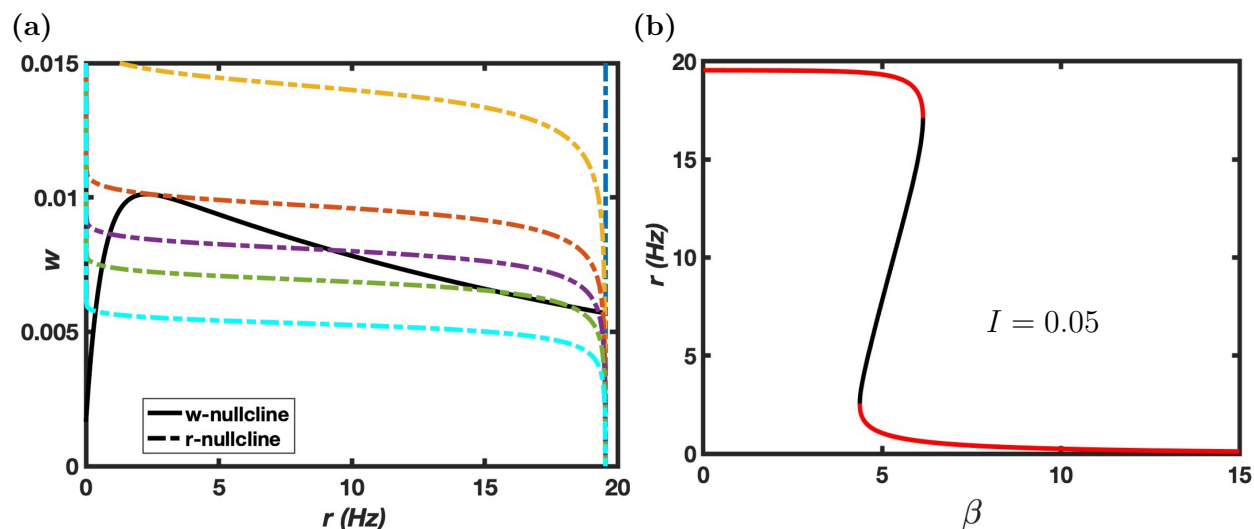

FIGURE 4.11. Steady-states of the default firing rate model with fixed input $I = 0.005$ change as a function of the adaptation strength parameter β. (a) Phase-plane with w-nullcline in solid black and various r-nullclines in dashed colors. From left to right, $\beta = 0.0.05$ (blue), 3 (yellow), 4.377 (orange), 5.25 (purple), 6.125 (green), 8 (light blue). (b) Single-parameter bifurcation diagram of the fixed points of the firing rate $r = r^*$ of the default firing rate model as a function of the parameter β with constant input $I = 0.05$ shows bistability. Red curves plots stable fixed points, black curve plots saddle points

The range of β values that result in bistable dynamics changes with the input I. Figure 4.12 plots a two parameter bifurcation diagram of the firing rate model in (β, I) parameter space. The red bifurcation curve plots saddle-node bifurcations, and splits the (β, I) space into distinct bistable and monostable regions. The range of input values I that lead to bistable dynamics in the firing rate model increases as β increases, i.e., the robustness of the

bistability increases with β. The bifurcation diagram also shows that bistability does not exist in the default firing rate model below a critical value of $\beta \sim 0.015$. This implies that the M-current is necessary for the firing rate model (with default parameters), and thus the cell-based network model (with default parameters), to show bistability.
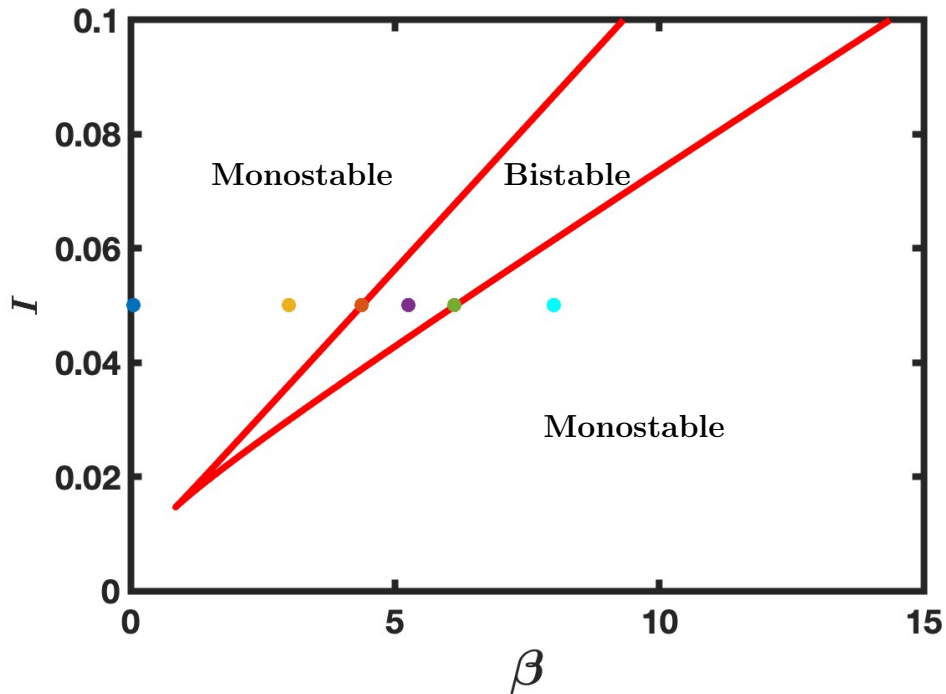

FIGURE 4.12. Two parameter bifurcation diagram in (β, I) parameter space. The red curve plots saddle-node bifurcations and separates the space into two regions: monostable (single, stable fixed point) and bistable (two stable fixed points, one saddle point). The colored dots correspond to the parameters of the firing rate model in figure 4.11a.

4.3.4. Recurrent Connection Strength α and Adaptation Strength β Can Promote Bistability. The behavior of the default firing rate model responds to changes in the recurrent connection strength α and the adaptation strength β, i.e., the qualitative dynamics of the default firing rate model can change from monostable to bistable through changes in α or β. However, the analysis done so far relied on changing only one parameter (recall that the input I is a control parameter).

Figure 4.13 plots a two parameter bifurcation diagram of the firing rate model in (α, β) parameter space for various input values I, with the red curves indicating saddle-node

bifurcations. The shape of the bistable region does not change with I and exists inside the cone-like region contained by the saddle-node bifurcation curves. Both recurrent connection strength α and adaptation strength β play an important role in the promotion of bistability. If recurrent connection strength α and/or adaptation strength β are sufficiently small, e.g. default firing rate parameters (blue dot in figure 4.13), no bistable dynamics emerge for any input I. However, a region in (α, β) parameter space where α and β are relatively large exists where bistable dynamics occur for all input values I. This region is labeled "Bistable" in figure 4.13. This implies that the M-current and the intra-network synaptic connections play a key role in the promotion of bistability in the cell-based network model.
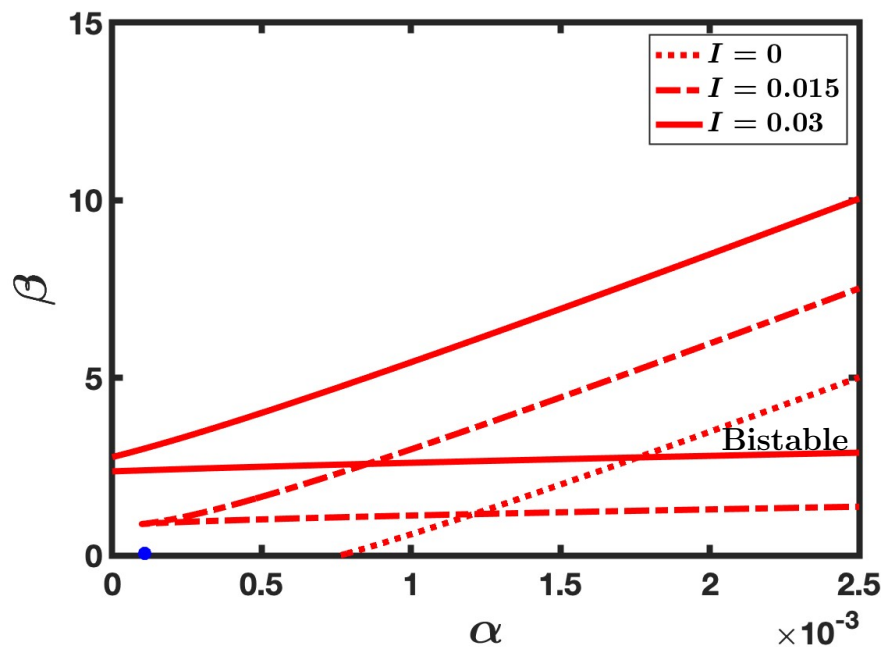

FIGURE 4.13. Two parameter bifurcation diagrams of firing rate model in (α, β) parameter space for various input values I. Red curve(s) indicate saddle-node bifurcations and separate the space into monostable and bistable regions. Geometry of bistable region does not change with I. Monostable region exists outside of cone-like region contained by bifurcation curvs, bistable region is contained inside cone-like region bounded by saddle-node curve(s). Shared region of bistability for all I values is labeled "Bistable". Blue dot corresponds to default values $\alpha = 0.000108$, $\beta = 0.05$ and is in the monostable region for all input I values.

4.3.5. Firing Rate Model Not Sensitive to Remaining Parameters. Bifurcation and sensitivity analysis of the default firing rate model revealed that only recurrent connection strength α and adaptation strength β significantly affect the existence of bistability. Changing any of the parameters n, I_{half}, r_{max}, a,b,c, or d do not result in saddle-node bifurcations, and thus do not result in bistability. However, changes in the decay parameter b can, when combined with changes in α and β, lead to insight into the role of the non-monotonicity of the steady-state adaptation curve in promoting bistable dynamics. This is presented in section 4.4 and Appendix 4.5.3.

4.4. M-Current Promotes Bistability in Firing Rate Model

Recall that the steady-state adaptation curve $w_\infty(r)$ of the default firing rate model is non-monotonic (figure 4.3b). The steady-state adaptation curve is

$$w_\infty(r) = a(e^{-br} - e^{-dr}) + d.$$

Figure 4.15a plots the steady-state adaptation curve for various values of the decay parameter b, showing that the (non-)monotonicity of the steady-state adaptation curve can be controlled with a single parameter (b) and can be classified into two parameter domains: non-monotonic if $b > 0$, and monotonic with no limit if $b < 0$.

In this section, the non-monotonicity of the steady-state adaptation function $w_\infty(r)$ is shown to promote robust bistable dynamics in the firing rate model by altering the bistable regions in the (α, I) and (β, I) parameter space, i.e., the non-monotonicity of the adaptation function increases the range of recurrent connection strength α and adaptation strength β parameter values that lead to bistability in the firing rate model.

Figure 4.14b plots two parameter bifurcation diagrams of the default firing rate model in the (α, I) parameter space for various decay parameters b with the corresponding $w_\infty(r)$ functions plotted in figure 4.14a. The bifurcation curve shifts in the (α, I) space as the decay parameter b changes. The minimum recurrent connection strength α required for the

firing rate model to express bistable dynamics is smaller when the adaptation curve is non-monotonic ($b > 0$) than the monotonic cases ($b \leq 0$). We note that the shift of the bistable region in (α, I) parameter space is relatively small, thus the sensitivity of bistability in the firing rate model (with respect to recurrent connection strength α and input I) to changes in the decay parameter b is low.
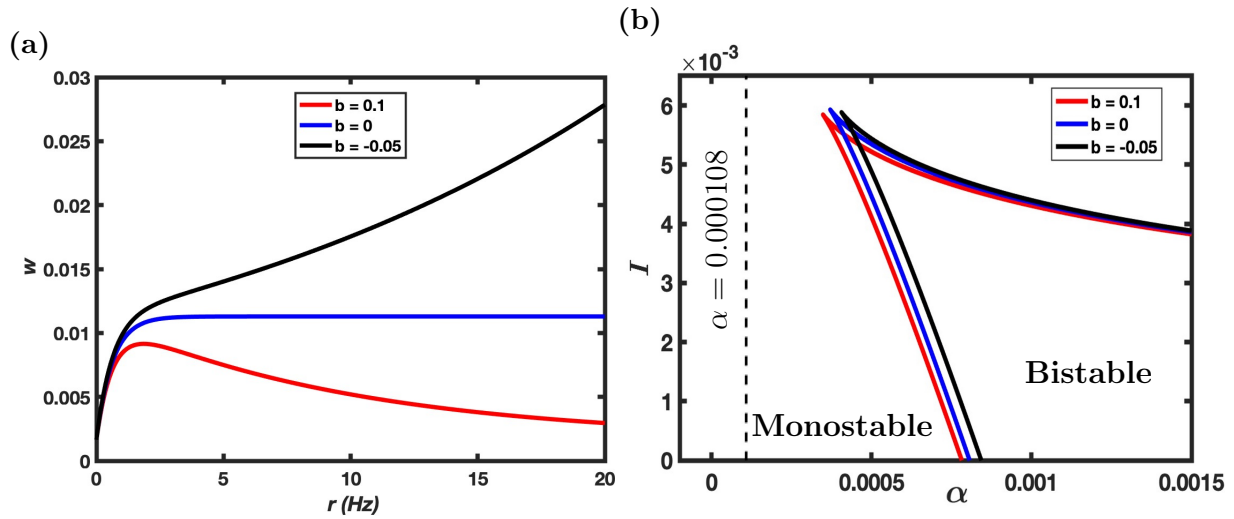

FIGURE 4.14. (a) Three examples of steady-state adaptation curve $w_\infty(r)$ for various values of decay paramter b. (b) Two-parameter bifurcation diagram(s) in (α, I) parameter space. Solid curves plot saddle-node bifurcations for various decay parameters b of the steady-state adaptation curve w_∞ and separate the space into monostable and bistable regions. Default recurrent connection strength parameter $\alpha = 0.000108$ shown as dashed curve.

Figure 4.15b plots two parameter bifurcation diagrams of the default firing rate model in the (β, I) parameter space for various decay parameters b with the corresponding $w_\infty(r)$ functions plotted in figure 4.15a. The bifurcation curves enclosing the bistable region in the (β, I) space form a cone: As the decay parameter b changes, the area of the cone changes, and the cone shifts. An example of this change is shown in figure 4.15b - the area of the bistable region decreases to 0 as the adaptation curve $w_\infty(r)$ approaches monotonicity. The sensitivity of the bistable region to changes in b is high, implying that both adaptation strength β and the non-monotonicity of the adaptation curve $b < 0$ interact to promote bistability. Both of these parameters stem from the M-current, suggesting that the M-current plays a pivotal role in the promotion of bistability in the cell-based network model.
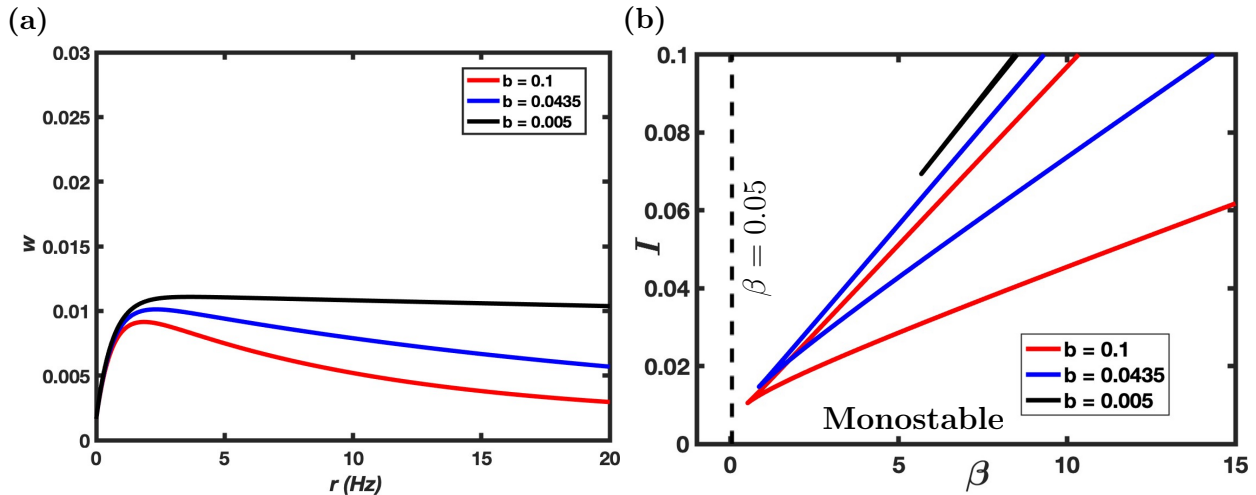

FIGURE 4.15. (a) Adaptation curve $w_\infty(r)$ for various decay parameters b. (b) Two-parameter bifurcation diagrams in (β, I) parameter space. Solid curves plot saddle-node bifurcations for various decay parameters b of the steady-state adaptation curve $w_\infty(r)$ and separate the space into monostable and bistable regions. Bistable regions are contained inside the cone formed by the saddle-node bifurcation curve, monostable regions are outside of the cone. Area of bistable region decays to 0 as adaptation curve approaches monotonicity. Default adaptation strength parameter $\beta = 0.05$ shown as dashed curve.

4.5. Predictions from Firing Rate Model Verified in Cell-Based Network Model: Identification of Mechanisms that Promote Bistability

Analysis of our firing rate model indicates that changing recurrent connection strength α, adaptation strength β, and steady-state adaptation decay parameter b in a coordinated manner can promote bistable dynamics in the firing rate model. This suggests that changing corresponding parameters in the cell-based network model will also lead to bistable dynamics.

In order to test for bistability in the cell-based network model for various parameter sets, we apply a 0.1 sec stimulus pulse with amplitude 0.1 (as described in chapter 2 section 1.4) when it is in a non-active state to bring the network into a high activity state. We then determine if the network remains "indefinitely" in the high activity state after the stimulus is turned off.

4.5.1. Increased Recurrent Connection Strength Promotes Bistability. The recurrent connectiion strength α in the firing rate model relates to several parameters in the cell-based network model. Specifiically, increasing the maximal synaptic conductances $g_{syn,e/i}$, the probability of excitatory synaptic connections p, and the synaptic decay time-constant τ_d could be interpreted as increasing the effect of the recurrent connection strength. Therefore, we alter parameters in the cell-based model as follows: (1) Increase the maximal synaptic conductances to $g_{syn,e/i} = 5.7$ nS/cm^2, (2) Increase the probability of excitatory synaptic connections to $p = 0.8$, and (3) Increase the synaptic decay time-constant to $\tau_d = 25$ msec [**70**]. Furthermore, to increase the excitability of the model neurons, we (4) decrease the average threshold potential v_T, maximal leakage conductance g_L, and maximal delayed rectifier conductance g_K of the cells. For each neuron, these parameters are drawn from the uniform distribution $\mathcal{U}(0.95x, x)$, where $x = v_T, g_L, g_K$ are the values of parameters in our "default" cell-based network model.

Figure 4.16a plots the mean firing rate (r) of the cell-based network model with increased recurrent connection strength as a function of time. The network is in a non-active state $(r(t) = 0$ Hz) before the input pulse. When the input is turned on, the mean firing

96

rate of the network jumps to a highly active state ($r(t) \approx 15$ Hz) and remains in this state even after the input is turned off, and therefore the cell-based model displays bistable dynamics. Figure 4.16c plots the mean adaptation level (w) of the cell-based network model as a function of time. Following the mean firing rate, the adaptation level increases to a steady-state value when the input is turned on and remains there after the input is turned off. Figure 4.16e plots the average firing ratee and adaptation level in the (r, w) phase-plane. The solution trajectory ($r(t), w(t)$) is indicated by the black curves when the input is on ($I(t) = 0.1$), and indicated by the red curve when the input is off ($I(t) = 0$). The green and blue curves indicate putative $r-$ and $w-$nullclines (for $I(t) = 0$), respectively. The putative nullclines are based on insight from the analysis of the firing rate model. Note that, during and after the input pulse, the solution trajectory hover around a (presumed) high activity stable steady-state (i.e., the intersection of the nullcines).

We can destroy bistability in the system by decreasing other parameters related to recurrent connection strength α. For example, figures 4.16b, 4.16d, and 4.16f plot the mean firing rate, mean adaptation level, and (r, w) phase-plane, respectively, when the probability of excitatory neurons is decreased to $p_{ICNS,e} = 3.5 \ln(100)/99$. The mean firing rate and adaptation level increase while the input is turned on, but then decay down to 0 after the input is turned off. Note that, during the input pulse, the solution trajectory in the (r, w) phase-plane in figure 4.16f remains near the (presumed) stable fixed point that existed before reducing $p_{ICNS,e}$. However, when the input is turned off, the solution trajectories approach the non-active steady-state. This suggests that the reduced recurrent connection strength caused a saddle-node bifurcation that leads to the elimination of a stable fixed point and saddle point.
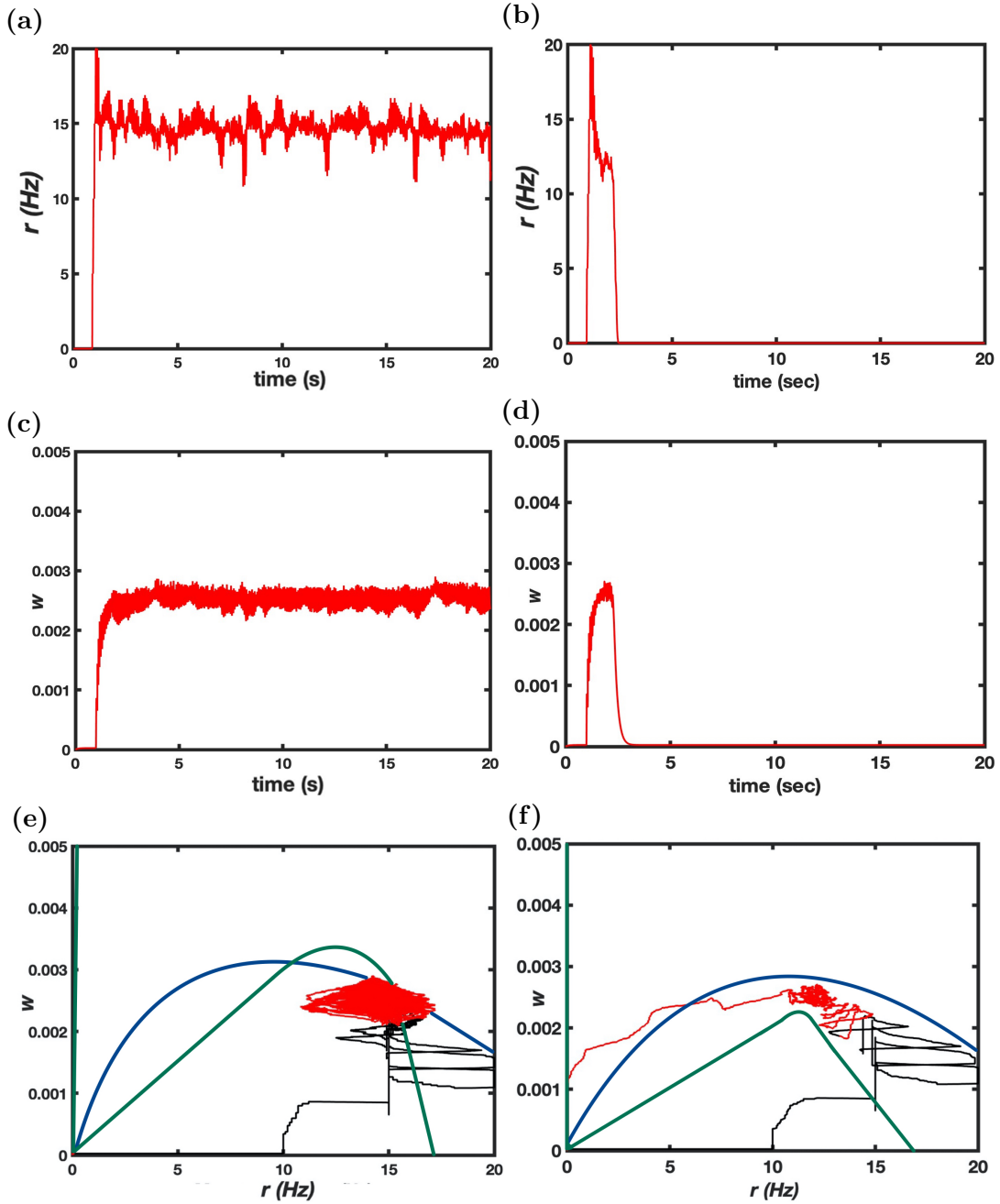
FIGURE 4.16. Mean firing rate and M-current activation data for a bistable (a),(c),(e) and excitable (b),(d),(f) network model in response to the pulse input $I(t)$. (a),(b) Mean firing rate r of the network model as a function of time. (c),(d) Mean adaptation w as a function of time (e),(f) Phase plane of r and w. Red curve indicates when input is off, black curve indicates input is on. Putative r-nullcline in green, putative w-nullcline in blue. Putative nullclines based on insight gained from analysis of the firing rate model, and indicate putative nullclines when there is no input ($I = 0$).

98

4.5.2. Decreased Adaptation Strength Promotes Bistability. Note that increasing the recurrent connection strength in the cell-based model bestowed the system with bistability for $I_{const} = 0$. This implies that our new parameter set for which the cell-based model displays bistability corresponds to the triangular region in figure 4.13 (for $I = 0$) where the firing rate model is bistable. Figure 4.13 predicts that increasing the adaptation strength β above a critical value will destroy bistability. This suggests that increasing the net effect of the M-current will destroy bistability in the cell-based network model.

Figures 4.17a, 4.17c, and 4.17e plot the mean firing rate, adaptation, and the (r, w) phase-plane of the cell-based network model from section 4.5.1 showing bistable dynamics. Figures 4.17b, 4.17d, and 4.17f show that increasing the average g_M value from 8 nS/cm^2 to 11 nS/cm^2 induces a loss of bistability. Specifically, increasing the average value of the maximal M-current conductance increases the net effect of the M-current in the cell-based network model and flattens the putative $r-$nullcline, inducing a saddle-node bifurcation and eliminating the possibility of bistability. Thus, in this case, increased adaptation strength deters bistable dynamics in the cell-based model.
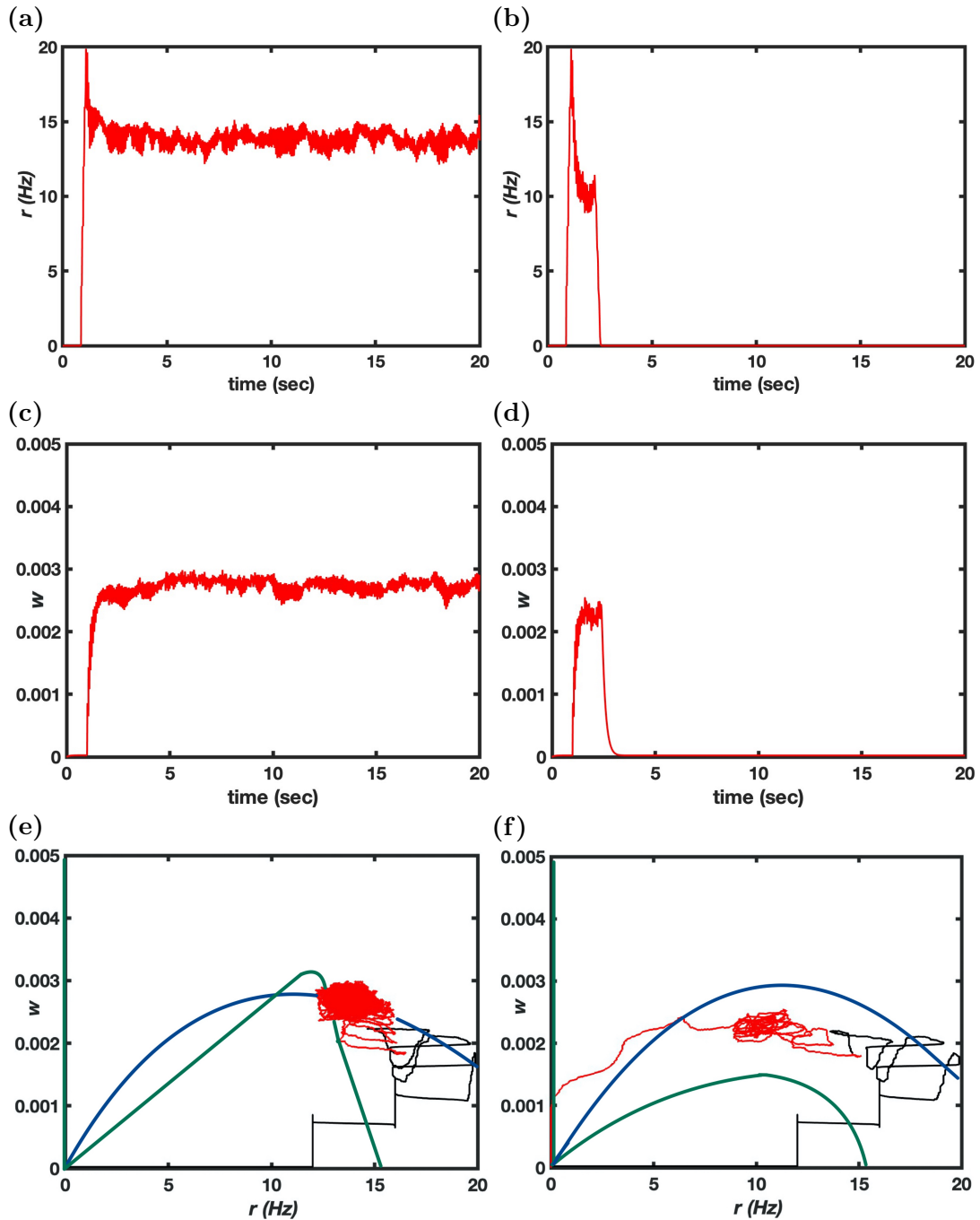
FIGURE 4.17. Mean firing rate and M-current activation data for a bistable (a),(c),(e) and excitable (b),(d),(f) network model in response to the pulse input $I(t)$. (a),(b) Mean firing rate r of the network model as a function of time. (c),(d) Mean adaptation w as a function of time (e),(f) Phase plane of r and w. Red curve indicates when input is off, black curve indicates input is on. Putative r-nullcline in green, putative w-nullcline in blue. Putative nullclines based on insight gained from analysis of the firing rate model, and indicate putative nullclines when there is no input ($I = 0$).

100

4.5.3. Non-Monotonicity of Steady-State Adaptation Curve Promotes Bista-bility. The steady-state adaptation curve in the default cell-based network model and firing rate model is non-monotonic (figure 4.3), i.e., as the firing rate increases the level of adaptation first increases and then decreases. The analysis of the firing rate model suggests that this non-monotonicity of the steady-state adaptation curve can promote bistability. Note that increased activation of the M-current during a spike can lead to a monotonic steady-state adaptation curve. Indeed, figures 4.18a and 4.18b plot the steady-state mean firing rate and adaptation level of the cell-based network model from section 4.5.1 with a 75% increase of the saturation factor Δw, respectively. Note that the steady-state adaptation curve is monotonic. Therefore, we examine the effects of increasing the saturation factor of the M-current (Δw) in the cell-based network model.
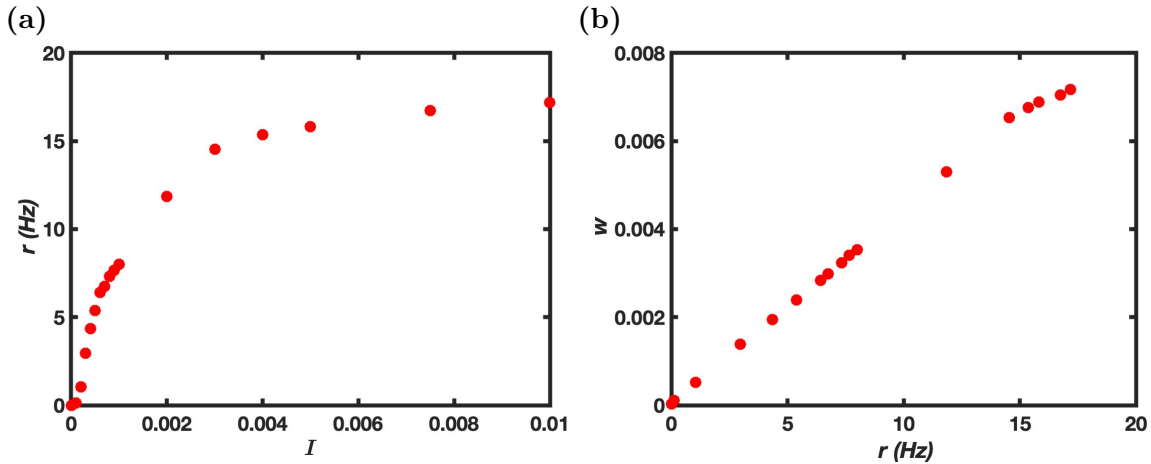

FIGURE 4.18. Mean steady-state firing rate and adaptation level from cell-based network model with an increased M-current saturation factor by 75% (Note that this parameter change does not result in any of the activation variables w elevating above the saturation value of 1). The mean steady-state adaptation curve is strictly monotonic. (a) Mean steady-state firing rate of the network $r = r_\infty$. (b) Mean steady-state adaptation of the network $w = w_\infty$ as function of the mean steady-state firing rate. The data was computed for various constant input values $I(t)$ from 315 seconds of simulated time with 15 seconds removed to account for transience.

Figure 4.19 plots the mean firing rate, adaptation, and (r, w) phase-planes. Figures 4.19a, 4.19c, and 4.19e plot the mean firing rate, adaptation level, and phase plane of the cell-based network model from section 4.5.1 showing bistable dynamics. Figures 4.19b, 4.19d, and 4.19f plot the mean firing rate, adaptation level, and phase plane, respectively, when the saturation factor is increased by 75%. Note that the putative $r-$nullcline remains unchanged, but the putative $w-$nullcline does not decrease at high firing rate (r). Thus, there are no fixed points at high activity and no bistability.
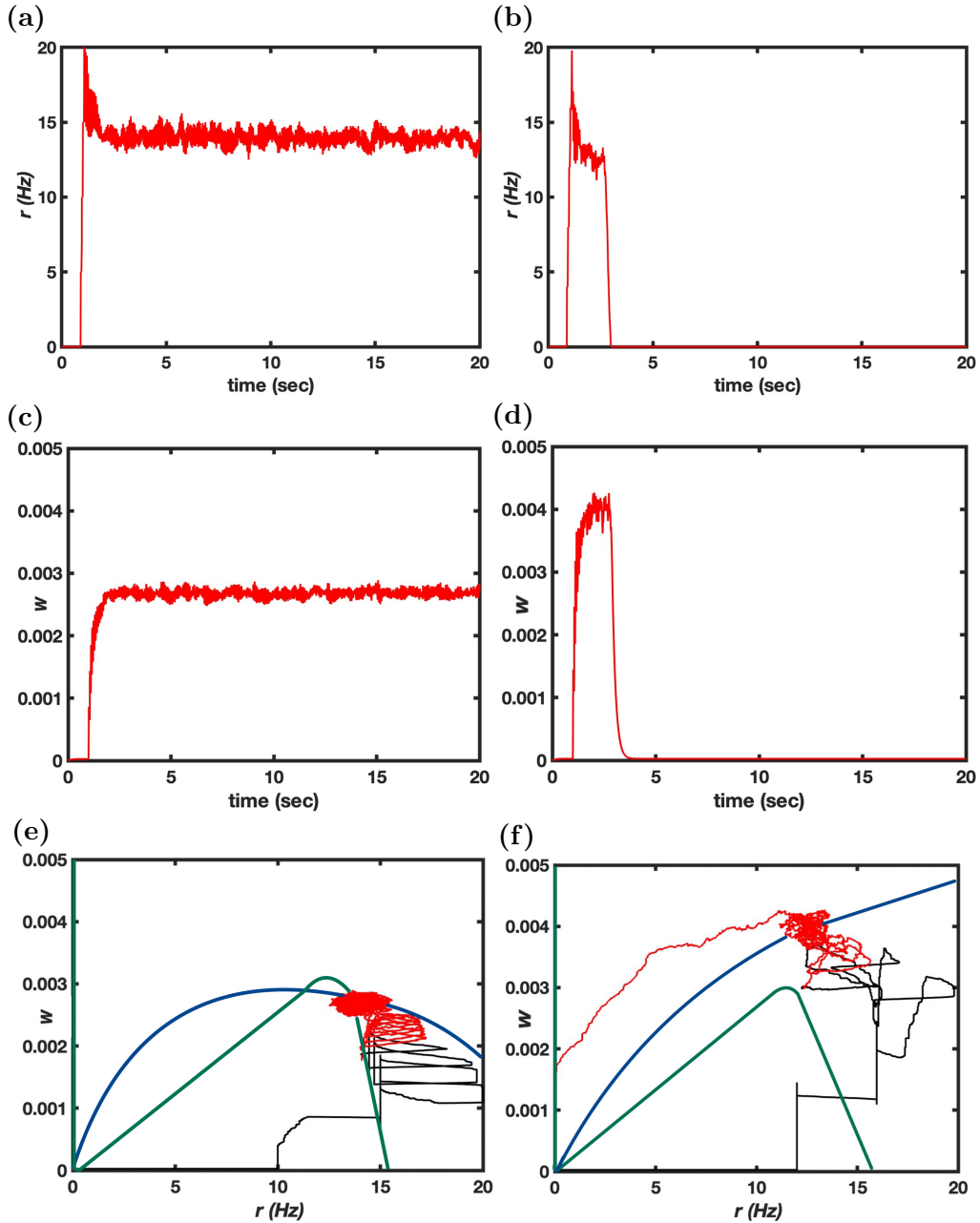
FIGURE 4.19. Firing rate r and adaptation w for a bistable cell-based network model (a)-(c) and (d)-(f) network model with increased superthreshold M-current activation. Increased activation during firing of action potentials inhibits the bistable dynamics. (a),(d) Mean firing rate r of the network model as a function of time. (b),(e) Mean adaptation w as function of time. (c),(f) Mean firing rate and adaptation phase plane. Black curve indicates input is on, red curve indicates input off. Putative r-nullcline in green, and putative w-nullcline in blue based on insight from analysis of firing rate model dynamics, and indicate putative nullclines when there is no input ($I = 0$).

103

4.6. Appendix

4.6.1. Bistable Parameter Set Decreases Parameter Sensitivity. The default firing rate model does not display bistability, but altering the recurrent connection strength and/or the adaptation strength parameters bestows the firing rate model with bistable dynamics. The sensitivity of the firing rate model to parameter alterations can change depending on the parameter set implemented before parameter changes. To show this, parameter values $\alpha = 0.0015$ and $\beta = 2$ are chosen so that the firing rate model displays bistable dynamics. Figure 4.20 plots a bifurcation diagram of this bistable firing rate model in the (I, r) parameter space.
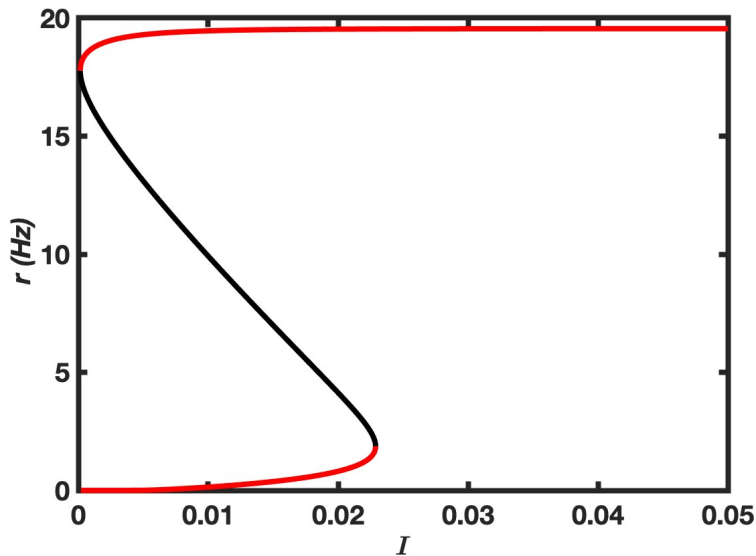

FIGURE 4.20. Bifurcation diagram for firing rate model in a bistable parameter set with $(\alpha, \beta) = 0.0015, 2)$, and I as the control parameter. The remaining parameters are default parameters from table 4.1.

Figure 4.21 plots two bifurcation diagrams in the (α, I) and (β, I) parameter space. The saddle-node bifurcation curves for the default firing rate model are plotted as the solid red curves, and the saddle-node bifurcation curves for the bistable firing rate model with $\alpha = 0.0015$ and $\beta = 2$ are plotted as the dotted red curves. The shape of the bistable region does not change when the parameters are changed, but the bistable region in the parameter spaces are much larger for the altered firing rate model with altered α, β parameter values. This implies that the sensitivity of the firing rate model to changes in recurrent connection strength and adaptation strength decreases when the original parameters implemented for the firing rate model result in bistable dynamics.
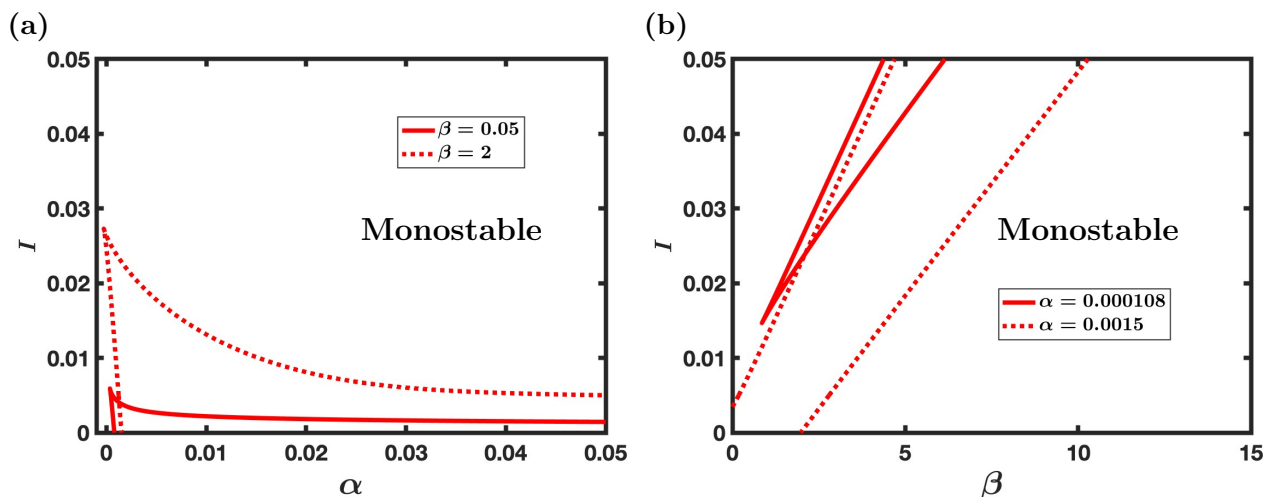

FIGURE 4.21. Two-parameter bifurcation diagram(s) demonstrating how changing a bistable firing rate model has reduce sensitivity of to parameter perturbations. The red curves indicate saddle-node bifurcations with the enclosed area representing bistability. The area outside of the red curves indicate monostability. Remaining parameters not addressed in legend(s) taken from table 4.1.

4.6.2. Non-Monotonicity of Steady-State Adaptation Curve Promotes Robust Bistable Dynamics. In this subsection, analysis of the sensitivity of the bistable firing rate model to changes in the (non-)monotonicity of the steady-state adaptation curve is presented. Figure 4.22 plots a two parameter bifucation diagram in (b, I) parameter space, where the decay parameter b controls the (non-)monotonicity of the adaptation function $w_\infty(r)$ - i.e.

if $b > 0$, then $w_\infty(r)$ is non-monotonic, if $b = 0$, then $w_\infty(r)$ is monotonic with asymptotic limit, and if $b > 0$ then $w_\infty(r)$ is monotonic without a limit. Clearly the bistable model (default parameters from table 4.1 except $\alpha = 0.0015$, $\beta = 2$) expresses bistable dynamics even when the adaptation function $w_\infty(r)$ is monotonic. However, the range of input values I that induce bistable dynamics is reduced significantly when $b \leq 0$. This implies that the non-monotonicity of the adaptation curve/function promotes robust bistable dynamics, i.e. the bistable dynamics are less sensitive to changes in input I when the steady-state adaptation curve is non-monotonic.
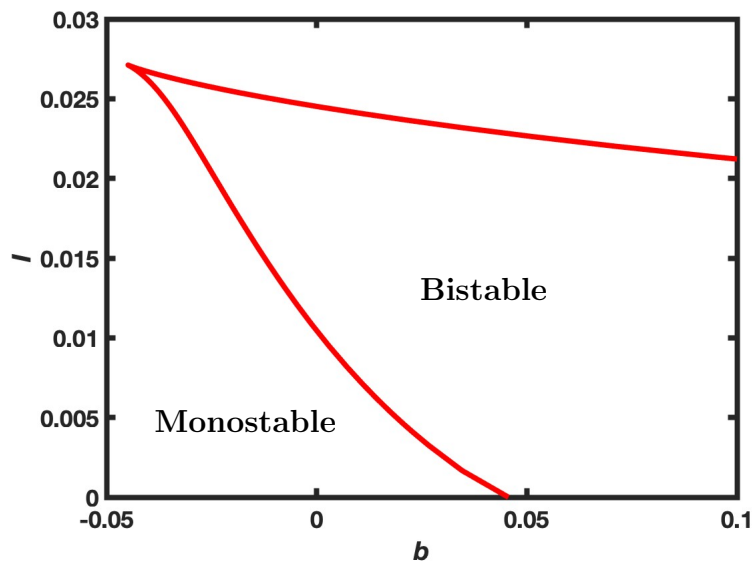

FIGURE 4.22. Two parameter bifurcation diagram for the firing rate model with default parameters except $(\alpha, \beta) = (0.0015, 2)$ implemented with b on the horizontal axis controlling the monotonicity of the steady-state activation curve and I on the vertical axis controlling the strength of input. The largest range of input values which result in bistable dynamics occur when $b > 0$. A decrease in the non-monotonicity of the activation curve is correlated with a decrease in the robustness of bistability in the model with respect to input. Eventually the monotonicity is increased enough that it eliminates any bistable dynamics from the model.

CHAPTER 5

Autonomic Control of Cardiovascular System - Hierarchical Structure of ANS Promotes Local Control

In the previous chapters, we modeled the ICNS only. (Note, however, that our ICNS model is sufficiently general that it can be used to model a general ANS ganglion, including the ITNS.) In this chapter, we incorporate the cell-based and firing rate models of the ANS ganglia developed in chapters 2 and 4 into a holistic model of the autonomic neurocardiovascular control system that includes a hierarchical neural circuit model of the ANS, a phase model of the sinoatrial node (SAN), a mechanical model of the cardiovascular system, and a model describing the baroreflex. In the future, we aim to implement this model to investigate the impact that the hierarchical structure of the ANS has on cardiovascular control, i.e., address the question: What do the ICNS and ITNS contribute to the neurocardivascular control system? This chapter primarily sets up future work, some preliminary results are provided.

5.1. Hierarchical Models of Autonomic Nervous System for Cardiovascular Control

The structure of our ANS network model is based on the anatomical hierarchical neural circuit outlined by by Shivkumar et al. [**24**,**69**] and the corresponding computational models of Kember et al. [**37**, **41**] (see figure 5.1). The neural circuit consists of the sympathetic pathway (SNS) and the parasympathetic pathway (PNS). The SNS comprises three layers (subnetworks): the central nervous system (CNS), the intrathoracic nervous system (ITNS) and the intrinsic cardiac nervous system (ICNS). Efferent pathways connect the CNS to the

ITNS and the ITNS to a subpopulation of neurons in the sympathetic ICNS (i.e., the S-ICNS). Afferent pathways connect the S-ICNS with the ITNS. The PNS comprises two layers (subnetworks): the CNS and a subpopulation of neurons in the parasympathetic intrinsic cardiac nervous system (i.e., the P-ICNS) with efferent connections from the CNS to the P-ICNS. The S-ICNS and the P-ICNS are also interconnected. Note that there is no clear delineation between a sympathetic ICNS and a parasympathetic ICNS, and the S-ICNS and the P-ICNS in the model are extensively connected, effectively forming a single subnetwork.
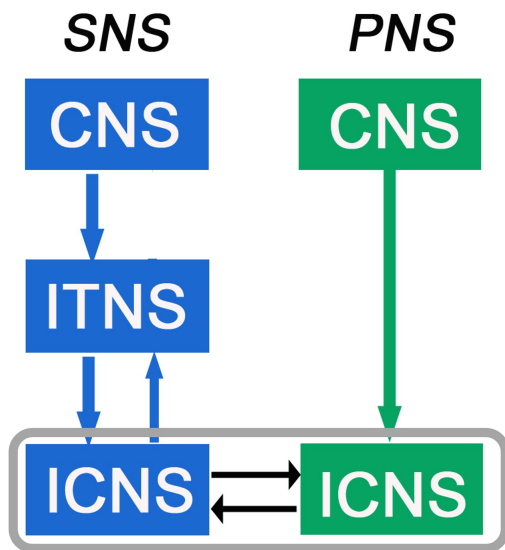

FIGURE 5.1. Schematic showing the network connectivity and structure of the hierarchical network model of the cardioascular autonomic nervous system. Sympathetic nervous system is shown in blue, parasympathetic nervous system is shown in green. The ICNS is not clearly delineated in the model but is shown here to indicate that it is included in both the SNS and PNS models.

5.1.1. Cell-Based Network Model of ANS.

5.1.1.1. *CNS Neuronal Dynamics.* The sympathetic and parasympathetic CNS subnetworks contain 100 model neurons each. Spike times for the individual neurons in the CNS subnetworks are modelled as renewal processes. That is, the firing times of the j-th neuron in the sympathetic and the parasympathetic branches of the CNS are given by Poisson processes with firing rates λ_{SNS} and λ_{PNS} with a post-spike absolute refractory period of t_{ref} [26].

5.1.1.2. *Network Connectivity.* Synaptic dynamics and network connectivity within the ITNS and ICNS subnetworks are as described in chapter 2 sections 2.1.2 and 2.1.3, respectively. The probability of connection between the S-ICNS and P-ICNS neurons is $p_{SP} = p_{PS}$. In the PNS, efferent connections from CNS neurons to P-ICNS neurons occur randomly with probability of connection p_{PNS}. In the SNS, afferent connections from the S-ICNS to the ITNS occur with probability $p_{SNS,aff}$. In the SNS, neurons in the ITNS receive efferent input from CNS neurons with probability $p_{ITNS,eff}$, and S-ICNS neurons receive efferent input from ITNS neurons with probability $p_{ICNS,eff}$. Each neuron in the ITNS that receives efferent input receives it from n+1 random presynaptic neurons in each preceding layer (with $n = 3$), where the n connections are weak, and the 1 connection is strong. This $n + 1$ convergent innervation is observed in both amphibian sympathetic ganglia [81] and mammalian sympathetic ganglia [31, 34, 71]. The random connectivity in the neural circuit inherently generates populations of afferent, efferent and local circuit neurons as described by Shivkumar and colleagues [24, 69]. The model for afferent feedback from the cardiovascular system is inlcuded as described in chapter 2 section 2.1.4 is included: The function describing the times of the presynaptic spikes of input is a scaled version of the left ventricular pressure (LVP). We also include local pressure feedback from atrial stretch receptors [78] (modeled in the same way as LVP feedback) to the sympathetic and parasympathetic subnetworks as $\lambda(t) = \max(0, P_{la,mean} - P_{la})$ and $\lambda(t) = \max(0, P_{la} - P_{la,mean})$, respectively, where P_{la} is left atrial pressure and $P_{la,mean} = 7.26$ mmHg is the mean value of P_{la} during "resting" conditions. These functions are scaled so the expected number of pre-synaptic input spikes per cardiac cycle is equal to that of the LVP afferent feedback. Note that the two afferent feedbacks add linearly.

5.1.2. Firing Rate Model of ANS. We also construct a neurocardiovascular control model incoporating the firing rate model derived in chapter 4 for each subnetwork (ITNS and ICNS) with the framework of the firing rate extended to include the connections between the ITNS and ICNS subnetworks shown in figure 5.2.
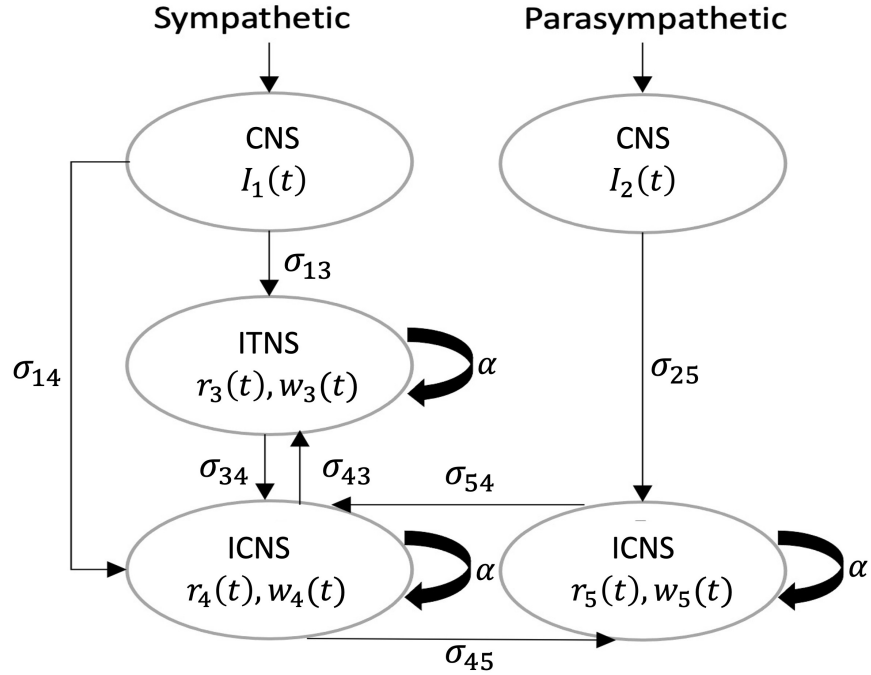
FIGURE 5.2. Schematic of the firing rate model of the ANS. The structure of the model is the same as the structure of the cell-based network model of the ANS, but each subnetwork is represented by a firing rate model..

The equations for the firing rate model of the ANS are

$$\tau_r \frac{dr_3}{dt} = -r_3 + f(\sigma_{13}I_1 + \alpha r_3 - \beta w_3 + \sigma_{43}r_4)$$

$$\tau_w \frac{dw_3}{dt} = -w_3 + w_\infty(r_3)$$

$$\tau_r \frac{dr_4}{dt} = -r_4 + f(\sigma_{14}I_1 + \alpha r_4 - \beta w_4 + \sigma_{34}r_3 + \sigma_{54}r_5)$$

$$\tau_w \frac{dw_4}{dt} = -w_4 + w_\infty(r_4)$$

$$\tau_r \frac{dr_5}{dt} = -r_5 + f(\sigma_{25}I_2 + \alpha r_5 - \beta w_5 + \sigma_{45}r_4)$$

$$\tau_w \frac{dw_5}{dt} = -w_5 + w_\infty(r_5)$$

where I_k is the activity of the sympathetic ($k = 1$) CNS and the parasympathetic ($k = 2$) CNS. r_j is the firing-rate of the j-th layer, w_j is the adaptation due to the M-current in the j-th layer, σ_{jk} is the connection strength of the input from layer j into layer k, α is the

110

recurrent connection strengh of layer j, β is the adaptation strength of layer j for $j = 3, 4, 5$. The parameters for f and w_∞ are given in table 4.1 of chapter 4.

We assume that sympathetic and parasympathetic CNS activity is modeled by a single renewal process, I_1 and I_2, respectively. To model the reduced central signals that the ICNS subnetworks receive directly compared to those the ITNS subnetwork receive directly [37], we set $\sigma_{14} = \sigma_{25} = \frac{3}{4}\sigma_{13} = \frac{3}{4}$. The connection strength parameters σ_{34}, σ_{43}, σ_{45} and σ_{54} were chosen to match some basic quantitative behaviors of the cell-based ANS model. The homogenous construction of the parasympathetic and sympathetic ICNS along with the equal probabilities of connections between the S-ICNS and P-ICNS (p_{SP}) implies that $\sigma_{45} = \sigma_{54}$. The connection strength parameters $\sigma_{13}, \sigma_{25} = 1$ were chosen to reflect the input modeling choices in chapter 2. The σ_{jk}, α, and β parameters are provided in Table 5.1.

Parameter	Value
α	0.000108
β	0.05
σ_{13}	1
σ_{14}	0.75
σ_{25}	1
σ_{34}	0.00008
σ_{43}	0.00005
σ_{45}	0.000075
σ_{54}	0.000075

TABLE 5.1. Parameters for firing rate model of ANS. Note that the parameters σ_{13} and σ_{25} are equal to 1 to match with modeling choices of input from chapter 2 and α, β values taken from chapter 4.

5.2. Phase Model of Sinoatrial Node with Neural Input

The SAN acts as a pacemaker for the heart, setting the heart rate. For simplicity, a phase model is used to describe the phase of the SAN dynamics in a similar manner to previous work [60,77,78], however we explicitly use a phase-response curve (PRC) to capture the dependence of the timing of neural input on the phase of the SAN, that is, the dynamics

are given by

$$\frac{d\theta}{dt} = \omega + Z(\theta)I(t),$$

where θ is the phase of the SAN between 0 and 1, $\omega = 1/833$ msec^{-1} (72 bpm) is the intrinsic frequency of the SAN [**60**, **77**], $Z(\theta) = 1 - \cos(2\pi\theta)$ is the PRC that determines to what extent the neural input speeds up or slows down the heart rate and depends on the phase of the SAN, and $I(t)$ describes the neural input to the SAN.

For this model, the neural input originates from the neurotransmitters released by ANS neurons onto the SAN. The two main neurotransmitters are Acetylcholine (ACh) and Norepinephrine (NE), released by parasympathetic and sympathetic neurons, respectively [**37**, **69**, **78**]. NE binds to β-adrenergic receptors (βAR channels) on the SAN and induces a slow (~ 10 s) excitatory response, while ACh binds to muscarinic receptors (KACh channels) on the SAN and induces a fast (beat-to-beat) inhibitory response, speeding up and slowing down the rate of change of SAN activity, respectively. Therefore, the neural input to the SAN is given by

$$I(t) = I_{\beta_{AR}}(t) - I_{KACh}(t).$$

The current that is rapidly induced by activation of the KACh channels is

$$I_{KACh} = G_{KACh}\frac{\alpha(ACh)}{\alpha(ACh) + 9.96},$$

where

$$\alpha(ACh) = \frac{12.32ACh}{ACh + 4.2 \cdot 10^{-6}}$$

with G_{KACh} representing the drive coefficient (as in [**59**]). The current induced by activation of βAR channels is

$$I_{\beta_{AR}} = G_{\beta_{AR}}\beta_{AR},$$

with

$$\tau_{\beta_{AR}}\frac{d\beta_{AR}}{dt} = -\beta_{AR} + \beta_{AR,max}\frac{NE^2}{K_{NE}^2 + NE^2}$$

112

where $G_{\beta AR}$ is the drive coefficient, $\tau_{\beta AR}$ is the time constant of βAR activation, $\beta_{AR,max}$ is the maximum βAR activation, and K_{NE} produces the half maximum response (as in [55]).

Figure 5.3 plots an example of the voltage of the SAN v, the phase of the SAN θ, and the value of the PRC as a function of the phase of the SAN $Z(\theta)$ with no neural input ($I(t) = 0$). Figure 5.4 shows a surface plot of the combined effects of sympathetic activity (NE) and parasympathetic activity (ACh) on heart rate set by the SAN model in steady-state. Parameters of the SAN model are given in table 5.2.
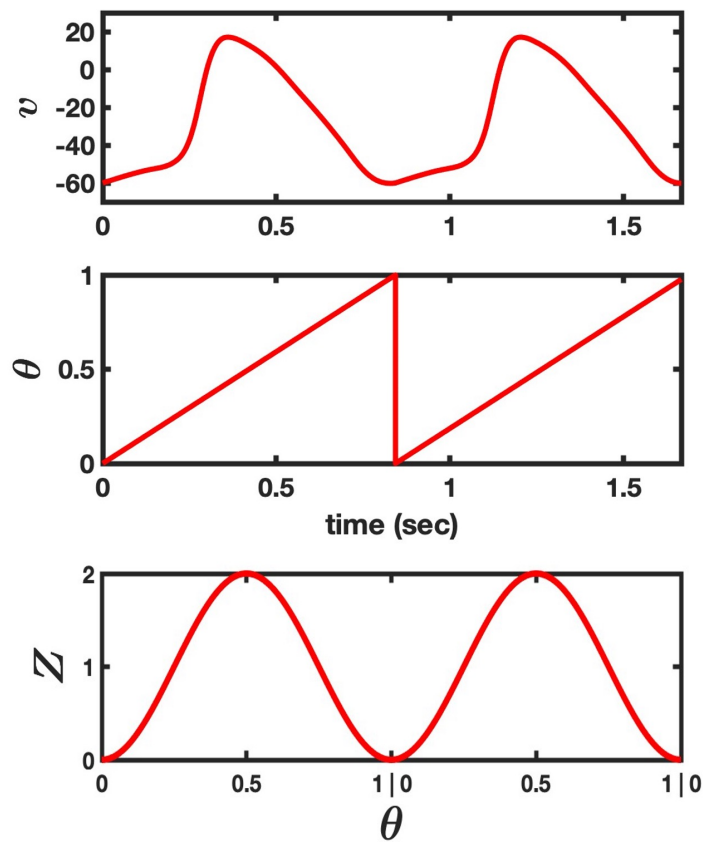

FIGURE 5.3. Membrane potential v, phase θ, and phase response curve Z of the phase model of the sinoatrial node with no neural input. The SAN model evolves with an intrinsic frequency $\omega = 1/833$ msec^{-1} that remains unchanged without neural input from the ANS.
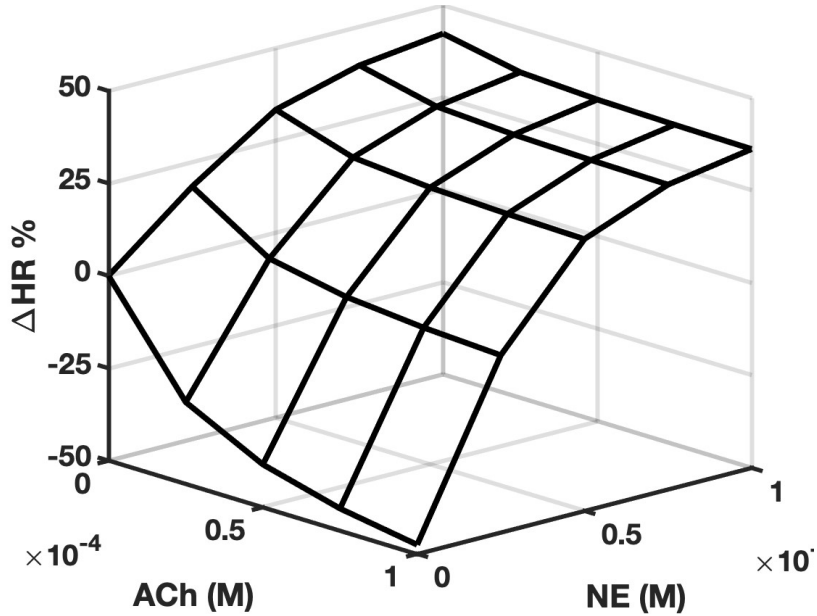
FIGURE 5.4. Steady-state response of heart rate induced by constant ACh and NE binding values input to SAN model illustrating how the KACh and βAR induced drive combine to control SAN beat frqeuency.

Parameter	Value
G_{KACh}	10^{-3} msec^{-1}
$G_{\beta_{AR}}$	10^{-3} msec^{-1}
$\tau_{\beta_{AR}}$	10^4 msec
$\beta_{AR,max}$	0.8
K_{NE}	1500 M

TABLE 5.2. Table of parameter values used for phase model of sinoatrial node. βAR parameters taken to approximate previous values [**55**].

5.3. Mechanical Model of Heart and Vasculature

The cardiovascular system is a combination of the heart and the vascular system's vast network of veins, arteries, and arterioles that extend throughout the body. The mechanical portion of the neurocardiovascular control model describes the contractions of the heart and the flow of blood through the cardiovascular system. To model the mechanical aspects of the cardiovascular system, a modified version of the idealized Ursino et al. mechanical model [**60**, **77**] is implemented. Figure 5.5 shows a schematic of the cardiovascular model. The model can be subdivided into a cardiac portion and a vascular portion, consisting of 4

cardiac compartments (left and right, atrial and ventricular) and 8 vascular compartments for the pulmonary and systemic arteries and veins. The state of each cardiac compartment x is described by pressure P_x and volume V_x, with compliance C_x and resistance R_x parameters, and blood flow between compartments F_{xy}. The left and right ventricular compartments also have an elastance state variable $E_{max,x}$. The state of each vascular compartment x is described by pressure P_x, with compliance C_x and resistance R_x parameters. The systemic and pulmonary arterial compartments also have a state variable F_x describing the outward blood flow.
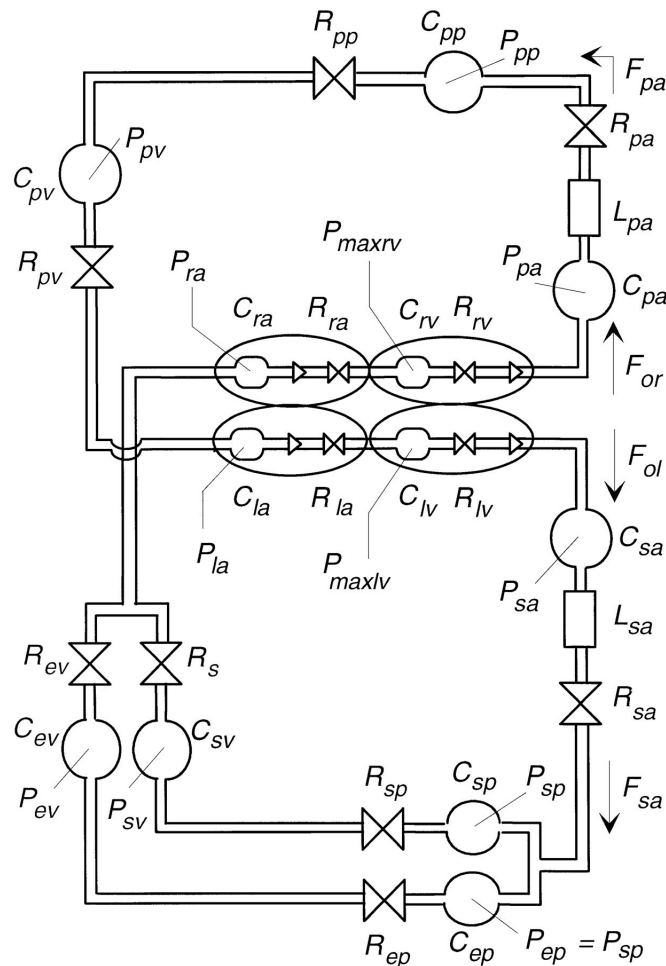

FIGURE 5.5. Schematic of the mechanical portion of the cardiovascular model. The four compartments of the heart, pulmonary arteries, peripheral systems, pulmonary veins, systemic arteries, splanchnic and extrasplanchnic periphery and veins. Figure from Ursino 1998 [**77**].

115

5.3.1. Mechanical Vasculature model. The vasculature model is split into two parts - the pulmonary and systemic. The pulmonary model describes the flow of oxygen depleted blood being pumped into the lungs, oxygenating, and pumping back to the left atrium. The systemic model describes the flow of oxygenated blood being pumped through the body, and the deoxygenated blood returning to the right atrium. The vasculature model uses a set of pressure, capacitance, inertance, and resistance relationships to model activity of each compartment and the flow between them (schematic shown in figure 5.5). The pressure and blood flow of the systemic and pulmonary arteries (of compartment x into compartment y) are given by

$$C_x \frac{dP_x}{dt} = F_{in} - F_x$$

$$L_x \frac{dF_x}{dt} = P_x - P_y - R_x F_x$$

where F_{in} is the inward blood flow, F_x is the outward blood flow, P_x is the pressure R_x is the resistance, C_x is the capacitance, L_x is the inertance, and P_y is the pressure of the following compartment.

The structure of the pressure variables for the remaining vascular compartment(s) x is given by

$$C_x \frac{dP_x}{dt} = F_{in,x} - F_{out,x}$$

where C_x is the capacitance, P_x is the pressure, $F_{in,x}$ is the blood flow into the compartment, and $F_{out,x}$ is the blood flow out of the compartment. Blood flow has the form $F_{in/out,x} = \frac{P_1 - P_2}{R}$.

5.3.2. Mechanical Cardiac Model. The cardiac model is comprised of 4 compartments representing the left atrium, left ventricle, right atrium, and right ventricle. The pressure gradient $(P_{pv} - P_{la})$ between the pulmonary veins and the left atrium drives blood into the left atrium, where P_{pv} is pulmonary venous pressure and P_{la} is left atrial pressure.

The blood flow from the left atrium into the left ventricle is given by

$$
F_{il} = \begin{cases} 0 & \text{if } P_{la} \le P_{lv} \\ \frac{P_{la} - P_{lv}}{R_{la}} & \text{if } P_{la} > P_{lv} \end{cases},
$$

and eft atrial pressure is modeled by

$$
C_{la} \frac{dP_{la}}{dt} = \frac{P_{pv} - P_{la}}{R_{pv}} - F_{il}
$$

where C_{la} is the compliance of the left atrium and R_{pv} is pulmonary venous resistance. Note that left atrial volume V_{la} is directly determined by P_{la}.

The left ventricle receives blood flow from the left atrium (F_{il}), and pumps to induce blood fow outwardly to the systemic arteries (F_{ol}). The left ventricular volume V_{lv}, and blood flow out of left ventricle F_{ol} are given by

$$
\frac{dV_{lv}}{dt} = F_{il} - F_{ol}
$$

$$
F_{ol} = \begin{cases} 0 & \text{if } P_{sa} \ge P_{max,lv} \\ \frac{P_{max,lv} - P_{sa}}{R_{lv}} & \text{if } P_{sa} < P_{max,lv} \end{cases}
$$

where systemic arterial pressure P_{sa}, left ventricular isometric pressure $P_{max,lv}$, and left ventricular pressure P_{lv} are given by

$$
C_{sa} \frac{dP_{sa}}{dt} = F_{ol} - F_{sa}
$$

$$
P_{max,lv} = \phi(t) E_{max,lv}(V_{lv} - V_{u,lv}) + (1 - \phi(t)) P_{0,lv}(\exp(k_{E,lv} V_{lv}) - 1)
$$

$$
P_{lv} = P_{max,lv} - R_{lv} F_{ol}
$$

where

$$
\phi(t) = \begin{cases} \sin^2(\pi T \theta / T_{sys}) & \text{if } 0 \le \theta \le T_{sys}/T \\ 0 & \text{else} \end{cases}
$$

117

models the contraction of the left ventricle, θ is the phase of the SAN, T is the heart period, T_{sys} is the duration of systole, $V_{u,lv}$ is the unstressed volume of the left ventricle, $P_{0,lv}$ and $k_{E,lv}$ are constant parameters that describe the left ventricular pressure/volume relationship at diastole, and $E_{max,lv}$ is the left ventricular elastance at maximum contraction given by $E_{max,lv} = E_{max,lv0} + G_{E,lv}F(\beta_{AR})$, where $G_{E,lv}$ is gain, $E_{max,lv0}$ is left ventricular elastance with no neural input, and F is a threshold-logarithmic function of the level of βAR activation.

The structure of the right atrium and ventricle model is similar to the left. Parameters for mechanical model of cardiovascular system taken from [60, 77], however, total blood volume is set to $V_t = 4300$ ml so output of cardiovascular model at "resting" conditions shown in figure 5.6 matches Ursino 1998 figure 2 [77].
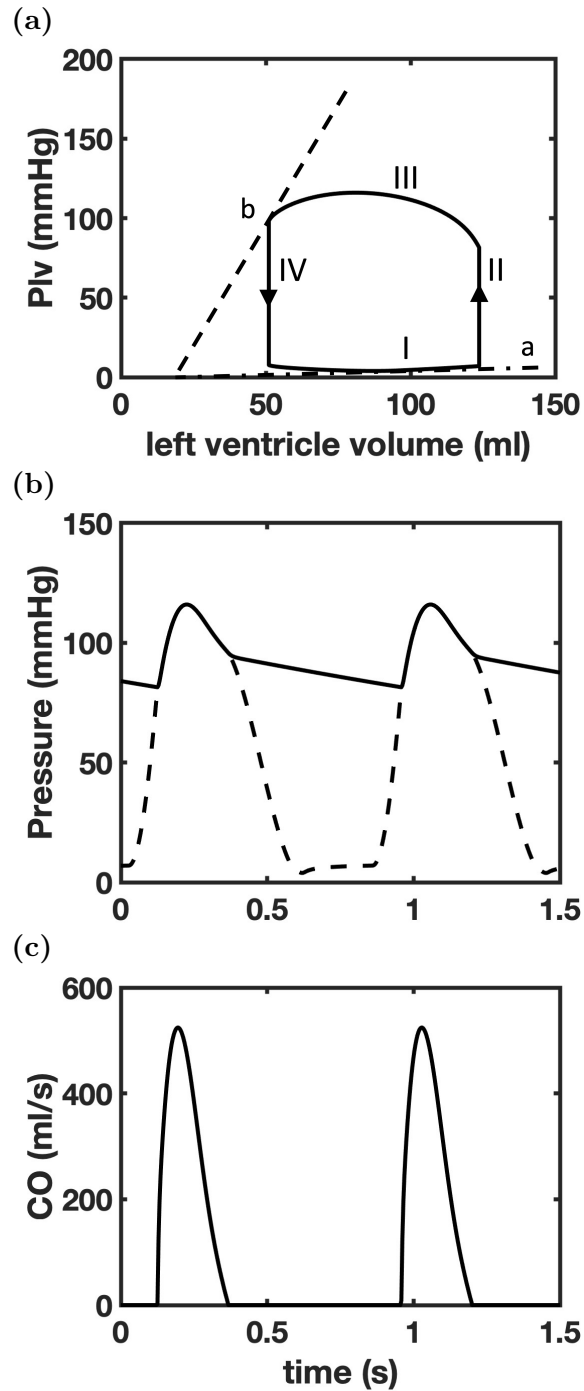
FIGURE 5.6. Pressure, volume, and cardiac output of mechanical cardiovascular model with no neural input. (a) Pressure-volume curve of left ventricle. (b) Systemic arterial pressure in solid curve, left ventricular pressure in dashed curve. (c) Cardiac output. Total blood volume V_t chosen so pressure-volume, pressure, and cardiac output data matched with figure 2 in Ursino 1998 [77].

5.4. Baroreceptor Model

As the heart pumps blood throughout the body, information about the blood pressure in the arteries is relayed to the brainstem via the Baroreceptor Reflex (Baroreflex). Pressure sensitive neurons (stretch receptors) located primarily in the carotid sinus and aortic arch sense the changes in pressure on the arterial walls induced by blood flow. This information about blood pressure is transduced into neural signals and carried via afferent neurons to the brainstem. The brainstem processes these neural signals and relays commands through the sympathetic and parasympathetic nervous systems in order to exert control of the heart rate and contractility. The baroreflex closes the largest neurocardiovascular feedback loop, allowing the ANS to accomodate changes in pressure and bring the cardiovascular system to homeostasis.

5.4.1. Model Description. To describe the baroreceptor system, we adapt the Madhi et al. 2013 baroreflex model [**49**], which is a three component model consisting of arterial wall deformation, baroreceptor stimulation, and baroreceptor firing rate. The arterial walls deform as the pressure within the carotid sinus and aortic arch change. The baroreceptor neurons originating in these vessels transduce the wall deformation into an action potential firing rate [**49**].

The arterial wall deformation model assumes that the pressure-area relationship of an elastic vessel (arteries) is nonlinear, with input pressure p and output wall strain ϵ_w (which is shown in figure 5.7)

$$\epsilon_w = 1 - \sqrt{\frac{A_0(\alpha^k + p_{sa}^k)}{A_0\alpha^k + A_m p_{sa}^k}},$$

where A_0 and A_m (mm^2) are the unstressed and maximal cross-sectional area, respectively, α (mmHg) is the characteristic pressure at which the vessel begins to saturate, and k determines the steepness of the sigmoidal pressure-area relationship given by

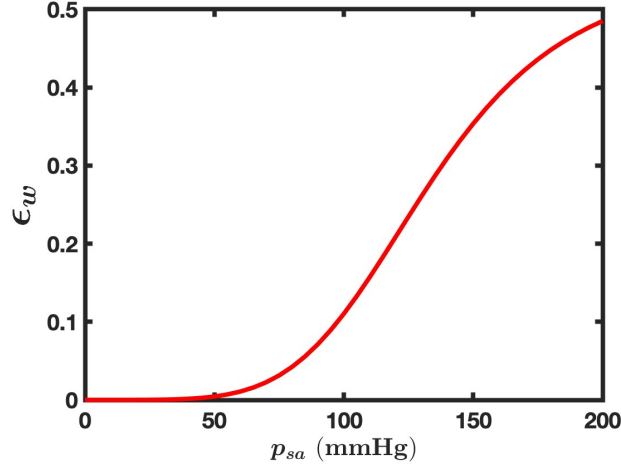$$A(p) = (A_m - A_0)\frac{p^k}{\alpha^k + p^k} + A_0.$$

FIGURE 5.7. Arterial wall strain ϵ_w as a function of systemic arterial pressure p_{sa}. Parameters given in table 5.3.

The baroreceptor model assumes that the strain at the nerve endings is a direct result of the arterial wall strain, and that this strain can be modeled by a series of Voigt bodies (dampers and springs in parallel). Specifically, the mechanoreceptive strain model includes 2 Voigt bodies attached to a wall with a spring on the terminal side. The model of the arterial wall strain is

$$\frac{d\epsilon_1}{dt} = -(\alpha_1 + \alpha_2 + \beta_1)\epsilon_1 + (\beta_1 - \beta_2)\epsilon_2 + (\alpha_1 + \alpha_2)\epsilon_w$$

$$\frac{d\epsilon_2}{dt} = -\alpha_2\epsilon_1 - \beta_2\epsilon_2 + \alpha_2\epsilon_w.$$

where ϵ_1 and ϵ_2 are the strains on the 1st and 2nd Voigt bodies, and α_i and β_i are spring constants. The strain sensed by the baroreceptors ϵ_{ne} is then given by

$$\epsilon_{ne} = \epsilon_w - \epsilon_1(\epsilon_w).$$

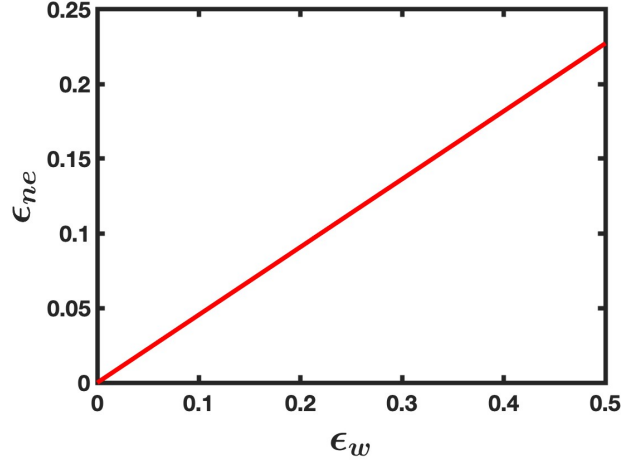The steady-state strain sensed by the baroreceptors ϵ_{ne}^∞ is shown in figure 5.8.

FIGURE 5.8. Steady-state mechanoreceptor sensed strain ϵ_{ne}^{∞} as a function of arterial wall strain
$epsilon_w$. Parameters given in table 5.3.

The baroreceptor firing activity is given by the steady-state firing rate of a leaky integrate-and-fire neuron given by

$$f = (T + \tau_{ref})^{-1} = \begin{cases} 0 & \text{if } I_{ne} \leq g_L V_{thresh} \\ \dfrac{1}{-\frac{C}{g_L} \log\left(\frac{I_{ne} - g_L V_{thresh}}{I_{ne}}\right) + \tau_{ref}} & \text{if } I_{ne} > g_L V_{thresh}. \end{cases}$$

where C is capacitance, g_L is leakage conductance, V_{thresh} is the threshold for a spike, τ_{ref} is refractory period, and $I_{ne} = s_1 \epsilon_{ne} + s_2$ is the input current that depnds on the strain sensed by the baroreceptor. Figure 5.9 plots the steady-state firing rate of the baroreceptors as a function of the sensed strain. The parameters in Table 5.3 were chosen so that the baroreceptor model output shown in figure 5.10 would qualitatively match Madhi et al. figure 10 [**49**].
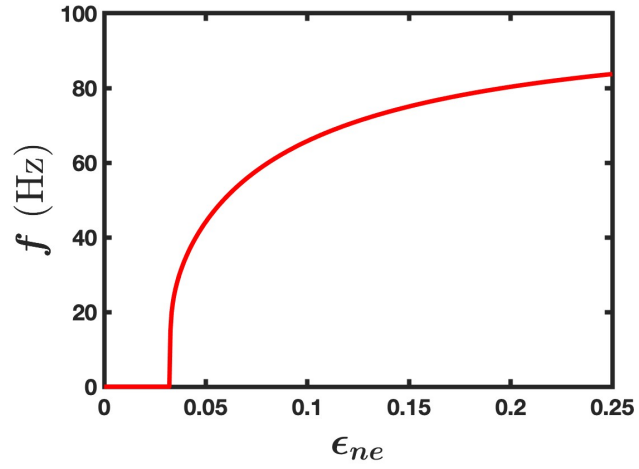
FIGURE 5.9. Firing-rate of the baroreflex f as a function of the baroreceptor sensed strain ϵ_{ne}.

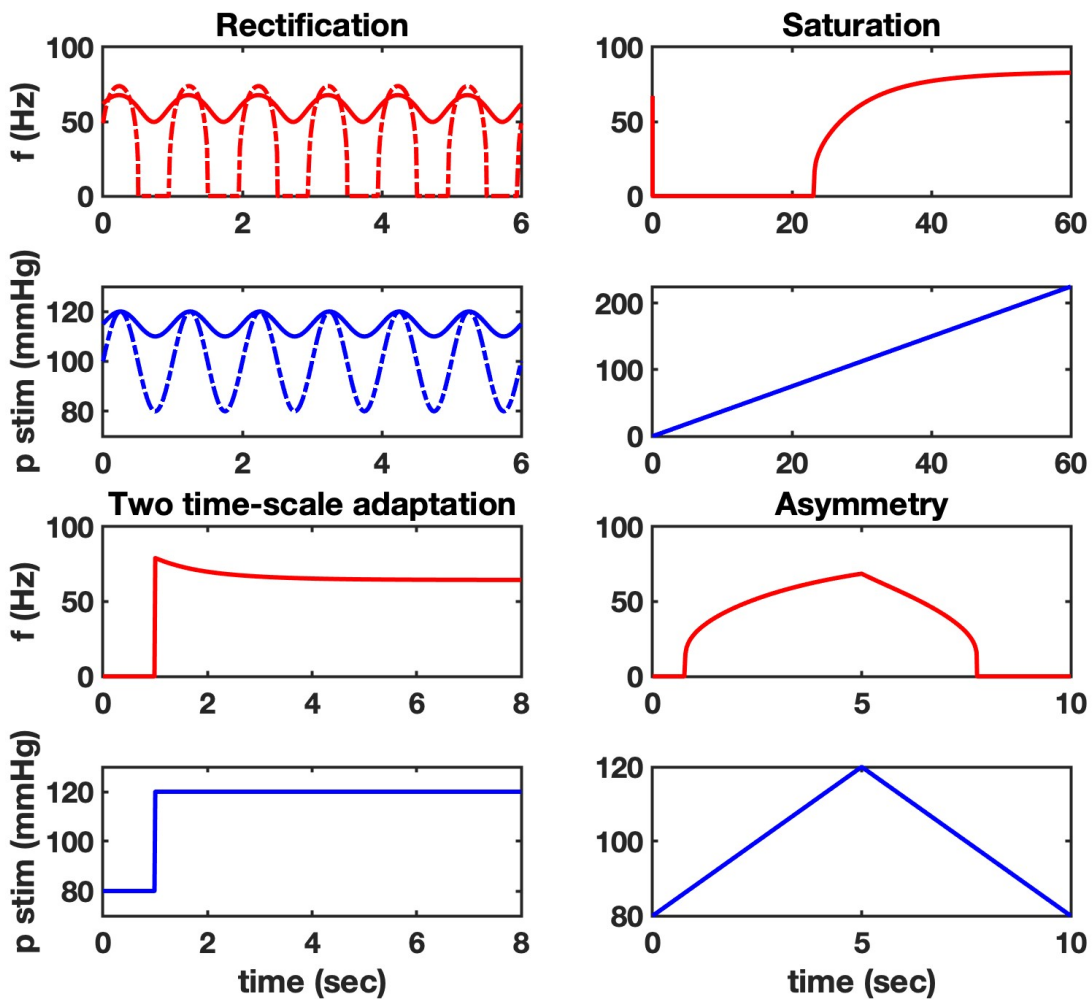FIGURE 5.10. Qualitative response of the baroreflex model (red) to sinusoidal, ramp, step, and triangular pressure inputs (blue). Baroreflex model elicits similar qualitative responses to Mahdi et al. 2013, figure 10 [49]. Pressure input ranges altered to reflect the systemic arterial pressure ranges in cardiovascular model shown in figure 5.6, and baroreflex parameters tuned to elicit similar qualitative response.

Parameter	Value
A_0	π mm^2
A_m	5π mm^2
α	180 mmHg
k	5
α_1	0.4 s^{-1}
α_2	0.5 s^{-1}
β_1	0.5 s^{-1}
β_2	2 s^{-1}
s_1	100 pA
s_2	0 pA
g_L	0.4 μS
C	3.75 nF
V_{thresh}	12.5 mV
t_{ref}	0.01 s

TABLE 5.3. Paramters used in the Baroreflex model. Original values from Madhi et al. 2013 [49] adapted to use with current cardiovascular model described in previous section.

5.5. Preliminary Results: Effect of ITNS and ICNS on Heart Rate and Heart Rate Variability

In this section, we present preliminary results for three different models of the ANS in the autonomic neurocardiovascular control system: a cell-based hierarchical model of the ANS, a firing rate hierarchical model of the ANS, and a classical model of the ANS, in which the ITNS and ICNS are omitted from the model, i.e., the only neural signals to the heart and vasculature are directly from the brainstem and spinal cord (CNS). In doing so, we show how the ITNS and ICNS contribute to adaptation of the cardiovascular system to trauma. In our simulation of the neurocardiovascular control model, a 5% loss of total blood volume was induced at time $t = 120$ msec. Figure 5.11 plots the length of the cardiac cycle versus the cycle number for each of the three models of cardiovascular control. The cell-based and firing rate models of cardiovascular control exhibit $\sim 10\%$ increase in heart rate whereas the classical model of autonomic cardiovascular control produced an attenuated response of $\sim 2.5\%$ increase in heart rate. The attenuated response of the classical model is likely due to the lack of local pressure feedback driving the ITNS and ICNS to increase sympathetic input to the heart while decreasing parasympathetic input. This implies that the structure of the ANS, i.e., the ITNS and ICNS, contribute to control of heart rate . Note that the cell-based model displays higher HRV both before and after the increased blood demand. Furthermore, it appears that the hierarchical structure of the ANS possibly enables quicker response by the heart to sudden blood loss.
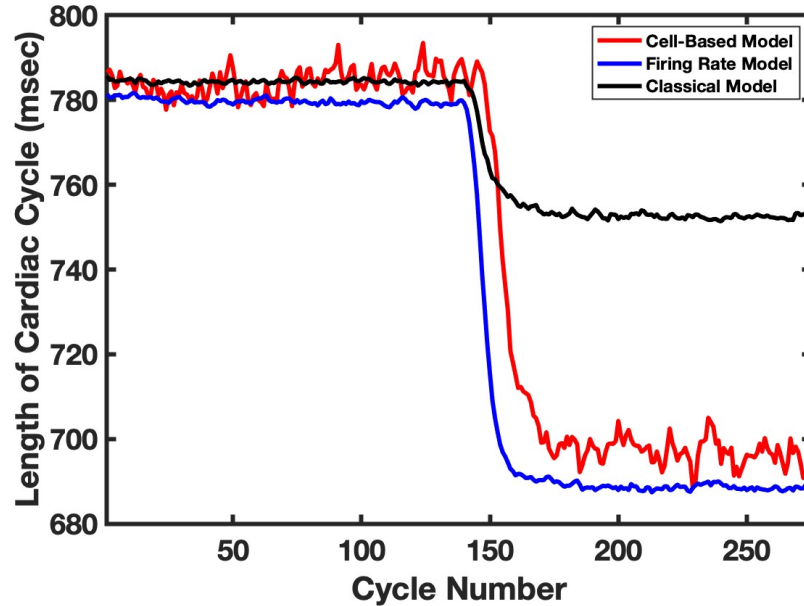
FIGURE 5.11. Length of cardiac cycle versus the cycle number. The ITNS and ICNS regulate heart rate – cell-based and firing rate model of autonomic cardiovascular control system increase heart rate response to traumatic blood loss versus attenuated response of classical model of autonomic neurocardiovascular control. 5% loss of total blood volume induced at 120 seconds of simulated time. The model was simulated for 240 seconds with the first 30 seconds removed to account for transience.

Extensive future work must be done to further our understanding of the effect of the ITNS and ICNS on neurocardiovascular control. We aim to investigate the effect of the ITNS and ICNS on HRV during "resting" conditions and in response to trauma such as sudden blood loss. We also aim to investigate the role of the ITNS and ICNS in ANS response to cardiac arrythmias, myocardial infarctions, and cardiovascular diseases. Furthermore, stimulating peripheral activity to relieve conditions (SPARC) is a current research topic of interest [83] - this model can potentially be used to predict the therapeutic uses of stimulating various subnetworks of the ANS.

Bibliography

[1] Adams, P. R., Brown, D. A., & Constanti, A. (1982). Mcurrents and other potassium currents in bullfrog sympathetic neurones. The Journal of Physiology, 330(1), 537-572.

[2] Adams, P. R., Brown, D. A., & Constanti, A. (1982). Pharmacological inhibition of the Mcurrent. The Journal of Physiology, 332(1), 223-262.

[3] Ardell, J. L., Andresen, M. C., Armour, J. A., Billman, G. E., Chen, P. S., Foreman, R. D., ... & Zucker, I. H. (2016). Translational neurocardiology: preclinical models and cardioneural integrative aspects. The Journal of physiology, 594(14), 3877-3909.

[4] Ardell JL, Andresen MC, Armour JA, Billman GE, Chen PS, Foreman RD, Herring N, OLeary DS, Sabbah HN, Schultz HD, Sunagawa K, Zucker IH (2016). Translational neurocardiology: preclinical models and cardioneural integrative aspects. J Physiol 591(14): 3877- 3909.

[5] Ardell, J. L., Butler, C. K., Smith, F. M., Hopkins, D. A., & Armour, J. A. (1991). Activity of in vivo atrial and ventricular neurons in chronically decentralized canine hearts. American Journal of Physiology-Heart and Circulatory Physiology, 260(3), H713-H721.

[6] Armour, J. A., & Ardell, J. L. (Eds.). (2004). Basic and clinical neurocardiology. Oxford University Press.

[7] Armour, J. A., Collier, K., Kember, G., & Ardell, J. L. (1998). Differential selectivity of cardiac neurons in separate intrathoracic autonomic ganglia. American Journal of Physiology-Regulatory, Integrative and Comparative Physiology, 274(4), R939-R949.

[8] Augustin, M., Ladenbauer, J., Baumann, F., & Obermayer, K. (2017). Low-dimensional spike rate models derived from networks of adaptive integrate-and-fire neurons: comparison and implementation. PLoS computational biology, 13(6), e1005545.

[9] Beaumont, E., Salavatian, S., Southerland, E. M., Vinet, A., Jacquemet, V., Armour, J. A., & Ardell, J. L. (2013). Network interactions within the canine intrinsic cardiac nervous system: implications for reflex control of regional cardiac function. The Journal of physiology, 591(18), 4515-4533.

[10] Boron W, Boulpaep. 2012. Medical Physiology. 2nd ed. Philadelphia: Elsevier Inc. Chapter 14, Autonomic Nervous System.

[11] Brown, A. M., Saum, W. R., & Tuley, F. H. (1976). A comparison of aortic baroreceptor discharge in normotensive and spontaneously hypertensive rats. Circulation research, 39(4), 488-496.

[12] Brown A. M., Saum WR, Yasui S (1978) Baroreceptor dynamics and their relationship to afferent fiber type and hypertension. Circ Res 42: 694702.

[13] Brown, A. M. (1980). Receptors under pressure. An update on baroreceptors. Circulation research, 46(1), 1-10.

[14] Brown, D., Adams, P. (1980). Muscarinic suppression of a novel voltage-sensitive K+ current in a vertebrate neurone. Nature, 283(5748), 673-676.

[15] Brunel, N. (2000). Dynamics of sparsely connected networks of excitatory and inhibitory spiking neurons. Journal of computational neuroscience, 8, 183-208.

[16] Brunel, N., Hakim, V., & Richardson, M. J. (2014). Single neuron dynamics and computation. Current opinion in neurobiology, 25, 149-155.

[17] Constanti, A., & Brown, D. A. (1981). M-currents in voltage-clamped mammalian sympathetic neurones. Neuroscience letters, 24(3), 289-294.

[18] Costanzo, L. S. (2009). Physiology, E-Book. Elsevier Health Sciences.

[19] Connelly, W. M., Laing, M., Errington, A. C., & Crunelli, V. (2016). The thalamus as a low pass filter: filtering at the cellular level does not equate with filtering at the network level. Frontiers in neural circuits, 9, 89.

[20] Cruikshank, S. J., Lewis, T. J., & Connors, B. W. (2007). Synaptic basis for intense thalamocortical activation of feedforward inhibitory cells in neocortex. Nature neuroscience, 10(4), 462-468.

[21] Cuevas, J., Harper, A. A., Trequattrini, C., & Adams, D. J. (1997). Passive and active membrane properties of isolated rat intracardiac neurons: regulation by H-and M-currents. Journal of Neurophysiology, 78(4), 1890-1902.

[22] Davis, H., Herring, N., & Paterson, D. J. (2020). Downregulation of M current is coupled to membrane excitability in sympathetic neurons before the onset of hypertension. Hypertension, 76(6), 1915-1923.

[23] Fortune, E. S., & Rose, G. J. (1997). Passive and active membrane properties contribute to the temporal filtering properties of midbrain neurons in vivo. Journal of Neuroscience, 17(10), 3815-3825.

[24] Fukuda, K., Kanazawa, H., Aizawa, Y., Ardell, J. L., & Shivkumar, K. (2015). Cardiac innervation and sudden cardiac death. Circulation research, 116(12), 2005-2019.

[25] Geisler, C. D., & Goldberg, J. M. (1966). A stochastic model of the repetitive activity of neurons. Biophysical journal, 6(1), 53-69.

[26] Gerstner, W., & Kistler, W. M. (2002). Spiking neuron models: Single neurons, populations, plasticity. Cambridge university press.

[27] Hall, J. E., & Hall, M. E. (2020). Guyton and Hall Textbook of Medical Physiology E-Book: Guyton and Hall Textbook of Medical Physiology E-Book. Elsevier Health Sciences.

[28] Hammer, P. E., & Saul, J. P. (2005). Resonance in a mathematical model of baroreflex control: arterial blood pressure waves accompanying postural stress. American Journal of Physiology-Regulatory, Integrative and Comparative Physiology, 288(6), R1637-R1648

[29] Haken, H. (2008). The NeuronBuilding Block of the Brain. Brain Dynamics: An Introduction to Models and Simualtions, 9-16.

[30] Hernandez, C. C., Zaika, O., Tolstykh, G. P., & Shapiro, M. S. (2008). Regulation of neural KCNQ channels: signalling pathways, structural motifs and functional implications. The Journal of physiology, 586(7), 1811-1821.

[31] Hirst, G. D., & McLachlan, E. M. (1986). Development of dendritic calcium currents in ganglion cells of the rat lower lumbar sympathetic chain. The Journal of physiology, 377(1), 349-368.

[32] Holmes, M. H. (2012). Introduction to perturbation methods (Vol. 20). Springer Science & Business Media.

[33] Huang, M. H., Smith, F. M., & Armour, J. A. (1993). Modulation of in situ canine intrinsic cardiac neuronal activity by nicotinic, muscarinic, and beta-adrenergic agonists. American Journal of Physiology-Regulatory, Integrative and Comparative Physiology, 265(3), R659-R669.

[34] Janig, W., & McLachlan, E. M. (1992). Characteristics of function-specific pathways in the sympathetic nervous system. Trends in neurosciences, 15(12), 475-481.

[35] Jolivet, R., Lewis, T. J., & Gerstner, W. (2004). Generalized integrate-and-fire models of neuronal activity approximate spike trains of a detailed model to a high degree of accuracy. Journal of neurophysiology, 92(2), 959-976.

[36] Joyner, M. J., & Casey, D. P. (2015). Regulation of increased blood flow (hyperemia) to muscles during exercise: a hierarchy of competing physiological needs. Physiological reviews.

[37] Kember, G., Armour, J. A., & Zamir, M. (2011). Neural control of heart rate: the role of neuronal networking. Journal of theoretical biology, 277(1), 41-47.

[38] Kember, G., Armour, J. A., & Zamir, M. (2013). Dynamic neural networking as a basis for plasticity in the control of heart rate. Journal of theoretical biology, 317, 39-46.

[39] Kember, G., Armour, J. A., & Zamir, M. (2013). Neural control hierarchy of the heart has not evolved to deal with myocardial ischemia. Physiological genomics, 45(15), 638-644.

[40] Kember, G., Ardell, J. L., Armour, J. A., & Zamir, M. (2014). Vagal nerve stimulation therapy: what is being stimulated?. PLoS One, 9(12), e114498.

[41] Kember G, Ardell JL, Shivkumar K, Armour JA. (2017) Recurrent myocardial infarction: Mechanisms of free-floating adaptation and autonomic derangement in networked cardiac neural control. PLOS ONE 12(7): e0180194

[42] Kirchheim, H. R. (1976). Systemic arterial baroreceptor reflexes. Physiological reviews, 56(1), 100-177.

[43] Knight, B. W. (1972). The relationship between the firing rate of a single neuron and the level of activity in a population of neurons: Experimental evidence for resonant enhancement in the population response. The Journal of general physiology, 59(6), 767-778.

[44] Korner, P. I. (1971). Integrative neural cardiovascular control. Physiological Reviews, 51(2), 312-367.

[45] Kwag, J., Jang, H. J., Kim, M., & Lee, S. (2014). M-type potassium conductance controls the emergence of neural phase codes: a combined experimental and neuron modelling study. Journal of The Royal Society Interface, 11(99), 20140604.

[46] Lewis, T. J., & Rinzel, J. (2003). Dynamics of spiking neurons connected by both inhibitory and electrical coupling. Journal of computational neuroscience, 14, 283-309.

[47] Lindner, B. (2013, December). Low-pass filtering of information in the leaky integrate-and-fire neuron driven by white noise. In International Conference on Theory and Application in Nonlinear Dynamics (ICAND 2012) (pp. 249-258). Cham: Springer International Publishing.

[48] Ma, J., & Tang, J. (2017). A review for dynamics in neuron and neuronal network. Nonlinear Dynamics, 89, 1569-1578.

[49] Mahdi, A., Sturdy, J., Ottesen, J. T., & Olufsen, M. S. (2013). Modeling the afferent dynamics of the baroreflex control system. PLoS computational biology, 9(12), e1003384.

[50] Mahowald, M., & Douglas, R. (1991). A silicon neuron. Nature, 354(6354), 515-518.

[51] Marrion, N. V. (1997). Control of M-current. Annual review of physiology, 59(1), 483-504.

[52] Mattia, M., & Del Giudice, P. (2002). Population dynamics of interacting spiking neurons. Physical Review E, 66(5), 051917.

[53] Mejias, J. F., Payeur, A., Selin, E., Maler, L., & Longtin, A. (2014). Subtractive, divisive and non-monotonic gain control in feedforward nets linearized by noise and delays. Frontiers in computational neuroscience, 8, 19.

[54] Michaelevski, I., & Lotan, I. (2011). Role of neuronal potassium M-channels in sympathetic regulation of cardiac function. The Journal of Physiology, 589(Pt 11), 2659.

[55] Mokrane, A., & Nadeau, R. (1998). Dynamics of heart rate response to sympathetic nerve stimulation. American Journal of Physiology-Heart and Circulatory Physiology, 275(3), H995-H1001.

[56] Nowak, L. G., Sanchez-Vives, M. V., & McCormick, D. A. (1997). Influence of low and high frequency inputs on spike timing in visual cortical neurons. Cerebral Cortex (New York, NY: 1991), 7(6), 487-501.

[57] Nykamp, D. Q., & Tranchina, D. (2000). A population density approach that facilitates large-scale modeling of neural networks: Analysis and an application to orientation tuning. Journal of computational neuroscience, 8, 19-50.

[58] Nykamp, D. Q., & Tranchina, D. (2001). A population density approach that facilitates large-scale modeling of neural networks: extension to slow inhibitory synapses. Neural computation, 13(3), 511-546.

[59] Osterrieder, W., Noma, A., & Trautwein, W. (1980). On the kinetics of the potassium channel activated by acetylcholine in the SA node of the rabbit heart. Pflugers Archiv: European Journal of Physiology, 386(2), 101-109.

[60] Park, J. H., Gorky, J., Ogunnaike, B., Vadigepalli, R., & Schwaber, J. S. (2020). Investigating the effects of brainstem neuronal adaptation on cardiovascular homeostasis. Frontiers in neuroscience, 14, 470.

[61] Pewsey, A., & Garca-Portugus, E. (2021). Recent advances in directional statistics. Test, 30(1), 1-58.

[62] Rajendra Acharya, U., Paul Joseph, K., Kannathal, N., Lim, C. M., & Suri, J. S. (2006). Heart rate variability: a review. Medical and biological engineering and computing, 44, 1031-1051.

[63] Rajendran, P. S., Nakamura, K., Ajijola, O. A., Vaseghi, M., Armour, J. A., Ardell, J. L., & Shivkumar, K. (2016). Myocardial infarction induces structural and functional remodelling of the intrinsic cardiac nervous system. The Journal of physiology, 594(2), 321-341.

[64] Rowell, L. B. (1974). Human cardiovascular adjustments to exercise and thermal stress. Physiological reviews, 54(1), 75-159.

[65] Saum WR, Brown AM, Tuley FH (1976) An electrogenic sodium pump and baroreceptor function in normotensive and spontaneously hypertensive rats. Circ Res 39: 497505.

[66] Schaffer, E. S., Ostojic, S., & Abbott, L. F. (2013). A complex-valued firing-rate model that approximates the dynamics of spiking networks. PLoS computational biology, 9(10), e1003301.

[67] Selyanko, A. A., Derkach, V. A., & Skok, V. I. (1982). Voltage-dependent actions of short-chain polymethylene bis-trimethylammonium compounds on sympathetic ganglion neurons. Journal of the Autonomic Nervous System, 6(1), 13-21.

[68] Shelley, M. J., & Tao, L. (2001). Efficient and accurate time-stepping schemes for integrate-and-fire neuronal networks. Journal of Computational Neuroscience, 11, 111-119.

[69] Shivkumar, K., Ajijola, O. A., Anand, I., Armour, J. A., Chen, P. S., Esler, M., ... & Zipes, D. P. (2016). Clinical neurocardiology defining the value of neurosciencebased cardiovascular therapeutics. The Journal of physiology, 594(14), 3911-3954.

[70] Skok, V. I., Farrugia, G., Ermilov, L. G., Miller, S. M., & Szurszewski, J. H. (1998). Patch-clamp recordings of membrane currents evoked during natural synaptic activity in sympathetic neurons. Neuroscience, 87(2), 509-517.

[71] Skok, V. I., & Ivanov, A. Y. (1983). What is the ongoing activity of sympathetic neurons?. Journal of the autonomic nervous system, 7(3-4), 263-270.

[72] Springer, M. G., Kullmann, P. H., & Horn, J. P. (2015). Virtual leak channels modulate firing dynamics and synaptic integration in rat sympathetic neurons: implications for ganglionic transmission in vivo. The Journal of physiology, 593(4), 803-823.

[73] Stevens, C., & Zador, A. (1995). When is an integrate-and-fire neuron like a poisson neuron?. Advances in neural information processing systems, 8.

[74] Strogatz, S. H. (2018). Nonlinear dynamics and chaos with student solutions manual: With applications to physics, biology, chemistry, and engineering. CRC press.

[75] Teasell, R. W., Arnold, J. M. O., Krassioukov, A., & Delaney, G. A. (2000). Cardiovascular consequences of loss of supraspinal control of the sympathetic nervous system after spinal cord injury. Archives of physical medicine and rehabilitation, 81(4), 506-516.

[76] Thompson GW, Collier K, Ardell JL, Kember G, Armour JA.. (2000) Functional interdepen- dence of neurons in a single canine intrinsic cardiac ganglionated plexus. J Physiol. 528.3: 561-571

[77] Ursino, M. (1998). Interaction between carotid baroregulation and the pulsating heart: a mathematical model. American Journal of Physiology-Heart and Circulatory Physiology, 275(5), H1733-H1747.

[78] Vadigepalli, R., Doyle, F. J., & Schwaber, J. S. (2001). Analysis and neuronal modeling of the nonlinear characteristics of a local cardiac reflex in the rat. Neural computation, 13(10), 2239-2271.

[79] Vaseghi M & Shivkumar K (2008) The Role of the Autonomic Nervous System in Sudden Cardiac Death. Progress in Cardiovascular Diseases 50(6): 404-19.

[80] Verkerk, A. O., Remme, C. A., Schumacher, C. A., Scicluna, B. P., Wolswinkel, R., de Jonge, B., ... & Veldkamp, M. W. (2012). Functional Nav1. 8 channels in intracardiac neurons: the link between SCN10A and cardiac electrophysiology. Circulation research, 111(3), 333-343.

133

[81] Wheeler, D. W., Kullmann, P. H., & Horn, J. P. (2004). Estimating use-dependent synaptic gain in autonomic ganglia by computational simulation and dynamic-clamp analysis. Journal of neurophysiology, 92(5), 2659-2671.

[82] Wolff, J. R., Kasa, P., Dobo, E., Romgens, H. J., Parducz, A., Joo, F., & Wolff, A. (1993). Distribution of GABAimmunoreactive nerve fibers and cells in the cervical and thoracic paravertebral sympathetic trunk of adult rat: evidence for an ascending feedforward inhibition system. Journal of Comparative Neurology, 334(2), 281-293.

[83] Yang, P. C., Rose, A., DeMarco, K. R., Dawson, J. R., Han, Y., Jeng, M. T., ... & Clancy, C. E. (2023). A multiscale predictive digital twin for neurocardiac modulation. The Journal of physiology, 601(17), 3789-3812.

[84] Zaika, O., Zhang, J., & Shapiro, M. S. (2011). Functional role of Mtype (KCNQ) K+ channels in adrenergic control of cardiomyocyte contraction rate by sympathetic neurons. The Journal of physiology, 589(10), 2559-2568.

[85] Zhao, S., Liu, J., Tan, Y., & Qian, K. (2022). Application of Transient Slope of Zero and Pole in Bode Diagram in Automatic Identification of Filter Parameters. Journal of Control, Automation and Electrical Systems, 33(6), 1840-1850.